Thermal Fly-height Control Slider Dynamics and Slider-Lubricant Interactions in Hard Disk Drives

by

Sripathi Vangipuram Canchi

A dissertation submitted in partial satisfaction of the

requirements for the degree of

Doctor of Philosophy

in

Engineering – Mechanical Engineering

in the

Graduate Division

of the

University of California, Berkeley

Committee in charge:

Professor David B. Bogy, Chair
Professor Roberto Horowitz
Professor Jon Wilkening

Spring 2011

The dissertation of Sripathi Vangipuram Canchi, titled Thermal Fly-height Control Slider Dynamics and Slider-Lubricant Interactions in Hard Disk Drives, is approved:

Chair _____ Date May 2, 2011

_____ Date 5/2/11

_____ Date 5/3/11

University of California, Berkeley

Thermal Fly-height Control Slider Dynamics and Slider-Lubricant Interactions in Hard Disk Drives

by

Sripathi Vangipuram Canchi

Abstract

Thermal Fly-height Control Slider Dynamics and Slider-Lubricant Interactions in Hard Disk Drives

by

Sripathi Vangipuram Canchi

Doctor of Philosophy in Engineering – Mechanical Engineering

University of California, Berkeley

Professor David B. Bogy, Chair

The storage industry's density target of $10Tb/in^2$ in hard disk drives within the next decade requires a significant change in head-disk interface (HDI) architecture, and it likely involves a combination of new technologies such as Heat Assisted Magnetic Recording and Bit Patterned Media Recording to mention a few. Independent of the actual recording technology, it is necessary to reduce the magnetic spacing to within $2nm$, which implies a physical spacing as little as $0.25nm$ at the read-write transducer location. At such a small spacing intermittent contact between the slider and the lubricant layer or hard overcoat surface on the disk becomes inevitable. A continuous lubricant-contact HDI may in fact be necessary to meet future magnetic spacing needs. While the new recording technologies impose a significantly tighter budget on the slider dynamics in all three directions (vertical, down-track and off-track), the contacting HDI must be reliable, ensuring no degradation of lubricant or disk overcoats even after prolonged operation.

The current slider technology uses Thermal Fly-height Control (TFC) to bring the read-write portion of the slider closer to the disk by resistive heating induced thermal deformation/protrusion. While subnanometer level clearance can be achieved using the TFC, slider stability and HDI reliability at very small spacing remains to be understood. In order to further reduce the magnetic spacing using the TFC architecture, a recording strategy with a small portion of the thermal protrusion in intermittent or continuous contact with the lubricant layer of the disk has been proposed, but there is limited theoretical and experimental work to verify the feasibility of this technique. The focus of this work is to advance the understanding of TFC slider dynamics and slider-lubricant interactions at a HDI with contact through experiments and modeling.

Slider-lubricant contact is experimentally established by carefully controlling the TFC heater power, and the three dimensional slider dynamics under lubricant-contact is investigated. The degree of slider-lubricant contact is shown to influence the slider's vibration modes. A simple two degree of freedom model that accounts for nonlinearities at the HDI through quadratic and cubic approximations is used to analytically investigate the interesting features of this problem. It is shown that the thermal protrusion induced by the heater power can cause the system modes to couple unfavorably for certain heater power ranges, and this

condition can manifest itself as large amplitude slider vibrations. Experiments are conducted to understand the interplay between slider dynamics and disk lubricant evolution under the thermal protrusion for contact and near contact conditions. Slider dynamics and lubricant rippling are shown to be well correlated and a mechanism of lubricant transfer from the slider to the disk at the onset of contact is demonstrated. Parametric investigations are conducted to understand the effect of lubricant type and thickness on lubricant distribution, lubricant depletion and subsequent lubricant recovery behavior at a contacting HDI.

To my family

Contents

List of Figures

List of Tables

Abbreviations

ABS	air bearing surface
AE	acoustic emission
BPMR	bit pattern media recording
HAMR	heat assisted magnetic recording
HDD	hard disk drive
HDI	head-disk interface
HGA	head gimbal assembly
JFT	joint frequency time
LDV	laser doppler vibrometer
MEMS	micro electro mechanical systems
OSA	optical surface analyzer
PFPE	perfluoropolyether
RPM	rotations per minute
TDMR	two dimensional magnetic recording
TDP	touchdown power
TEC	trailing edge center
TFC	thermal fly-height control
TOP	takeoff power
VCM	voice coil motor

Acknowledgments

I would like to thank Prof. David Bogy for his support and encouragement throughout my doctoral studies at UC Berkeley. He has been a great advisor, an inexhaustible source of motivation, and I am extremely grateful to him for providing me with the opportunities required for my professional and personal development.

I would also like to thank Prof. Roberto Horowitz and Prof. Jon Wilkening for their valuable inputs and feedback on my dissertation. My education at UC Berkeley was made complete by the enriching coursework that the university had to offer. I am indebted to all my instructors for their time, efforts and commitment to imparting and disseminating knowledge.

I had the unique opportunity to discuss my research with members from the industry. I am grateful for their comments in keeping my work current, suggesting directions for new research and providing good research parts for my experiments. I would like to specially thank Dr. Bruno Marchon and Dr. Run-Han Wang from Hitachi GST for their interest in my research and for their support during my internship.

My colleagues at CML have had an immeasurable positive impact on my work. I would like to thank them for the many stimulating discussions and their constructive feedback on my research. A special thanks to Kourosh Bakhtvar for his help with experiments and to Dolf Mardan for helping me with the computer networking needs required for my work.

The most important people behind my personal and professional successes are my parents and my sister. Their unconditional love and support have made me the person I am today. Their belief in my ability has always been an unending source of energy and confidence in my life. Needless to say, they were of tremendous help as I navigated through the rigors of my graduate studies.

Berkeley always felt like home because I had my extended family: Kedar Shah, Rupam Singla, Sameer Kelkar and Sara Beaini are not just my friends, but a great source of inspiration in my life. I have learned a great deal from each of them, and they have played an important role in keeping my 'workaholic' tendencies at check. I could always count on Sonja Schratter for golden words of wisdom and for the much appreciated tenderly love and care that accompanied it. I could not have asked for better company and I will always cherish the fun times we had together.

As a final note, I would like to acknowledge that this work was supported by the Computer Mechanics Laboratory and the Information Storage Industry Consortium's Extremely High Density Recording Program.

Chapter 1

Introduction

1.1 The Hard Disk Drive

The hard disk drive (HDD) is a non-volatile storage device used extensively in modern computers, which stores digital data on a spinning disk. The data is stored as concentric tracks of magnetic information on a ferromagnetic layer of the disk, and this information is written to and read back using a read-write head. While the concept of magnetic read/write has remained unchanged since its introduction in 1950's, the technology has undergone tremendous changes in the 50 years since its introduction. Notably, the areal density (defined as the number of bits stored per square inch) has increased exponentially from 2000 $bits/in^2$ in the 1950's to nearly 1 $Terra\ bit/in^2$ (1 $Terra\ bit \approx 10^{12}\ bits$) in current drives. The high storage densities have made it possible to manufacture large storage capacity, pocket-size portable drives at very affordable prices compared to the expensive, immovable tower like structures 50 years ago. Today, pocket drives up to 1 $Terra\ byte$ (1 $byte = 8\ bits$) are available at a cost of less than 20 $cents$ per $Giga\ byte$ (1 $Giga\ byte \approx 10^9\ bytes$).

1.1.1 The modern hard disk drive

Fig 1.1 shows a picture of a modern HDD with the top cover removed. The drive consists of stacked disk platters mounted on a spindle motor, which spins the disks at a constant angular velocity (usually in the range of $5400 - 10000$ RPM depending on the product). Information is written or read from the magnetic layers on the disk platters by a read-write head fabricated using micro electro mechanical systems (MEMS) technology onto a slider block, one for each side of the disk platter. Each slider block is attached to a flexure and suspension to form the head gimbal assembly (HGA) unit (Fig 1.2), and all the HGAs are attached to one E-block arm, which is actuated by a voice coil motor (VCM). Thus, the read-write heads can be actuated by the VCM to address any radius on the rotating disk to read and write the magnetic information on the disk.

1.1.2 The head-disk interface

The main mechanical challenge to make the read and write process possible is the ability to position the read-write head at the right distance away from the magnetic layer of the disk

and on the correct disk track where the magnetic information is to be recorded or accessed. This interface between the read-write head and the disk is termed the head-disk interface (HDI). According to the Wallace Spacing Loss equation, the intensity of the signal read back from the disk decreases exponentially with the distance between the magnetic layer and the read-write head [Wallace 1951]. To increase the magnetic bit areal density, the size of the magnetic bits must be made smaller and they must be squeezed closer to each other. This requirement implies that the read-write head must be brought closer to the magnetic layer to perform the higher resolution read and write operations with good signal to noise ratio.

Current HDDs have a sophisticated HDI that operates in the non-contact regime for the most part. The read-write head is spaced at a few nanometers clearance from the disk using air bearing technology. The surface of the slider block which faces the disk, called the air bearing surface (ABS) is etched with special patterns (Fig 1.3) which enables the slider to 'float' or 'fly' over the rotating disk separated by a small air gap which constitutes the air bearing. The ABS is designed to ensure that the forces and moments from the suspension and flexure that press the slider onto the disk are rightly balanced by the air bearing lift forces pushing it away from the disk, so that at equilibrium, the slider 'floats' or 'flies' without contact and with the required nanometer spacing at the read-write head location.

Two terms require important clarification when it comes to spacing at the HDI: the magnetic spacing and the physical spacing (also called the physical clearance, or head-disk clearance, or clearance), and a detailed look at the HDI is helpful (Fig 1.4). The disk media, which is usually a glass or aluminum substrate, is coated with a magnetic layer ($\approx 30nm$ thick), followed by a diamond like carbon (DLC) overcoat layer ($\approx 2nm$ thick) and lubricant ($\approx 1nm$ thick). The read-write head on the slider is similarly covered with a DLC layer ($\approx 1nm$ thick). The DLC and lubricant layers are important to provide good corrosion resistance, wear resistance in the event of contact and good surface chemistry that make a favorable non-contacting tribological interface. All the different layers including the disk substrate have an inherent roughness. When the slider is flying over the disk, the distance between the read-write head and the mean top surface of magnetic layer is called the magnetic spacing, and the distance between the mean surface of the DLC layer on the slider and the mean top surface of the disk lubricant is called the physical spacing.

The magnetic spacing directly affects the magnetic recording performance as well as the density of magnetic data that can be written on the disk, and to increase the recording density the magnetic spacing must be reduced. This demand can be achieved by decreasing the thickness of the DLC overcoat and lubricant layers as well as decreasing the physical spacing. While decreasing the overcoat and lubricant thickness can adversely affect the wear and corrosion resistance of the HDI, decreasing the physical spacing increases the probability for contact events which can cause slider (and hence read-write head) vibrations proving detrimental to reliable read-write operations.

Traditionally, the physical spacing has been reduced through better ABS design, but the task becomes increasingly challenging when physical spacings below $5nm$ are required. The increased tendency for slider instability arising from nonlinear forces at the HDI, slider interactions with the disk lubricant and disturbances due to occasional contact necessitate a new architecture that can stably achieve an extremely low physical spacing at the read-write head.

1.1.3 The thermal fly-height control technology

The thermal fly-height control (TFC) architecture is a novel technique which uses a resistive heating element to deform a local region around the read-write head portion of the slider, bringing it closer to the disk [Meyer et al. 1999]. The head-disk spacing may be controlled by changing the power supplied to the TFC heater, thereby controlling the temperature and hence the slider's local deformation profile.

Fig 1.5 shows the ABS, a zoomed scan of the exaggerated thermal protrusion bulge at the read-write head location and the HDI schematic with thermal protrusion. The TFC architecture therefore offers the solution of having a high flying ABS design (flying at $\approx 10nm$) wherein the read-write head can be brought to within subnanometer clearance from the disk on demand. Since the deformation is confined to only a small region around the read-write head, the actual area of the slider that comes into proximity with the disk is very small, reducing the ill effects of the destabilizing forces.

The HDI design is therefore a formidable challenge encompassing the mechanical engineering fields of tribology, dynamics, mechanics, heat transfer, fluid dynamics and material sciences to mention a few, which need to be integrated with other technical fields like magnetic recording physics, signal processing, control systems, product design and manufacturing so as to realize a functioning hard disk drive.

1.2 Motivation

The magnetic storage areal density (measured in bits per square inch) in today's HDD stands just under the $1Tb/in^2$ ($1\ Terra\ bit/square\ inch$) mark. This areal density translates to having a physical spacing of $2nm$ at the read-write head location. Historically, an increase in the storage density has been achieved by reducing the physical spacing at the read-write head of traditional (non TFC) sliders by careful ABS design and by relying heavily on tight manufacturing/assembly tolerance controls to realize a successful product. While this method with traditional sliders worked well for lower storage density needs (of up to tens of Gb/in^2) it becomes extremely difficult when the physical spacing requirements fall below $5nm$.

Several challenges arise while designing an extremely low flying traditional slider. Destabilizing nonlinear effects become important when the spacing reduces below $5nm$. Intermolecular forces influence the sliders flying stability leading to fly-height modulations and occasional contact with the disk/lubricant [Thornton and Bogy 2003b, Wu and Bogy 2002]. Slider-disk contact causes frictional tribocharging and the resulting electrostatic potential can further destabilize the slider's fly-ability proving detrimental to HDI performance [Ambekar et al. 2005, Gupta and Bogy 2005].

The detrimental effects of slider-lubricant interactions on slider dynamics and on HDI performance are well documented. The coupled effect of slider dynamics and lubricant modulation on each other (washboarding effect) is a serious concern for HDI reliability [Dai et al. 2004a]. Even for a noncontacting interface, lubricant transfer from the disk to the slider occurs by evaporation/condensation mechanisms, and it is enhanced by flow and accumulation of the lubricant on the slider's trailing end [Marchon et al. 2003]. Lubricant drop-off from the slider's trailing end to the disk has been experimentally observed and

is known to cause magnetic spacing changes that impact reliable read-write performance [Moseley and Bogy 2009, Pit et al. 2003]. Contact between the slider and disk enhances slider-lubricant interactions promoting meniscus formation and lubricant transfer between the disk and the slider [Ambekar and Bogy 2005, 2006].

In addition to slider instability and slider lubricant interactions, the reliability of the HDI and recording performance is severely compromised because of contact induced slider/disk wear and the particulate matter generated by this process.

These challenges motivated previous researchers to extensively investigate the HDI of traditional sliders in contact through experiments and simulation [Kiely and Hsia 2006, Knigge and Talke 2001, Wang et al. 2001, Yu et al. 2007]. Slider designs for partial/continuous contact recording architectures have been proposed as part of strategies to achieve the $1Tb/in^2$ and higher storage density targets [Chen and Bogy 2007, Mate et al. 2004, Xu et al. 2005]. While a working partial/continuous contact HDI has never been implemented in products, the studies show that in order to minimize contact related disturbance to slider flying attitude, it is important to reduce the actual area of the slider-disk contact, thereby reducing friction and contact forces generated at the HDI. Reducing the actual area of the slider which is in proximity and contact with the disk has the added advantage of decreasing the magnitude of the destabilizing intermolecular and electrostatic forces in addition to minimizing the slider-lubricant interactions.

The TFC slider architecture proved very successful in overcoming the limitations of the traditional slider designs. This architecture allows for a high flying ABS design (flying at $\approx 10nm$) with only a small portion around the read-write head coming into proximity with the disk. While TFC sliders were first introduced to make it possible to correct for fly-height deviations in a finished product and help relax the tolerance budgets during ABS manufacturing and assembly processes, their advantages have been leveraged with further research to currently bring the read-write head to within $2nm$ physical spacing 'on demand' for specific read-write operations in the drive. Even as issues pertaining to the long term HDI reliability with TFC sliders operating at $2nm$ physical spacing need to be addressed, the goal of $1Tb/in^2$ appears within reach using the TFC slider architecture working in a non-contact regime.

The future goals set by the disk drive industry are ambitious: to reach an areal density of $4Tb/in^2$ by 2016 and subsequently reach the $10Tb/in^2$ goal by the end of the decade. A significant change in HDI architecture is expected, and it likely involves a combination of new technologies such as Heat Assisted Magnetic Recording (HAMR) or Bit Patterned Media Recording (BPMR) to increase the magnetic bit areal density and Two-dimensional Magnetic Recording (TDMR) to increase the track density. Independent of the actual recording technology, it is necessary to further reduce the magnetic spacing to within $2nm$, which implies a physical spacing of only about $0.25nm$ at the read-write head location. This sub-nanometer spacing is in fact comparable to the root mean square roughness of current disk media, and it is expected that even with further improvements in media roughness, intermittent contact between the slider and the lubricant layer or even the disk overcoat will become unavoidable. A continuous lubricant-contact HDI may in fact be necessary to meet future magnetic spacing needs. While the new recording technologies impose a significantly tighter budget on slider dynamics in all three directions (vertical, down-track and off-track), the contacting HDI must be reliable, ensuring no degradation of lubricant or disk overcoats

even after prolonged operation.

Several challenges arise when trying to design a HDI for subnanometer spacing that can accommodate intermittent or continuous contact. Accurate spacing calibration becomes very important. In current drives, the head-disk clearance is calibrated against the TFC heater power by first determining the touch-down power (TDP), i.e. the power to achieve zero-clearance or slider contact with the lubricant on the disk. The TDP together with the knowledge of the slider's thermal actuation efficiency (fly-height loss per milliwatt) is used to calculate and supply the appropriate heater power to achieve a desired head-disk clearance during operation. Accurate determination of TDP becomes even more critical as the spacing control budgets decrease. Slider dynamics at close spacing as well as slider-lubricant interactions affect the TDP in addition to the slider's continued performance over time. Apparent spacing increases due to lubricant accumulation on the slider's trailing end pose a challenge to the reliable measurement and calibration of the head-disk clearance in a working drive [Marchon et al. 2009, Mate et al. 2010]. Recent investigations on the feasibility of recording in a 'lubricant-surfing' regime [Liu et al. 2009] open new questions on slider-lubricant interactions in contact and the associated slider dynamics. A complete understanding of the various phenomena at the HDI of TFC sliders in contact is still lacking, and an advancement of this understanding is the focus of this dissertation.

1.3 Objective and Scope

The primary thrust of this dissertation is to advance the understanding of TFC slider dynamics and slider-lubricant interactions at the HDI by

- experimentally investigating the characteristic phenomena at the HDI of TFC sliders in intermittent and continuous contact with the lubricant and the disk
- developing an understanding of the phenomena through empirical observations and modeling, and
- translating this understanding into criteria that help in the process of designing a better HDI for future HDD needs.

1.4 Organization of the Dissertation

Chapter 1 gives an introduction to the HDD, the HDI and the state of the current technology including the TFC slider. Chapter 2 develops the motivation for the need for TFC sliders by first discussing the experimentally observed dynamics of traditional (non TFC) sliders in contact with the rotating disk. The results of these investigations clearly demonstrate the infeasibility of traditional sliders working in the contact regime and simultaneously achieving meaningful magnetic recording. Chapter 3 outlines the experimental methods developed to conduct successful tests using TFC sliders and the simulation work used to qualitatively validate these methods. The results from these preliminary experiments highlight the interesting areas concerning TFC slider dynamics and slider-lubricant interactions that require further investigation. Detailed investigations of the 3D (vertical, off-track and down-track)

dynamics of sliders carefully actuated into contact with the disk lubricant are presented in Chapter 4, and explanations for the peculiar slider dynamics observed for certain slider designs are presented in Chapter 5 using nonlinear systems theory. Further parametric investigations, including friction measurements at the HDI of TFC sliders in contact, are detailed in Chapter 6. Chapter 7 and Chapter 8 focus on experimental investigations that correlate slider dynamics to slider-lubricant interactions including disk lubricant distribution and lubricant transfer between the slider and the disk at the HDI of TFC sliders for contact and near contact conditions.

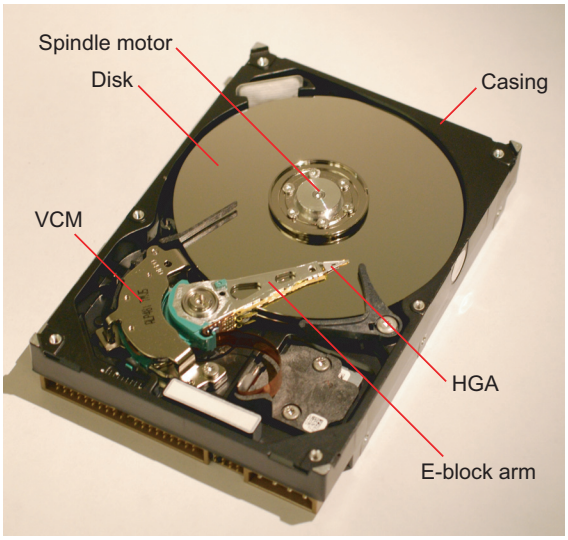

Figure 1.1: Parts in a modern HDD

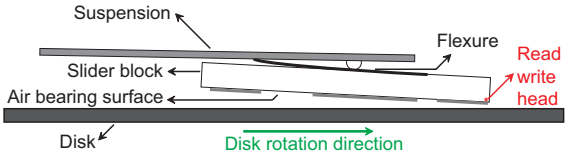

Figure 1.2: The HGA: suspension, flexure and slider block

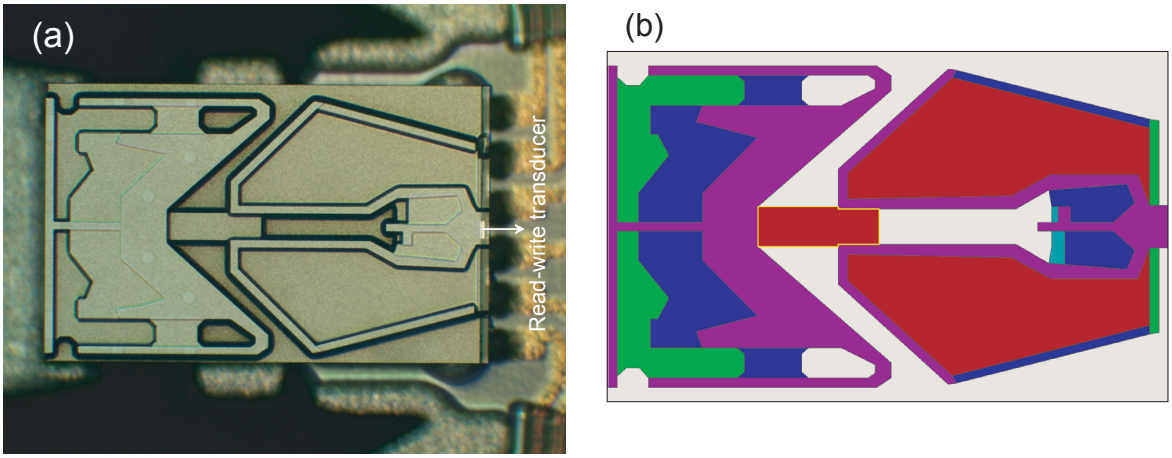

Figure 1.3: (a) Picture of an ABS showing the etch patterns (b) Reconstructed ABS model

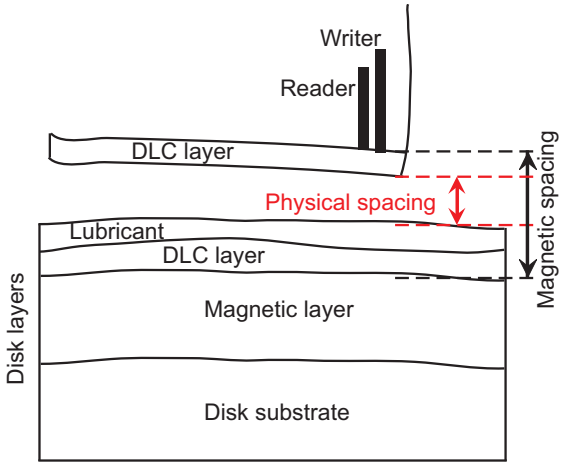

Figure 1.4: Detailed view of the HDI near the read-write head

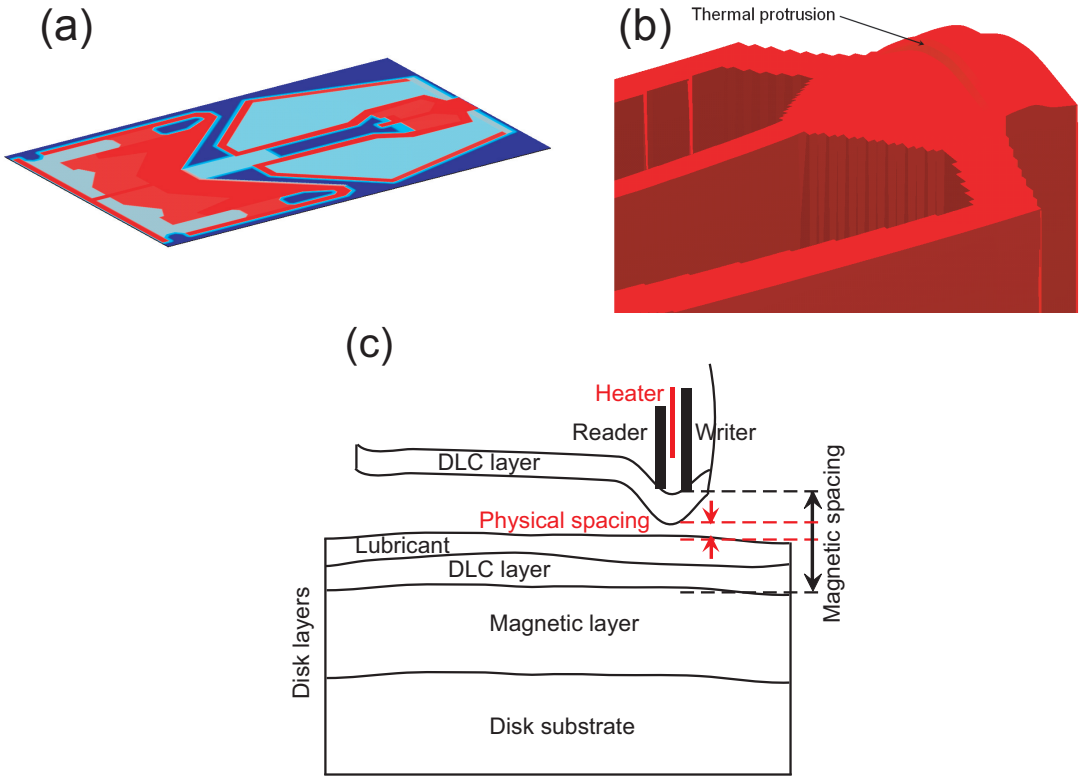

Figure 1.5: (a) TFC slider ABS (b) Zoomed section showing the trailing pad with thermal protrusion (c) Detailed view of the HDI near the read-write head with thermal protrusion

Chapter 2

The Dynamics of Traditional Sliders in Contact

This chapter discusses the experimental results on the dynamics of traditional sliders (i.e. sliders without thermal fly-height control) and the ensuing slider-lubricant interactions for a slider in contact with the disk. The combined vertical and off-track dynamics of extremely low flying traditional sliders are studied by bringing the slider into contact with the disk by a reduction in the disk rotation speed. It is shown that the vibrations induced by contact are beyond the limits required for meaningful recording performance. Detailed evaluations for the transient and longer term dynamics under contact are conducted for different slider and suspensions designs. These investigations are used to develop a consistent explanation for slider dynamics and the various competing phenomena at the contacting head-disk interface (HDI) such as slider/disk burnishing and slider-lubricant interactions. At close spacing and light contact, the dominant excitation occurs at suspension frequencies in the off-track direction and at the suspension and air bearing frequencies in the vertical direction. For a more severe contact condition, there is a stark change, and the excitation occurs over a broad range of frequencies. While suspension design significantly affects slider dynamics under contact, the effect of the contact area on slider dynamics is not evident from these experiments.

2.1 Experiments

In order to investigate the transient vertical and off-track dynamics of a traditional slider under contact, experiments are performed on a TTi spin stand that has programmable spindle speed capability. Polytec laser doppler vibrometers (LDV) are instrumented to measure the slider's vertical and off-track dynamics, and an Acoustic Emission (AE) sensor monitors contact between the slider and disk. Contact is induced by lowering the spindle speed, i.e the disk rotations per minute (RPM), and hence, decreasing the physical spacing between the slider and the disk (i.e slider's fly-height). Two different tests are devised to vary the spindle speed.

2.1.1 Spin-down spin-up (SDSU) test

In this test the spindle speed is lowered linearly with time from a specified maximum disk RPM, at which the slider flies without contact, to a specified minimum RPM, at which the slider contacts the disk, and increased linearly back to the specified maximum RPM (Fig 2.1a). The transient dynamics together with contact information are obtained from the LDV and the AE signal sampled at $1MHz$ during this test. The typical duration of a SDSU test is $16s$, with roughly half the time for spin-down and the rest for spin-up.

2.1.2 Dwell test

In this test the spindle RPM is lowered in steps of 300RPM from the specified maximum RPM to the minimum RPM (same as that for SDSU test) and raised back to the maximum RPM maintaining a controlled dwell time of $5s$ at each RPM (Fig 2.1b). The LDV and the AE signal are sampled at $1MHz$ for $1s$ at each dwell RPM for post processing.

The above two tests are useful in understanding the effects of the transient and the longer term slider-disk contact on the stability of the slider and the robustness of the HDI.

2.1.3 Post processing steps

The vertical and off-track velocity signals from the LDV are integrated to obtain the vertical and off-track displacements. In order to eliminate the low frequency noise that is characteristic of the LDV systems used, the velocity and displacement signals are high pass filtered at $10kHz$. For SDSU tests, the total test duration of $16s$ is divided into 160 intervals of $0.1s$, and the mean and the standard deviation (σ) of each interval is computed. In addition, the frequency content of each of these intervals is computed to obtain the joint frequency time plot (JFT) of the displacement, velocity and the AE signal. For the Dwell tests, the mean, the standard deviation (σ) and the frequency content of a $1s$ capture of AE and LDV signals is computed at each dwell RPM.

Experiments are performed on three different head gimbal assemblies (HGAs) differing in the slider and suspension form factors (Fig 2.2): HGA(I) 'pico' slider ($1.25mm \times 1.00mm$) on a long suspension, HGA(II) 'femto' slider ($0.85mm \times 0.70mm$) on a short suspension, and HGA(III) 'pico' slider on a short suspension. The media sample is a $95mm$ disk coated with 10.4Å Z-dol PFPE lubricant with a molecular weight of $3kDa$ and a low bonded ratio. All experiments are performed at 10^o skew.

2.2 Results and Discussion

Fig 2.3 and Fig 2.4 summarize the results of two SDSU tests performed on the same track, one immediately before, and one immediately after performing a Dwell test on that track. These plots show the change (3σ) of the AE signal, the vertical and the off-track displacements with disk linear velocity.

As the disk spins down, the AE signal shows a sharp jump in the 3σ value from the baseline indicating slider-media contact, and the linear velocity corresponding to contact initiation is called the touchdown velocity. Similarly, the takeoff velocity is defined as the

linear velocity at which slider-media contact ceases during disk spin-up. In general, there is a difference between the touchdown and the takeoff velocity values owing to competing phenomena at the HDI such as intermolecular forces and lubricant meniscus forces originating from slider-lubricant interaction and slider/media burnishing.

2.2.1 Effect of suspension design and slider form factor

SDSU1: (SDSU test before the Dwell test: Fig 2.3): The design of the suspension has a significant effect on the relative magnitudes of the vertical and off-track displacements when the slider contacts the media. Considering HGA(I) and HGA(III), which have the same pico slider on a long and short suspension respectively, it is evident from Fig 2.3b and Fig 2.3c that the slider's vertical (bouncing) displacements are dominant for the short suspension, while off-track displacements are dominant for the longer suspension. Considering HGA(II) and HGA(III) which have a femto and a pico slider, respectively, on the same short suspension, the vibrations of the smaller femto slider are expected to be smaller than that of the pico design because of the smaller area of the slider coming into contact with the disk [Chen and Bogy 2007, Mate et al. 2004]. (The center trailing pad width is $250\mu m$ for the pico slider and $80\mu m$ for the femto slider). However, Fig 2.3b and Fig 2.3c do not show any conclusive general trend: the vertical displacements are larger for HGA(II), while the off-track displacements are larger for HGA(III).

SDSU2: (SDSU test after the Dwell test: Fig 2.4): The results of the SDSU2 differ significantly from SDSU1. In the region where there is contact for both SDSU tests, the amplitude of the AE signal (indicative of the severity of contact) as well as that of the slider's displacements is higher for SDSU2 compared to SDSU1 at a given linear velocity. It is surmised that the prolonged interaction of the slider and lubricant at the lower RPM (with contact) during the Dwell test causes a deterioration of the HDI and hence the poor performance of the slider in the subsequent SDSU2 test. A comparison of the plots in Fig 2.4b and Fig 2.4c verifies our previous observation that vertical (bouncing) displacements are dominant for the short suspension, while off-track displacements are dominant for the longer suspension. The slider's form factor does not alter the slider's dynamics significantly because the amplitudes of vertical and off-track displacements are comparable for HGA(II) and HGA(III).

2.2.2 Comparison between SDSU test and Dwell test

The results for the amplitude of the AE signal, vertical displacements and off-track displacements from the Dwell test are compared to those of the SDSU tests in Fig 2.5 for HGA(I). The Dwell test results are shown with markers, while the curves are for the SDSU1 and SDSU2. Similar plots are included for HGA(II) and HGA(III) in Fig 2.6 and Fig 2.7, respectively.

From these figures it is observed that the results from the Dwell test agree better with the plots for SDSU2. During the Dwell test there is a prolonged interaction between the slider and the lubricant, especially at lower RPM when there is contact, and the HDI is altered significantly. For the SDSU2 the slider responds to this altered interface during contact, and hence the resulting plots for SDSU2 are in good agreement with the Dwell test results.

One conclusion that can be drawn from these figures is that the SDSU tests are better suited to predict the slider dynamics of a contacting HDI without significantly altering it. Additionally, if the results of SDSU1 and SDSU2 are in close agreement, it means that the Dwell test does not alter the HDI significantly, implying a robust contacting HDI. In the various experiments reported here, the results for SDSU2 differ from those for SDSU1, and hence the contacting HDI is inferred to be unreliable for long durations. It is important to note that the amplitude of slider vibrations under contact is far beyond the allowable limits for successful recording. For the given HGAs, the 3σ of the bouncing vibration should stay within $5nm$ for successful recording, and hence the HDI considered in these experiments are essentially unsuitable under contact.

2.2.3 Evidence of slider-lubricant interaction during contact

The changes that occur at the HDI during the Dwell test may be partially understood by looking at the change in touchdown and takeoff velocities of the SDSU1 and SDSU2 tests. This change is shown in Fig 2.8 for the three different HGAs considered. The touchdown velocity is greater than the takeoff velocity in SDSU1 for HGA(I), HGA(II) and HGA(III), and this trend is consistent with the burnishing of the disk asperities (and possibly the slider's contact pad) when it comes into contact with a new track on the disk. After a Dwell test is performed on the same track, the touchdown velocity in SDSU2 is less than the touchdown velocity in SDSU1 indicating a further burnishing of the track and/or slider during the Dwell test for all three HGAs.

In contrast to SDSU1, a significant change occurs after the Dwell test for HGA(II) and (III). The touchdown velocity in SDSU2 is noticeably less than the takeoff velocity for these HGAs, consistent with the hysteresis phenomena exhibited as a result of intermolecular and lubricant mediated adhesion at the HDI due to strong slider-lubricant interactions [Ambekar et al. 2005]. For HGA(I), however, the touchdown velocity remains higher than the takeoff velocity in SDSU2 indicating that the effect of slider-disk burnishing is far more dominant than the intermolecular and lubricant meniscus related adhesion forces at the HDI.

2.2.4 A consistent explanation for slider dynamics and slider lubricant interactions

Based on the above observations on slider-lubricant interactions, a consistent explanation for the relative magnitudes of the vertical and off-track motions for HGA(I), HGA(II) and HGA(III) emerges. The longer suspension in HGA(I) is inferred to be stiff in the vertical direction. As a result when the slider of HGA(I) comes in contact with the disk, the bouncing amplitudes are lower, but it is at the expense of a higher contact force at the HDI that causes higher disk track and/or slider burnishing and wear. In contrast, the short suspension of HGA(II) and HGA(III) is inferred to be less stiff in the vertical direction. When the slider comes into contact with the disk, the bouncing vibrations are higher, but there is lower disk/slider burnishing and wear. In this case, the forces from slider-lubricant interaction become dominant at the HDI, and the argument is supported by the clear hysteresis in touchdown and takeoff velocities for these HGA.

Observation of the sliders after testing under an optical microscope reveal a higher level of

lubricant pick-up on the sliders of HGA(II) and HGA(III) confirming higher slider-lubricant interactions for these cases as compared to HGA(I) (Fig 2.9).

2.2.5 Analysis in the frequency domain

The JFT plots for the off-track and vertical displacements capture the changes that occur in the slider's response when it comes in contact with the disk. Fig 2.10a and Fig 2.10b show the results for HGA(I), and the AE signal 3σ is plotted as a reference to mark contact initiation and termination.

As the fly-height of the slider decreases during disk spin-down, the slider first comes into light contact with the disk. The off-track motions are mainly excited at the suspension frequencies (with dominant excitation at $30kHz$). With a further reduction in the disk RPM, contact becomes more severe and the off-track vibrations are suddenly excited over a broad frequency range (seen as a dark band on the JFT plots). The vertical motion spectrum shows a similar behavior: at close spacing and light contact, the excitation is mainly at the suspension and air bearing frequencies, while for more severe contact, the excitation is over a wide frequency range. A nonlinear shift in the second harmonic of the air bearing frequency ($250kHz$ when the slider is flying) towards a higher frequency ($350kHz$) shows the nonlinear increase in the stiffness of the air-bearing with decreasing fly-height.

The FFT plots for Dwell tests on this slider (Fig 2.10c and Fig 2.10d) are shown for the disk RPM corresponding to near contact, light contact and severe contact conditions. The general trends of these plots compare well with the JFT plots of the SDSU test.

2.2.6 Effect of gram load change

The effect of an increase in the gram load on the slider's dynamics is studied by reducing the z-height of the slider from the design value by $3milli\ inches$. The results for HGAs(I) and (II) (Fig 2.11) show that the touchdown and takeoff velocities increase with increasing gram load, and it is consistent with a reduction in the fly-height of the slider. Whereas HGA(I) continues to exhibit 'inverse hysteresis' (touchdown velocity > takeoff velocity) supporting slider-disk track burnishing as the main phenomena at the HDI, HGA(II) exhibits hysteresis (touchdown velocity < takeoff velocity) supporting enhanced slider lubricant interaction. At a given linear velocity, the AE signal is higher for a higher gram load case, and the corresponding displacements in the off-track and vertical directions are also higher (Fig 2.12). An increase in gram load does not change the dominant behavior at the HDI (slider-track burnishing/wear vs. slider-lubricant interaction), but simply tends to enhance (worsen) the underlying phenomena.

2.3 Conclusion

This chapter presents the experimental results for the combined vertical and off-track dynamics and the ensuing slider-lubricant interactions when traditional (non TFC) sliders are brought into contact with the disk media. An evaluation of the transient and the longer term slider dynamics is performed using a sequence of spin-down spin-up test, followed by a dwell test and another spin-down spin-up test. While slider motions are excited beyond

reasonable limits required for successful magnetic recording, some relations on the competing phenomena at the contacting HDI such as slider-disk burnishing and slider-lubricant interactions, and their relation to the slider's dynamics is established. It may be inferred from these experiments that higher suspension vertical stiffness suppresses vertical bouncing motions at the expense of higher contact force and wear at the HDI, while lower suspension stiffness results in higher bouncing and increased slider-lubricant interactions, consistent with previous simulation studies [Chen and Bogy 2007]. Off-track motions of the slider are larger for longer suspension designs, which tend to have lower stiffness in the off-track direction. At close spacing and light contact, the dominant excitation occurs at suspension frequencies in the off-track direction and at the suspension and air bearing frequencies in the vertical direction. For a more severe contact condition, there is a stark change and excitation occurs over a broad range of frequencies. Previous simulation studies indicate that smaller contact pad widths should result in lower contact force and friction thereby reducing slider vibrations [Chen and Bogy 2007]. However, such a reduction is not evident from a comparison of results for 'pico' and 'femto' sliders (with larger and smaller trailing pad widths, respectively) mounted on the same suspension, possibly because slider-lubricant interactions are far more dominant at the HDI of these HGAs. A comparison of slider dynamics between traditional slider designs and TFC slider designs should better clarify the effect of contact area on slider dynamics and HDI performance.

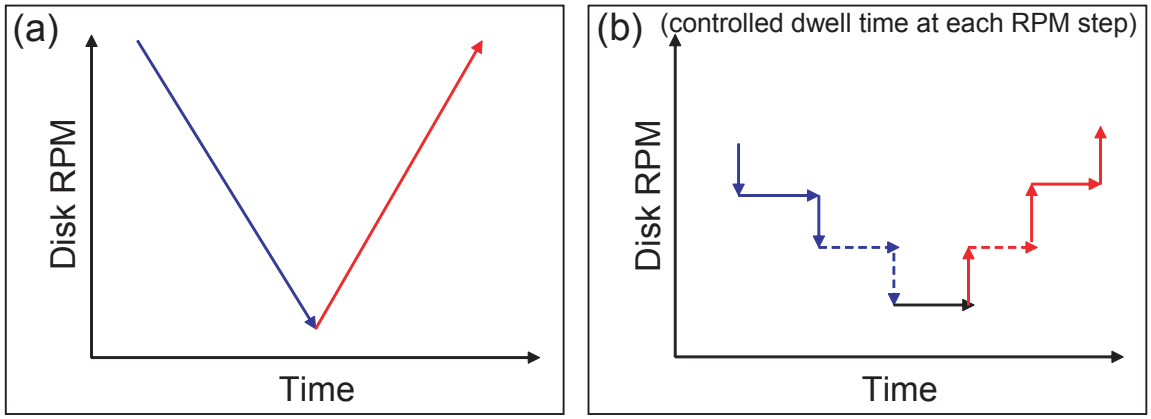

Figure 2.1: (a) Spin-down spin-up test (b) Dwell test

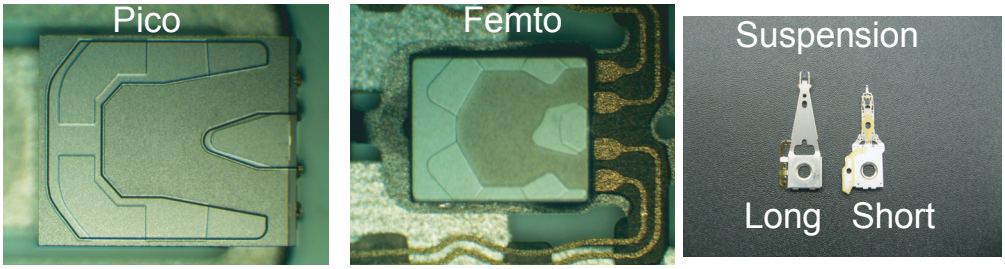

Figure 2.2: Slider air bearing surface and suspension pictures

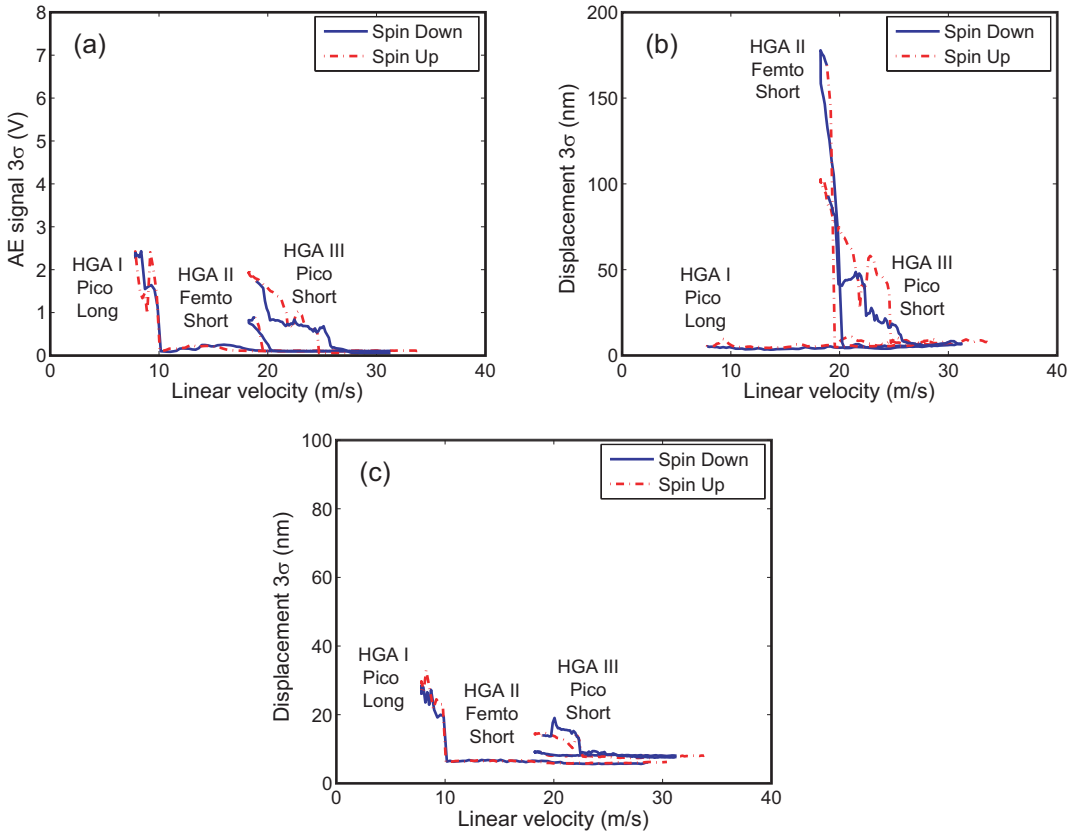

Figure 2.3: SDSU test before Dwell test (a) AE signal (b) Vertical displacement (c) Off-track displacement

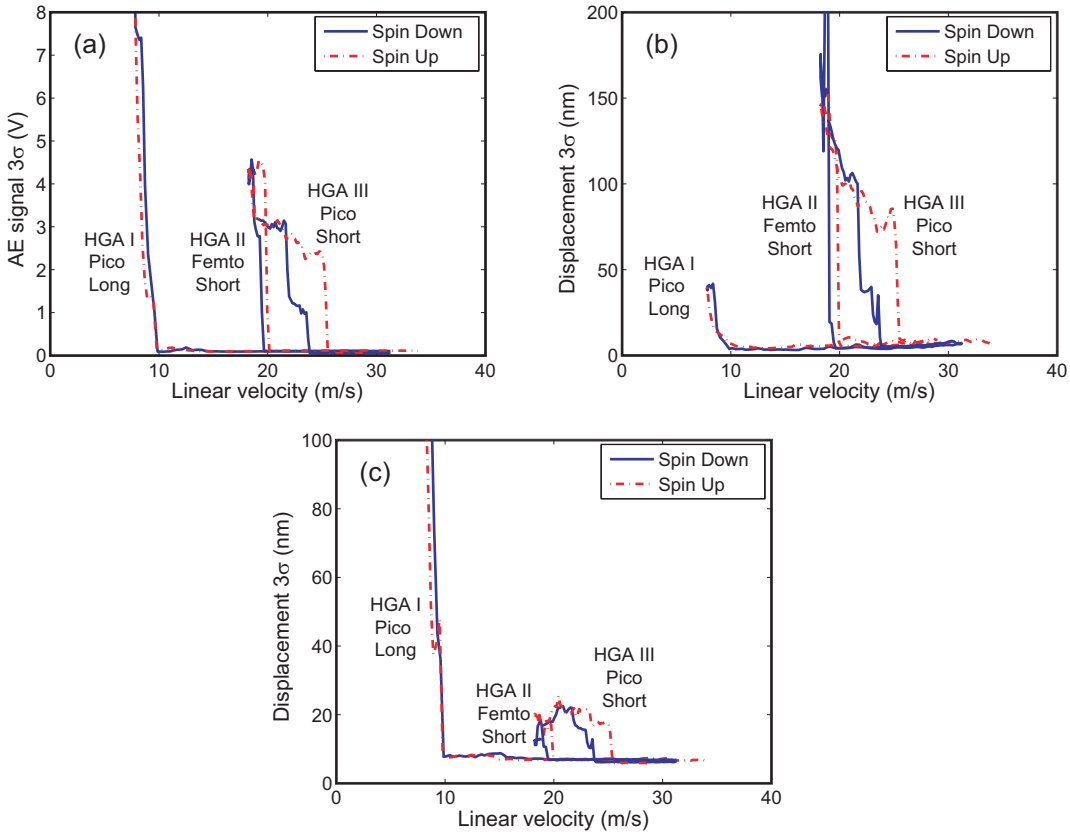

Figure 2.4: SDSU test after Dwell test (a) AE signal (b) Vertical displacement (c) Off-track displacement

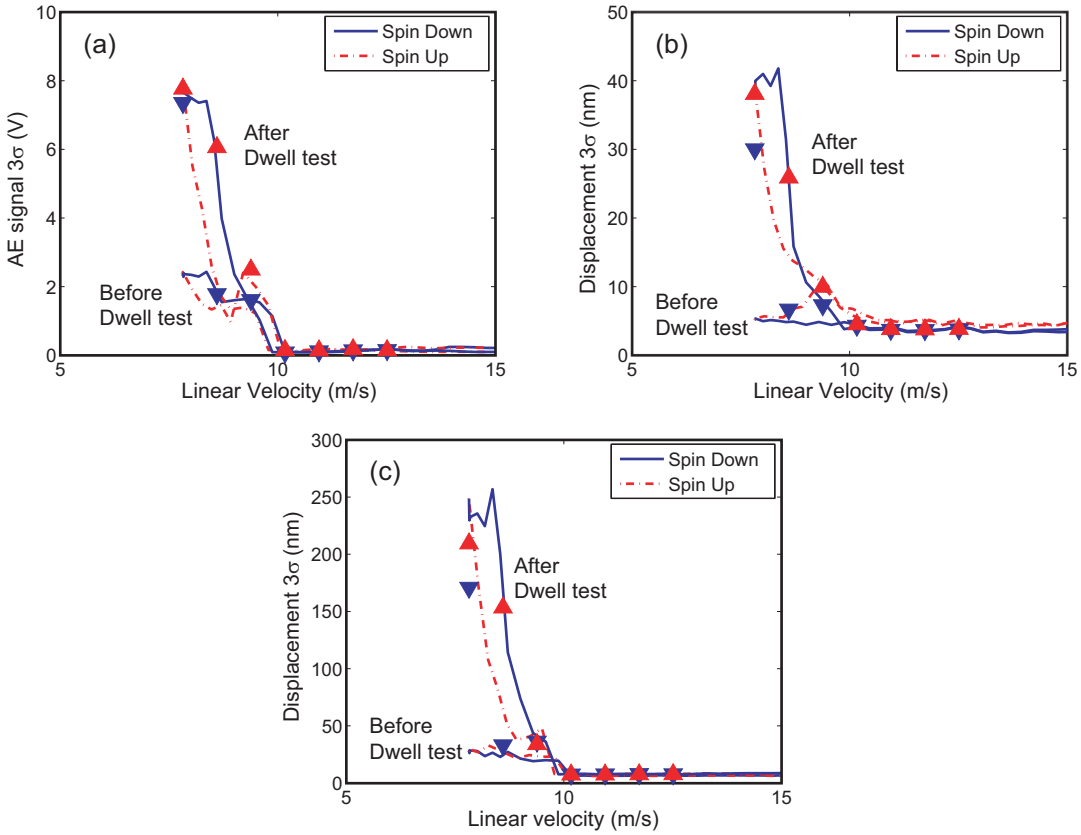

Figure 2.5: Comparison between SDSU test and Dwell test for HGA(I) (a) AE signal (b) Vertical displacement (c) Off-track displacement; ▼: Dwell test spin-down RPM, ▲: Dwell test spin-up RPM.

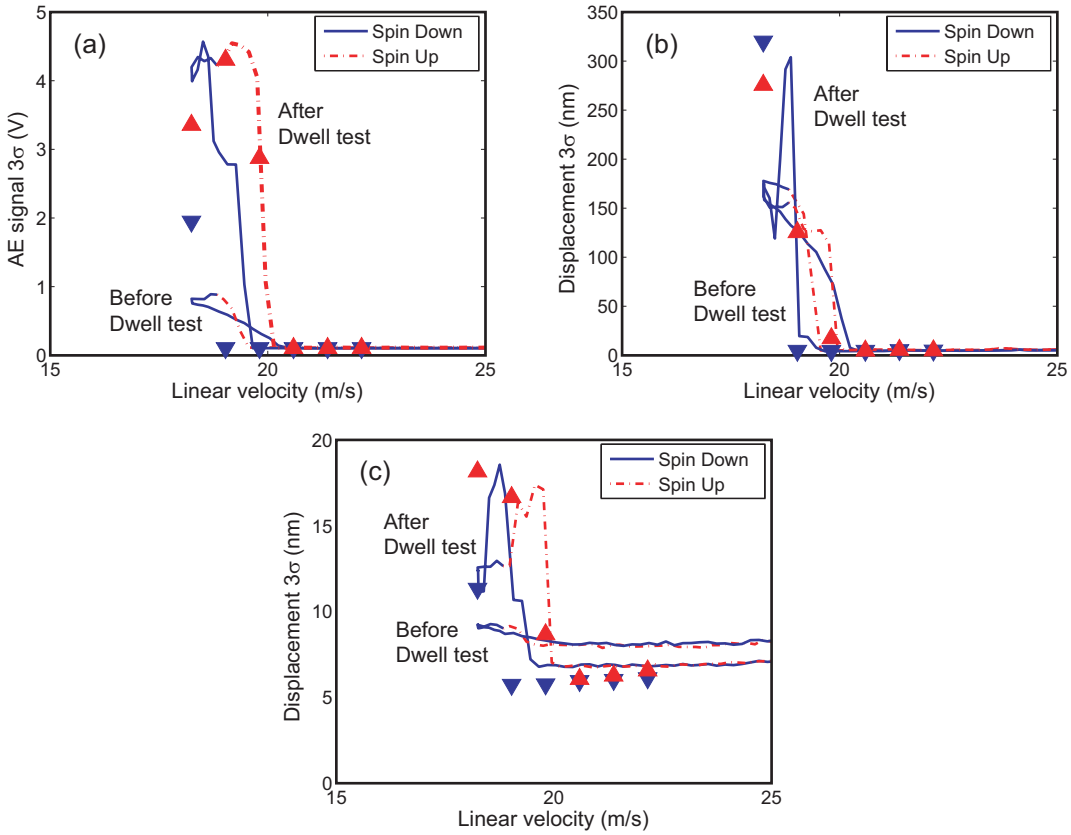

Figure 2.6: Comparison between SDSU test and Dwell test for HGA(II) (a) AE signal (b) Vertical displacement (c) Off-track displacement; ▼: Dwell test step-down, ▲: Dwell test step-up

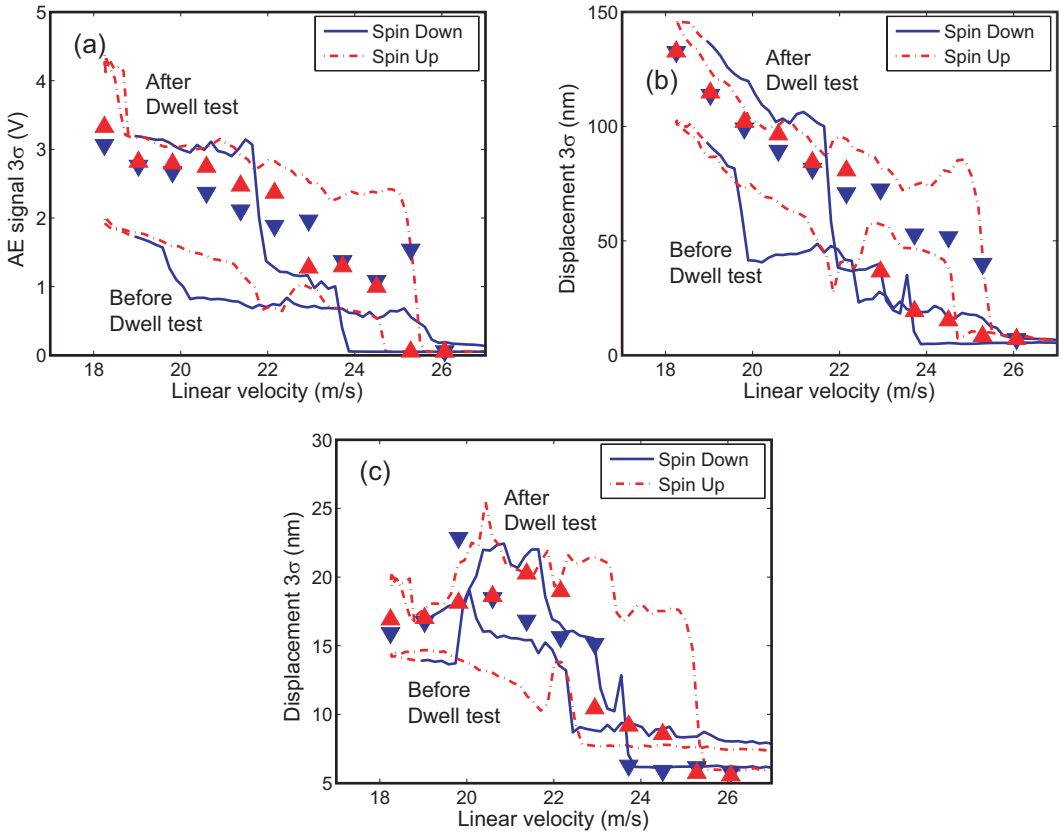

Figure 2.7: Comparison between SDSU test and Dwell test for HGA(III) (a) AE signal (b) Vertical displacement (c) Off-track displacement; ▼: Dwell test spin-down, ▲: Dwell test spin-up

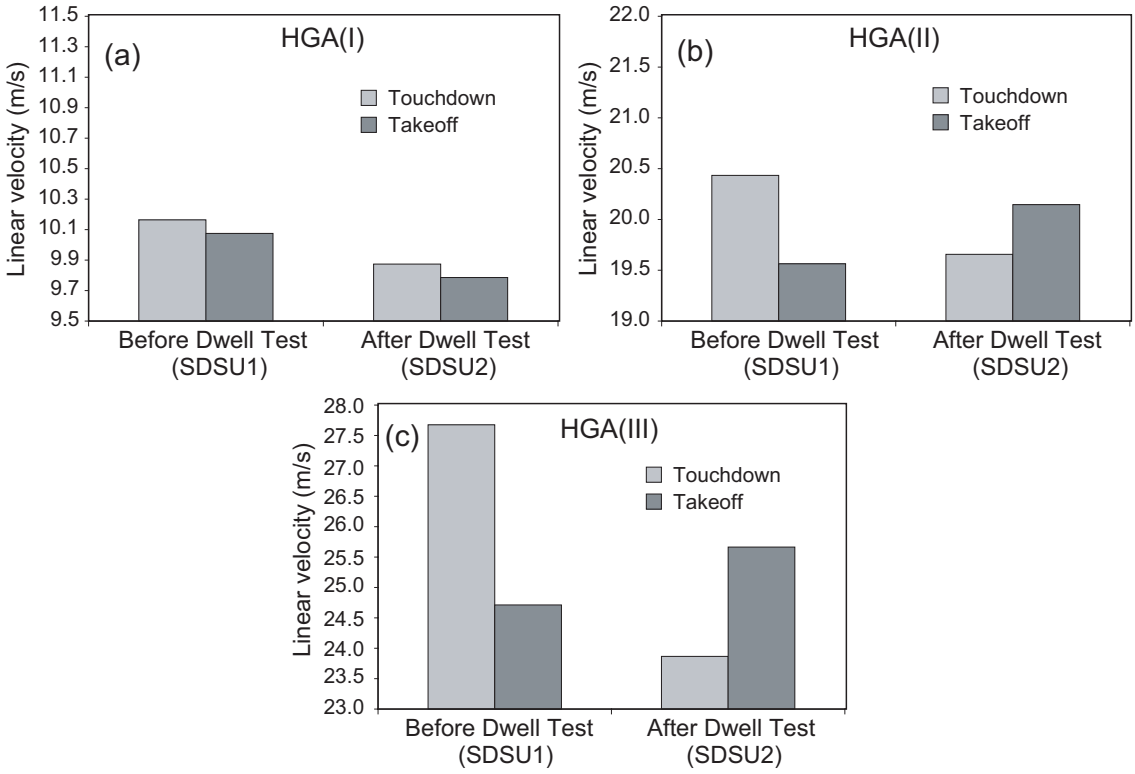

Figure 2.8: Effect of Dwell test on touchdown and takeoff velocity (a) HGA(I) (b) HGA(II) (c) HGA(III)

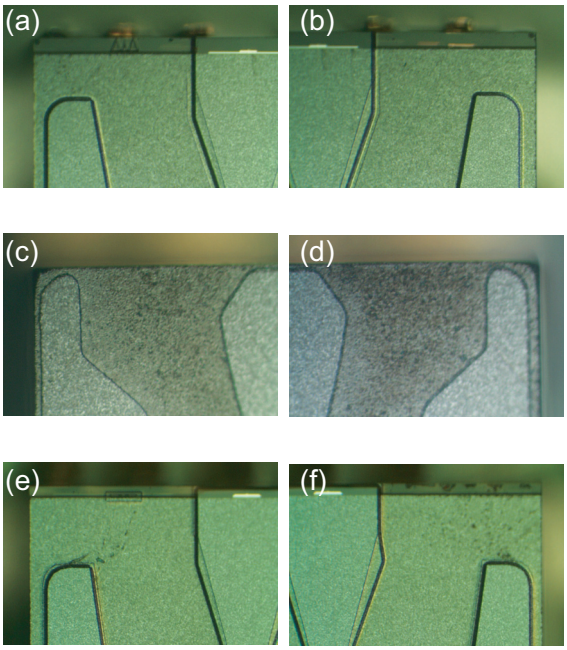

Figure 2.9: Slider contamination/lube pick-up (a,b) HGA(I); (c,d) HGA(II); (e,f) HGA(III)

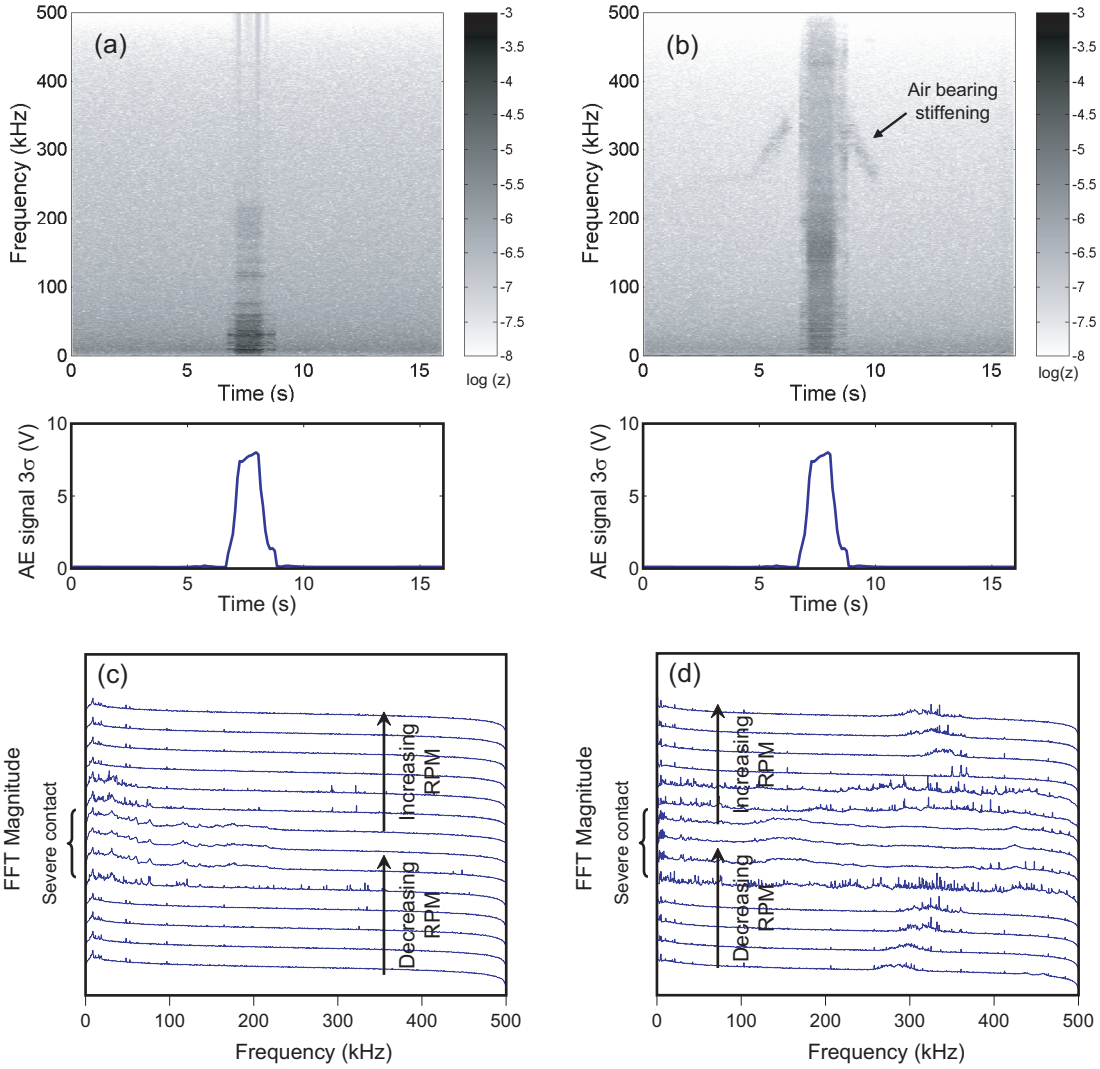

Figure 2.10: JFT plots of SDSU test for HGA(I) (a) Off-track motion (b) Vertical motion; FFT plots for Dwell tests (c) Off-track motion (d) Vertical motion

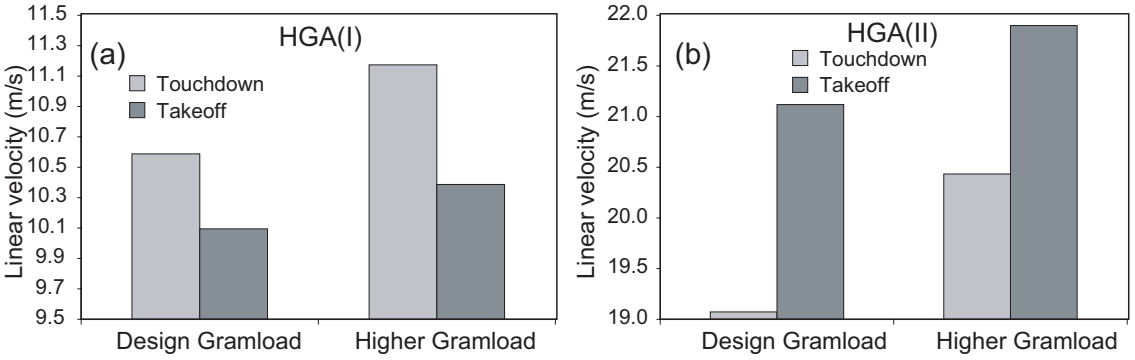

Figure 2.11: Effect of gram load (z-height reduction) on touchdown and takeoff velocity (a) HGA(I) (b) HGA(II)

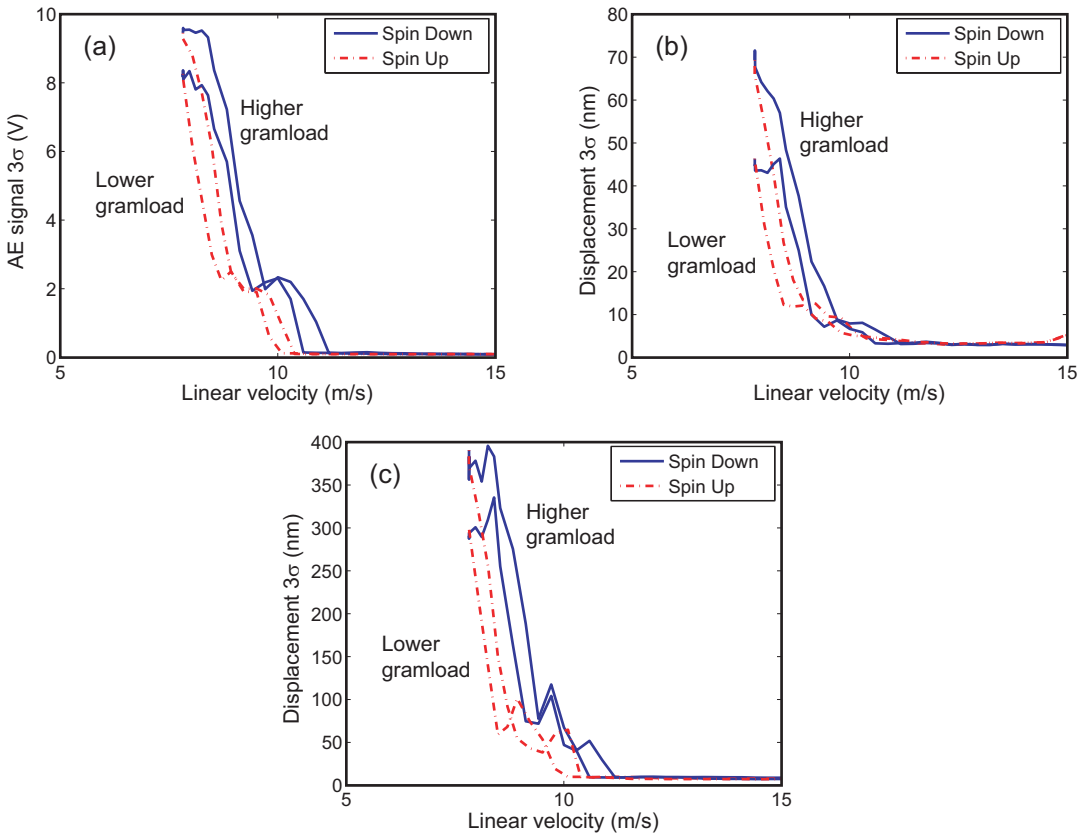

Figure 2.12: Effect of gram load (z-height reduction) for HGA(I) (a) AE signal (b) Vertical displacement (c) Off-track displacement

Chapter 3

Preliminary Experiments with Thermal Fly-height Control Sliders

A study of the dynamics of traditional sliders under contact (Chapter 2) reveals that such a head-disk interface (HDI) is unsuitable for good magnetic performance. This chapter reports the initial experimental investigations conducted on thermal fly-height control (TFC) sliders with focus on the topics of slider dynamics and disk lubricant distribution at a contacting HDI. The method used to power the slider's TFC heater and the new experimental techniques devised for TFC slider testing are described. A comparison of results show that thermal protrusion induced contact causes much lower slider vibration than contact induced by lowering the disk RPM (Chapter 2). TFC slider dynamics and its stability for low clearances (proximity) and contact are investigated using transient and longer duration contact tests, and the effect of thermal protrusion induced contact on the thin lubricant layer coating the disk is also investigated. Slider dynamics as well as disk lubricant distribution under the thermal protrusion differ significantly depending on the slider design (air bearing surface (ABS) and heater design). The results of simulations conducted using CMLAir air bearing software for a slider ABS whose geometry is reconstructed from measurements are correlated with those from experiments. These preliminary investigations using TFC sliders highlight the key areas pertaining to slider dynamics and slider-lubricant interactions which require further investigations.

3.1 Experiments

Experiments are conducted on a spin-stand instrumented with an optical surface analyzer (OSA) to monitor the disk lubricant profile *in-situ*, laser doppler vibrometer (LDV) to measure slider vertical vibrations and an acoustic emission (AE) sensor to detect contact between the slider and the disk Fig 3.1. The tests are conducted using a commercial TFC slider flown on research disks that are coated with perfluoropolyether lubricant of differing lubricant types and thickness.

3.1.1 Powering the TFC heater

Power to the TFC heater is provided using a data acquisition board (DAQ) and 'voltage follower' circuit. The DAQ is controlled using a custom written Labview program. This method offers the flexibility to input custom voltage/power waveforms to the TFC heater to conduct a wide range of tests. The full electrical circuitry is shown in Fig 3.2. The power/voltage waveform to be applied across the TFC heater is selected in the Labview program and the necessary voltage to be maintained across the TFC heater is computed on the fly. This voltage signal is output to the TFC heater from the DAQ analog output channel through the 'voltage follower' circuit. The 'voltage follower' circuit acts as a buffer and ensures that sufficient current is drained into the TFC heater to maintain the necessary voltage since the DAQ is inherently current limited to about $20mA$. The DAQ used in this work is a National Instruments DAQ-6211 having $16bit$ resolution and an input/output sampling rate of up to $250kHz$ providing a very good platform for a versatile set of experiments.

3.1.2 Touchdown detection

In order to ascertain the head-disk clearance at a specified heater power, the touchdown power (TDP), i.e. the power to achieve zero-clearance or slider contact with the disk lubricant, needs to be determined. The TDP together with the knowledge of the slider's thermal actuation efficiency (fly-height loss per milliwatt, known from slider and heater design) is used to calculate and supply the appropriate heater power to achieve a desired head-disk clearance during operation. The TDP on the spin-stand test is determined using an automated Labview program that gradually increases the heater power while monitoring the AE sensor output in feedback. The power corresponding to a sudden jump in AE signal is defined as the TDP, and the heater power is automatically turned off upon touchdown detection. (Fig 3.3).

Transient test

Once the TDP is determined, the TFC heater is supplied a sinusoidal power waveform with a peak power above TDP. This test is helpful in evaluating the transient dynamics of the slider as the TFC protrusion comes into contact and moves out of contact. Four sinusoidal cycles (at $0.5Hz$ frequency) are used to understand the transient slider dynamics in contact and to evaluate its repeatability. The sinusoidal waveform is chosen (over other waveforms, such as a triangle, sawtooth or ramp) because it is smooth in power and voltage time derivatives. A representative power waveform for this test is shown in Fig 3.4

Dwell test

The longer term (tens of seconds to minutes) slider dynamics is evaluated by holding the TFC heater power fixed for a given duration below the TDP (i.e. backoff), at the TDP (i.e. contact), or above the TDP (i.e. overpush). This test is useful in understanding slider dynamics and its correlation to lubricant profile distribution/evolution under the TFC protrusion. A representative waveform for this test is shown in Fig 3.5

Disk RPM spin down test

Contact between the slider and the disk may also be established without TFC actuation by spinning down the disk RPM [Vangipuram Canchi and Bogy 2009]. A comparison between TFC induced contact and disk RPM spin-down induced contact is presented in this chapter.

3.2 Results and Discussion

3.2.1 Slider dynamics

Disk RPM spin down contact vs. TFC induced contact

The dynamics of traditional (non-TFC) sliders in contact has been extensively investigated in the past using the disk RPM spin down experiments [Kiely and Hsia 2006, 2008, Knigge and Talke 2001, Vangipuram Canchi and Bogy 2009, Wang et al. 2001]. Slider dynamics resulting from TFC induced contact, where contact only occurs at the thermal protrusion, is expected to be significantly different because the contact of area is much lower. To understand this difference, a disk RPM spin down test is conducted by treating the TFC slider as a traditional slider (i.e. no power is supplied to the TFC heater), and the slider's vertical dynamics under contact is monitored. The slider's dynamics are then compared to that resulting from TFC induced contact by conducting a transient test.

Fig 3.6 shows the change in vertical displacement and velocity when a TFC slider (with ABS-1 design shown) is brought into contact using the disk RPM spin down test. The RPM is first decreased from 7200RPM to 500RPM and subsequently increased back to 7200RPM.

As the disk RPM is decreased, the AE signal shows a sudden rise marking the onset of contact. Correspondingly, the slider's vertical velocity and displacement also show a sudden increase suggesting vigorous slider motions during contact. The slider's vertical bouncing displacements during contact are very large ($300nm$) making it impossible to perform successful read-write operations. Contact between the slider and the disk may cause slider bouncing/pitching severe enough to bring even the leading edge into contact with the disk. The joint frequency time (JFT) plot is constructed to monitor how the slider's vertical velocity spectrum and the AE signal spectrum change when it is brought into contact. As evident from Fig 3.7, contact causes the slider to vibrate vigorously with the dynamics spanning a broad frequency range. The AE signal also picks up energy over the broad frequency range.

Slider vertical vibrations during the first sinusoidal pulse of the transient test, which brings the thermal protrusion into contact, is shown in Fig 3.8 for a slider with ABS-1. Comparing the results of TFC induced contact with those of RPM induced contact (Fig 3.6), it is evident that slider vibrations are significantly lower (by nearly two orders of magnitude) for the TFC induced contact. The slider's vertical bouncing displacements is highest for heater powers just above TDP and is only slightly higher than the baseline flying condition. The lower contact area between the slider's thermal protrusion and the disk results in lower contact forces and hence lower slider vibrations. Interestingly, it is observed that the slider vibrations as well as AE signal are lower in the overpush condition than at powers just above the TDP.

The JFT plot for the slider's vertical velocity and AE signal are shown in Fig 3.9 for the case with TFC induced contact. The slider dynamics are concentrated at certain well

defined frequencies/modes in this case. In comparison, the dynamics is spread over a very broad frequency range in the case of disk RPM spin down induced contact (Fig 3.7). When TFC induced contact initiates (i.e around the TDP), the slider's vertical bouncing occurs at $128kHz$ (first pitch mode) and its harmonics at $256kHz$ and $384kHz$. As pointed earlier, the slider's bouncing is highest during this phase. For powers higher than the TDP (i.e in overpush), the slider shows only a weak response at $260kHz$ and $310kHz$ and the slider's bouncing is also lower. The AE signal spectrum shows frequencies also seen in the slider's velocity spectrum in addition to other frequency peaks that are characteristic to the AE sensor itself.

The above results indicate that a HDI with TFC induced contact is much more robust than the HDI of a traditional (non-TFC) sliders in contact. The transient dynamics of the slider are further investigated using sliders with different ABS designs.

Effect of ABS design

Fig 3.10 and Fig 3.11 show the vertical dynamics under contact for ABS-1 and ABS-2, respectively. The results for ABS-1 compare with those presented in the previous section. The important distinction between the response of the two designs is that while increasing the heater power beyond the TDP causes slider vertical dynamics as well as AE signal magnitudes to suddenly get suppressed in the case of ABS-1, such a phenomenon does not occur for ABS-2. The JFT plots show that the slider dynamics for ABS-1 undergoes sudden change in frequency/modes as the TFC power is increased to TDP and beyond. Specifically, this experiment shows the excitation at the first pitch mode (at $f_1 = 128kHz$) and its second harmonic ($2f_1$)) at contact, but it quickly shifts to another dominant mode (at $f_2 = 233kHz$) in slight overpush, followed by very weak excitation (around $f_3 = 260kHz$) in strong overpush. In contrast, ABS-2 does not exhibit such sudden changes and shows very strong content around $310kHz$ in strong overpush. The difference in the behavior of the two designs may be attributed to the difference in the slider's form factors, ABS design as well as heater induced thermal protrusion profiles. The interesting phenomena of suppression of AE signal and slider dynamics for ABS-1 in strong overpush indicates the highly nonlinear nature of the HDI under TFC induced contact and it requires further investigation.

Hysteresis studies for slider vibrations and AE signal

The repeatability of the slider dynamics as well as AE signal contact may be verified using the hysteresis plots that show the change to the vertical vibration and the AE signal as a function of the TFC power. Fig 3.12 and Fig 3.13 show the hysteresis plots for ABS-1 and ABS-2 respectively. It is seen that the first cycle of the transient test is different from the subsequent three cycles which show almost the same signature. Strong hysteresis signature (contact ceases during 'power-down' at lower TFC power compared to the contact onset during 'power-up') is observed during the first cycle of the transient test suggesting strong slider-lubricant interactions when the slider first comes into contact with the disk lubricant. It is noted that the contact onset power (i.e. TDP) during the 'power-up' is not significantly different among the four cycles implying that the HDI is fairly robust to short durations of contact and overpush.

3.2.2 Slider-lubricant interactions

Transient test

OSA scans are used to monitor the lubricant profile changes under the TFC protrusion after transient tests and dwell tests. A lighter color indicates lubricant depletion and a darker color indicates lubricant accumulation. Fig 3.14 shows the change in the lubricant under the TFC protrusion as a result of conducting a transient test. In general, contact with the lubricant during the transient tests causes lubricant rippling and some lubricant depletion, which increases with the duration of contact. The changes to the lubricant during the transient test are larger for ABS-2, and it correlates well with the stronger slider dynamics for ABS-2.

The rippling frequencies of the lubricant and the frequencies that appear in the slider's velocity spectrum due to TFC induced contact are plotted in Fig 3.15 for ABS-1 and ABS-2. It is observed that for ABS-2, which has strong slider dynamics, the lubricant rippling also occurs close to the slider's dominant excitation frequency. The lubricant is negligibly affected by contact for tests with ABS-1, and hence the lubricant frequency spectrum also does not show any evident signature.

Dwell test

Tests are conducted to understand the change occurring in the disk-lubricant as well as contact and slider dynamics for longer duration of contact. Dwell tests are conducted by flying the slider for 5 to 20 minutes with the TFC power set for back-off, slight contact and overpush conditions.

For a 20 minute dwell test with ABS-1 in $10mW$ overpush, Fig 3.16 shows the AE signal and the lubricant change for each 2 minute time increment. The lubricant ripples and depletes with contact, and the change in the lubricant is negligible when there is no AE detected contact (between 5 and 11 minutes).

Fig 3.17a and Fig 3.17b show the lubricant change after 5 minutes of dwell test using ABS-1 and ABS-2, respectively. It is evident that the lubricant change is lower for ABS-1 compared to ABS-2, and in both cases, increasing overpush (interference) causes larger lubricant change.

An interesting phenomenon of lubricant pooling and its transport down the track is observed during the dwell tests using ABS-2. Fig 3.18 and Fig 3.19 show the results for lubricant evolution with time for $3mW$ and $7mW$ overpush cases, respectively, and the pooled lubricant (dark color) moves down the track with time. The average speed of movement is about $0.52mm/s$ for $3mW$ overpush and $1.17mm/s$ for $7mW$ overpush.

Thermal protrusion contact every revolution with the pooled lubricant is responsible for this small downtrack motion of the lubricant and the resulting transport mechanism. It is confirmed that contact (as opposed to air shear forces acting on the lubricant) is the main reason for this transport. As shown in Fig 3.20, the transport of the pooled lubricant stops once the TFC power is turned 'off' and the slider is flown passively over the track.

Enhanced slider-lubricant interactions under TFC induced contact pose a serious challenge to HDI performance and further investigations are required to understand their effect on slider dynamics as well as disk lubricant redistribution. In addition it is important to

translate this understanding into criteria helpful for designing a HDI that can accommodate contact.

3.2.3 Simulations

ABS reconstruction using a profiler

In order to conduct simulations, the ABS-1 design is 'reverse engineered' from the experimental parts. An optical microscope capable of 1000× magnification is used to determine the rail dimensions, and a Tencor P-10 surface profiler is used to measure the wall profiles and etch depths. The reconstructed ABS (Fig 3.21) is used for computational investigations performed using in-house CMLAir air bearing software codes.

Flying attitude predictions

The simulation predictions for the flying attitudes using the CMLAir static code [CMLAir 2007] are shown in Fig 3.22 for the case with no thermal protrusion. These simulations are performed at the product design conditions: 7200RPM and at the radius/skew conditions shown in Table 3.1. The results for the fly-height at the trailing edge center (TEC), pitch and roll are also tabulated.

Another simulation is performed to understand the effect of thermal protrusion on the flying attitude of the slider. In reality, the thermal protrusion is highly dependent on the material properties, heater design and heater location. The air flow over the ABS and the resulting cooling also have significant effect on the actual thermal protrusion profile. The CMLAir TFC code [Zheng and Bogy 2009] uses an automated iterative approach between the CMLAir static code and ANSYS slider-heater geometry files to compute the exact thermal protrusion profile for particular slider-ABS-heater combinations under different flying conditions and TFC heater powers. This process, while being very accurate, is computationally expensive. Since the objective of the current work is to understand the effect of thermal protrusion on the slider's flying attitude, an alternate simplified approach is employed. A representative deformation profile with $10nm$ maximum thermal protrusion (Fig 3.23) is used as an approximation and scaled up or down as required to simulate larger or smaller protrusion profiles.

Table 3.2 shows the slider's flying attitude with increasing thermal protrusion and the results are plotted in Fig 3.24. The minimum fly-height (physical spacing or the smallest slider-disk clearance) occurs at the read-write transducer location (tip of the protrusion bulge) and it decreases with increasing thermal protrusion. At $34nm$ protrusion, the minimum fly-height reduces to $1.54nm$ which is below the glide height of the disk surface and is to be interpreted as slider-disk contact. The decreasing pitch and increasing TEC fly-height indicate that the slider body as a whole flies slightly higher than the case without thermal protrusion. However, the physical spacing at the read-write head is reduced because the protrusion bridges the gap between the slider and the disk.

Comparison of simulation fly-height and experimental fly-height

A comparison is performed to verify the agreement between the simulated and experimental results. All results correspond to a condition that is equivalent to 0^o skew at $29.25mm$ radius (corresponds to design condition in an actual product). The design RPM for this slider 7200RPM and the corresponding linear velocity at this radius is $22m/s$.

The slider's fly-height at the TEC is obtained from simulations at different disk RPMs and compared to the experimental results. The experimental fly-height of the slider is estimated by finding the TDP at different disk RPMs. The TDP is converted into an estimated fly-height using a calculated value of the thermal protrusion efficiency (fly-height loss per milliwatt of heater power). This efficiency is calculated as the ratio of the simulated fly-height ($11.63nm$ at 7200RPM) to the experimental TDP at 7200RPM. The results of two experiments and those from simulation are shown in Fig 3.25. A reasonable agreement is obtained between the experimental and simulation predicted trends in the fly-height changes with linear velocity (disk RPM), but there is quantitative disagreement between the results. This disagreement most likely arises because of errors in the ABS model reconstruction. The slider's flying attitude is very sensitive to the etch depth, rail geometries and wall profiles. Additionally, it is pointed out that the simulation fly-heights are at the slider's TEC, while the touchdown occurs at a location under the read-write head, which is about $50\mu m$ from the slider's TEC. The qualitative agreement between the results gives reasonable confidence in the reconstructed ABS model, and it is used for further simulation studies to understand the air bearing dynamic performance for conditions with thermal protrusion.

Air bearing parameter identification with thermal protrusion

The CMLAir Parameter Identification Program (PIP) code [Zeng and Bogy 1997] is an automated program that estimates air bearing system parameters, the mode shapes and the natural frequencies based on impulse response analyses of the system. The effect of thermal protrusion on the system parameters requires important consideration as it helps predict and understand the dynamic response of the system. Fig 3.26 shows the air bearing modes for the case with no thermal protrusion. The nodal lines corresponding to the slider's three natural modes, namely, roll, first pitch and second pitch modes are marked with their corresponding natural frequencies at $78.41kHz$, $97.67kHz$ and $272.52kHz$, respectively.

Fig 3.27 shows the effect of thermal protrusion on the slider's natural frequencies and damping. While the roll and first pitch frequencies are relatively unaffected by the thermal protrusion, the second pitch frequency increases significantly (by about 25%) with increasing thermal protrusion. This increase in the slider's second pitch frequency is expected: as the thermal protrusion increases, the pressure under the protrusion, and hence the effective stiffness at the trailing end increases, resulting in a higher natural frequency. This phenomenon (which does not occur for traditional non-TFC sliders) requires special attention in the analysis of TFC sliders because thermal protrusion can potentially alter the slider's dynamic response.

It is noted that the thermal protrusion does not significantly alter the mode shapes for this particular ABS design. Fig 3.28 shows the mode shapes for the case with $30nm$ thermal protrusion and it compares well with that in Fig 3.26 for the case with no thermal protrusion.

Comparison of the predicted natural frequencies with experiments

Experiments show that when the TFC slider comes into contact with the disk lubricant, the dominant frequency of excitation is the first pitch mode at $\approx 128kHz$ for this ABS design (Fig 3.9). The simulations, however, under predict the first pitch mode frequency for the near contact condition. For $30nm$ protrusion, the minimum fly-height is $2.48nm$ (i.e near contact condition considering that the glide-height of the disk is around $2nm$), and the slider's first pitch mode is predicted to be $101.17kHz$. The difference in the predicted and experimental values indicate that the reconstructed ABS does not accurately represent the experimental part. Separately, it is pointed out that the CMLAir PIP code only estimates the linearized system parameters, and hence the results are expected to deviate from the experimental results for the fairly nonlinear air bearing system considered here, especially when small clearances owing to thermal protrusion are involved.

3.3 Conclusion

Experiments are successfully conducted using TFC sliders by instrumenting the current spin stand set-up with a versatile power supply hardware which has good resolution. The ability to conduct automated touchdown detection as well as testing methods to understand the transient and longer term slider dynamics and disk lubricant changes are developed. The slider vibrations under TFC induced contact are much lower than would occur if the slider is brought into contact with the disk through a disk RPM reduction. The slider dynamics are also concentrated at specific modes/frequencies during TFC induced contact compared to a broad band excitation of the dynamics for contact induced by disk RPM reduction.

The changes to the disk lubricant under TFC induced contact are observed and correlated with the slider dynamics. Slider lubricant contact at the thermal protrusion, in general, causes lubricant rippling and depletion which increases with the duration of contact. Interesting phenomena of lubricant accumulation and its motion down the disk track due to contact with the thermal protrusion are observed and reported. Further investigations on the effect of lubricant parameters (type, thickness, bonding ratio etc) on slider dynamics and disk lubricant redistribution require examination.

Simulations are conducted using an ABS whose geometry is reconstructed from measurements using optical microscopy and surface profilers, and the results are compared to the experiments. While a general agreement in trends is observed, the inherent limitations of the measurement and reconstruction techniques result in some quantitative disagreement in the simulated static fly-height results. The simulations are nevertheless helpful in gaining important insights into the static and dynamic performance of TFC sliders under thermal protrusion. Specifically, the parameter estimation analysis shows an interesting result that while the thermal protrusion does not significantly alter the slider's vibration modes or the slider's roll frequency and first pitch frequency, the second pitch frequency increases considerably with increasing protrusion.

Radius mm	Skew $deg.$	TEC fly-height nm	Pitch $\mu rad.$	Roll $\mu rad.$
18.5	-16.896	11.36	111.23	7.74
29.25	0	11.63	137.01	11.63
32.02	3.183	11.50	138.25	19.65
45.58	16.317	13.40	135.62	-13.68

Table 3.1: Simulated results for the reconstructed ABS-1 design without thermal protrusion

Thermal protrusion nm	TEC fly-height nm	Min. fly-height nm	Pitch $\mu rad.$	Roll $\mu rad.$
0	11.63	11.05	137.01	11.63
5	14.17	10.35	132.59	13.33
10	16.96	9.40	127.51	14.98
14	19.30	8.31	122.30	18.36
18	21.79	6.72	120.32	11.18
24	25.73	4.41	112.83	12.78
30	30.10	2.48	106.26	11.76
34	33.36	1.54	101.24	11.07

Table 3.2: Simulated results for the slider's flying attitude as a function of TFC protrusion

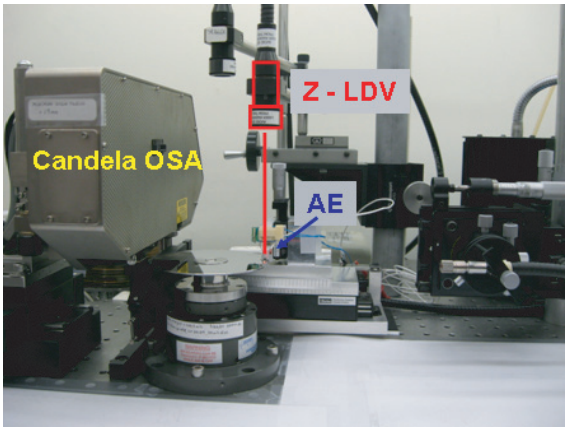

Figure 3.1: The spin stand experimental set-up

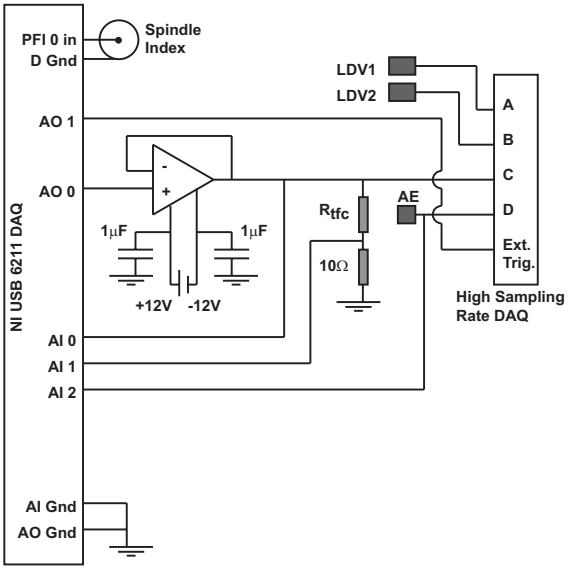

Figure 3.2: Electrical circuit diagram

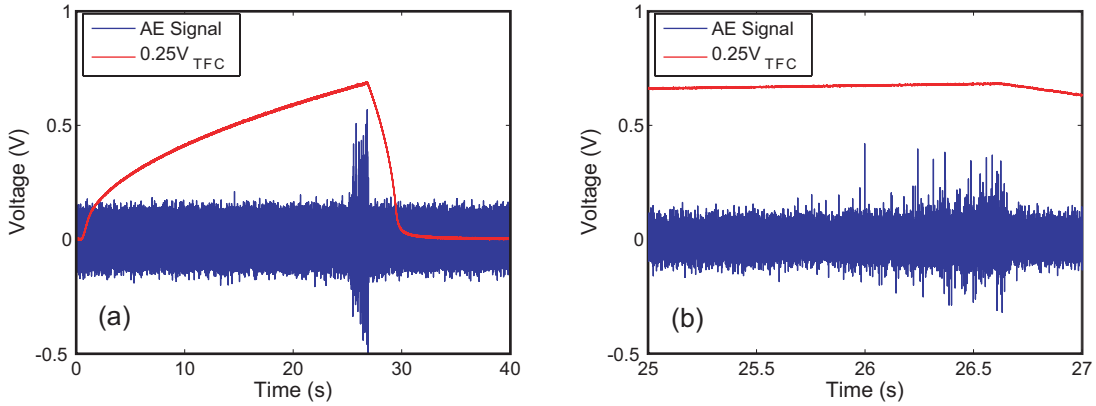

Figure 3.3: (a) Touchdown detection plot (b) Zoomed section of the touchdown detection plot

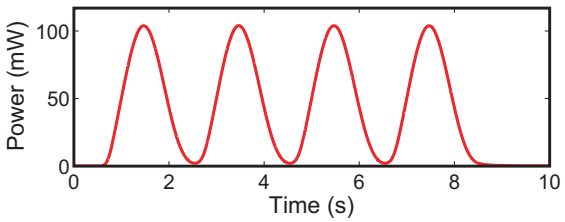

Figure 3.4: Representative power waveform for the transient test

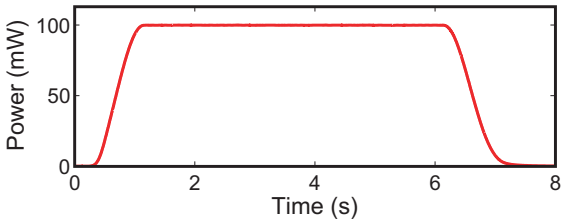

Figure 3.5: Representative power waveform for the dwell test

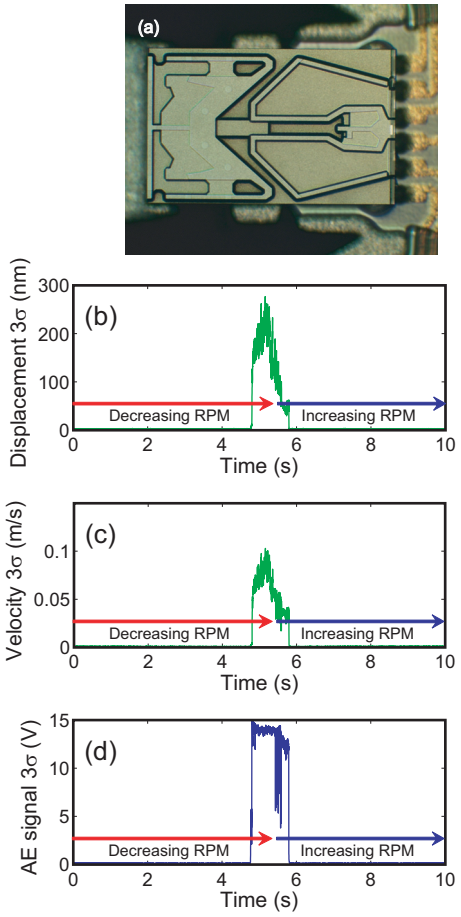

Figure 3.6: (a) Slider ABS-1 design (b) Vertical displacement 3σ (c) Vertical velocity 3σ (d) AE signal 3σ

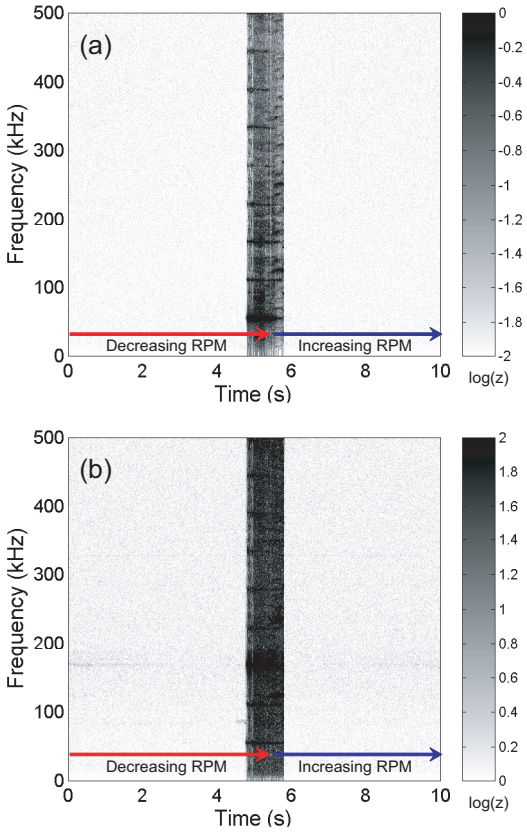

Figure 3.7: (a) JFT of vertical velocity (b) JFT of AE signal

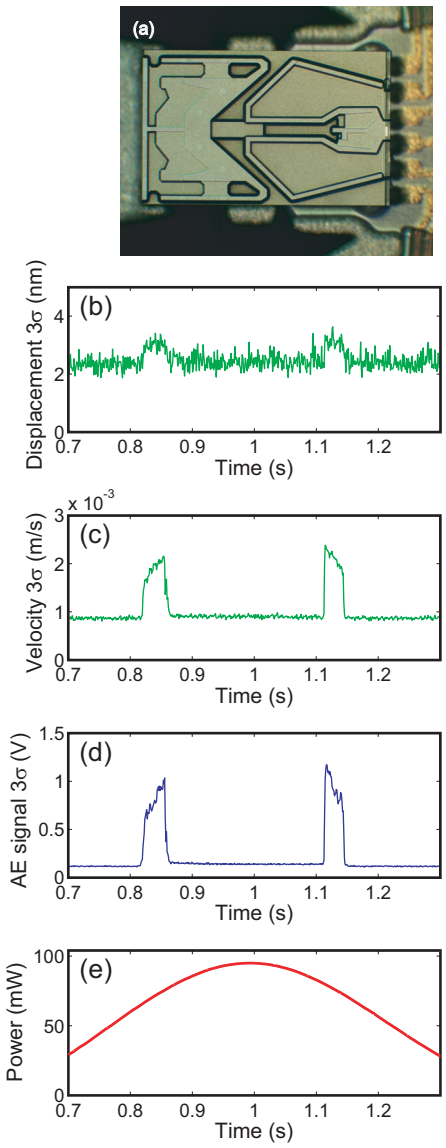

Figure 3.8: (a) Slider ABS-1 design (b) Vertical displacement 3σ (c) Vertical velocity 3σ (d) AE signal 3σ (e) TFC heater power

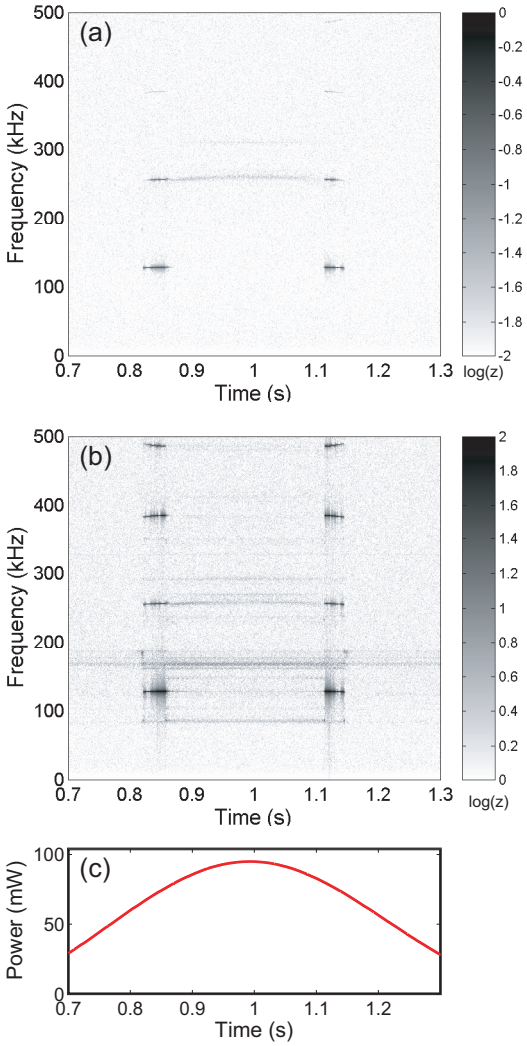

Figure 3.9: (a) JFT of vertical velocity (b) JFT of AE signal (c) TFC heater power

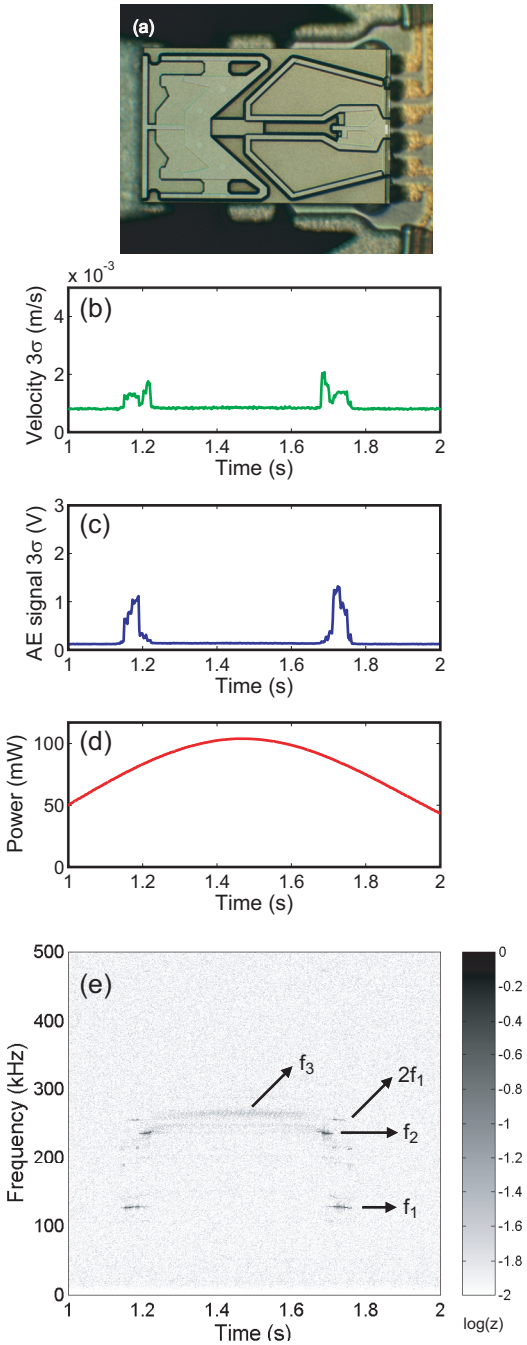

Figure 3.10: (a) Slider ABS-1 design (b) Vertical velocity 3σ (c) AE signal 3σ (d) TFC heater power (e) JFT of vertical velocity

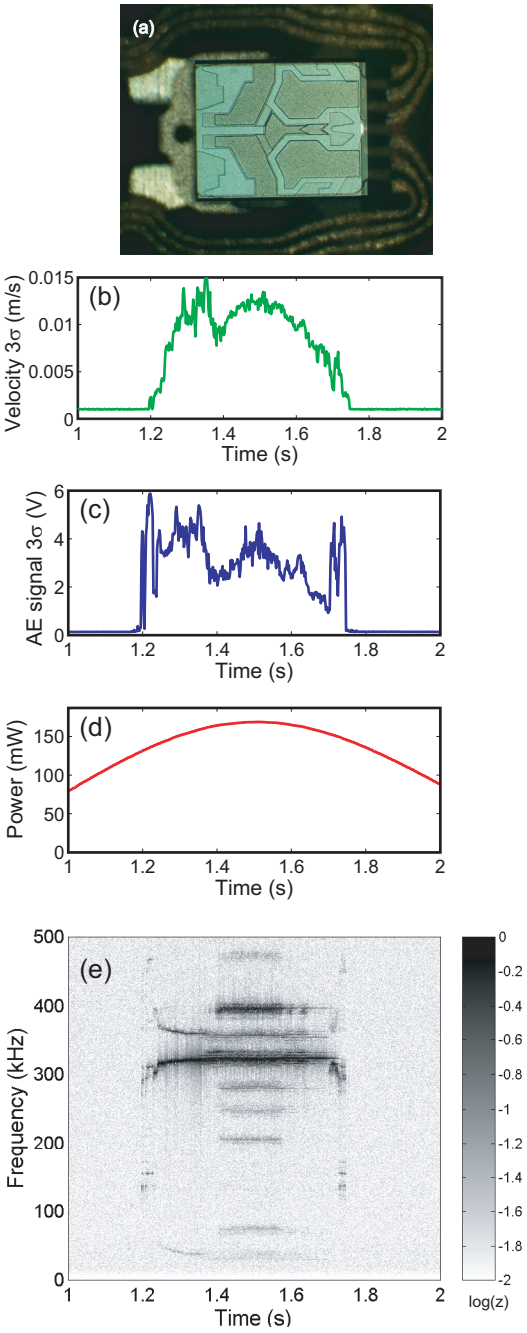

Figure 3.11: (a) Slider ABS-2 design (b) Vertical velocity 3σ (c) AE signal 3σ (d) TFC heater power (e) JFT of vertical velocity

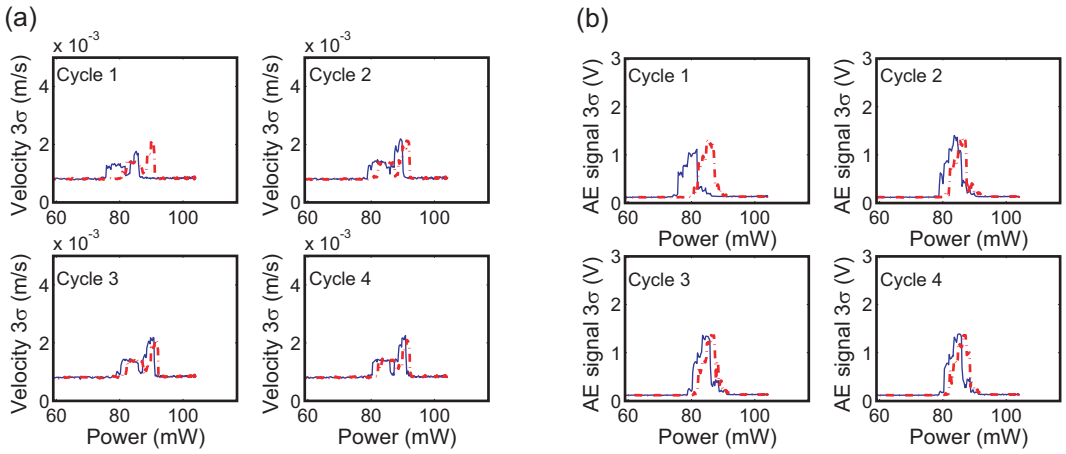

Figure 3.12: Hysteresis plots for the four cycles of the transient test using ABS-1 (a) Vertical velocity 3σ (b) AE signal 3σ; $-\cdot-$ power up ; — power down

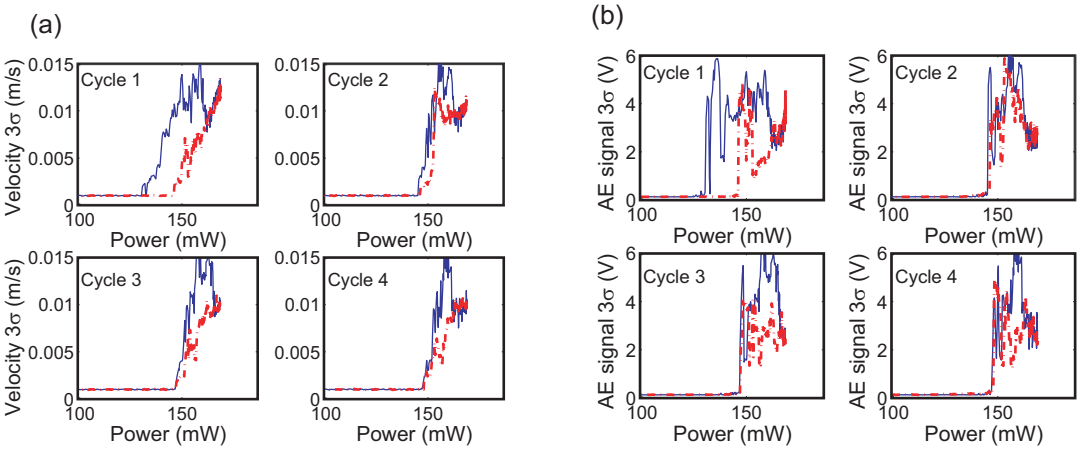

Figure 3.13: Hysteresis plots for the four cycles of the transient test using ABS-2 (a) Vertical velocity 3σ (b) AE signal 3σ; $-\cdot-$ power up ; — power down

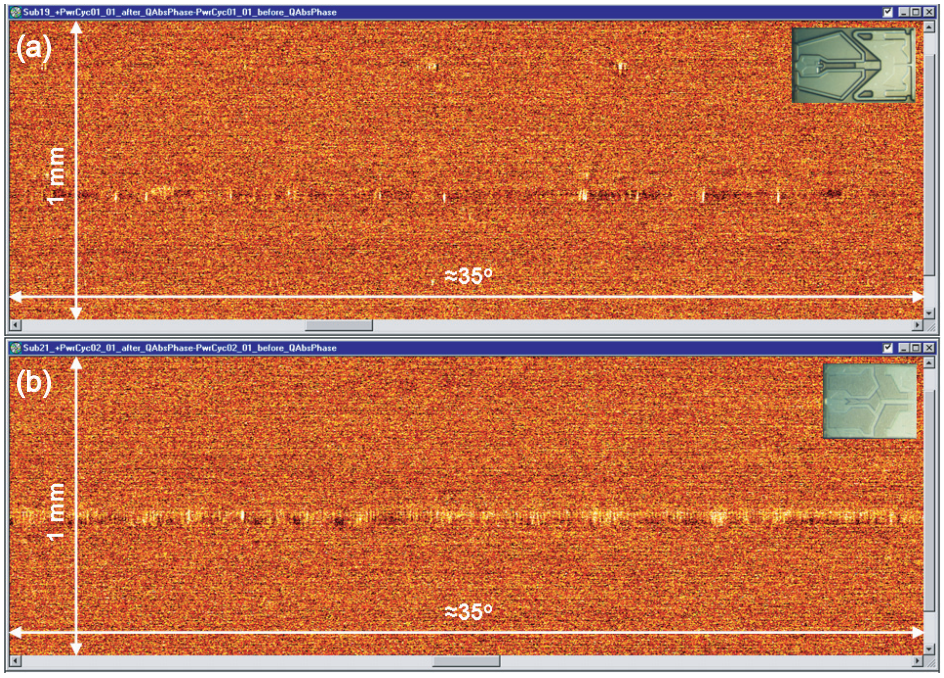

Figure 3.14: Lubricant change due to transient test for different slider ABS designs (a) ABS-1 (b)ABS-2

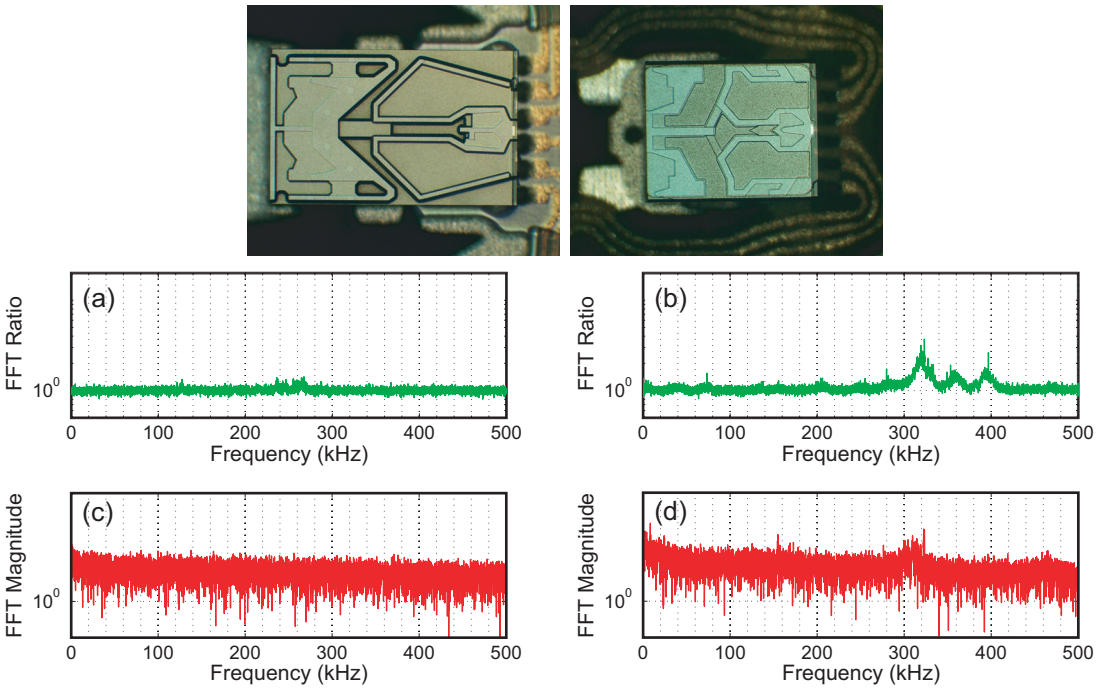

Figure 3.15: Ratio of velocity FFT magnitude for condition with contact over condition without contact for (a) ABS-1 (b) ABS-2. Lubricant rippling frequencies after transient test for (c) ABS-1 (d) ABS-2

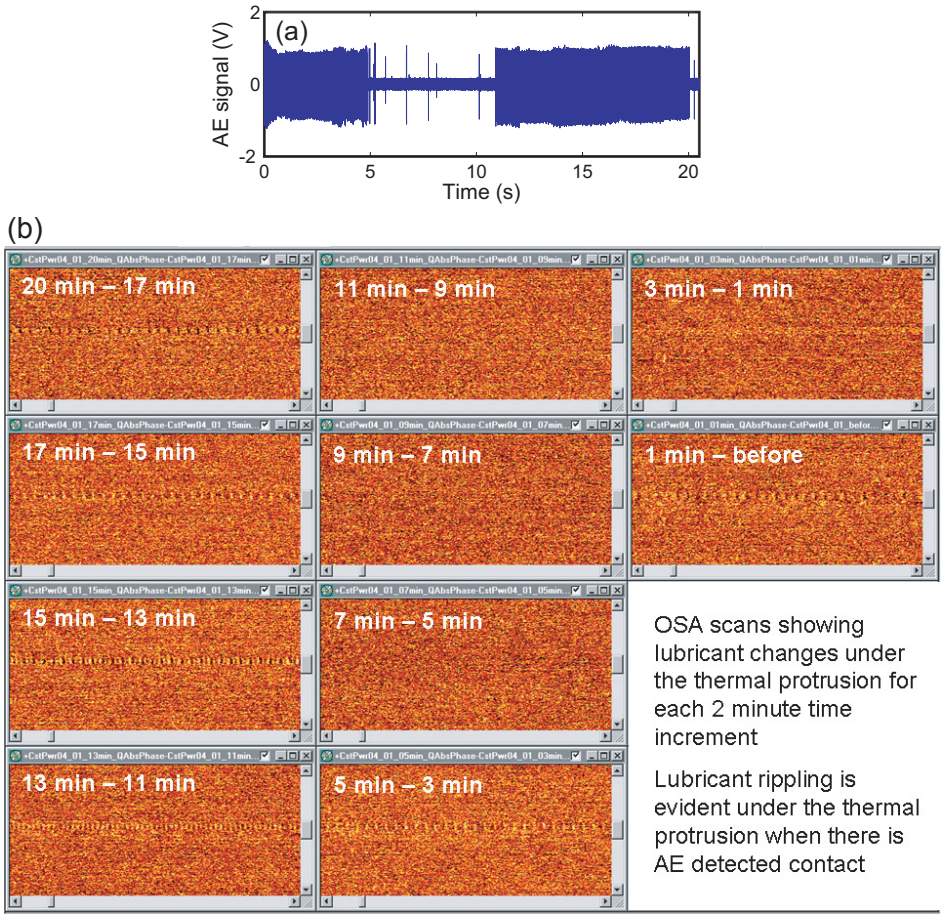

Figure 3.16: (a) AE signal time history for a 20 minute dwell test (b) Lubricant change for each 2 minute increment

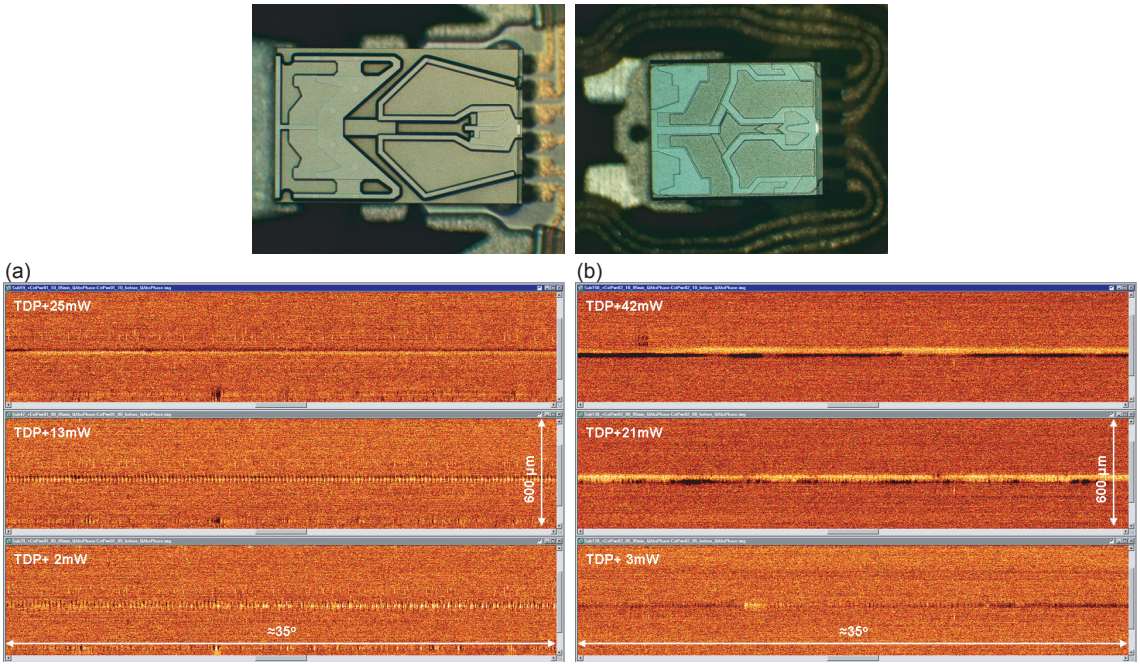

Figure 3.17: Lubricant change after a 5 minute dwell test at different overpush power (a) Slider ABS-1 design (b) Slider ABS-2 design

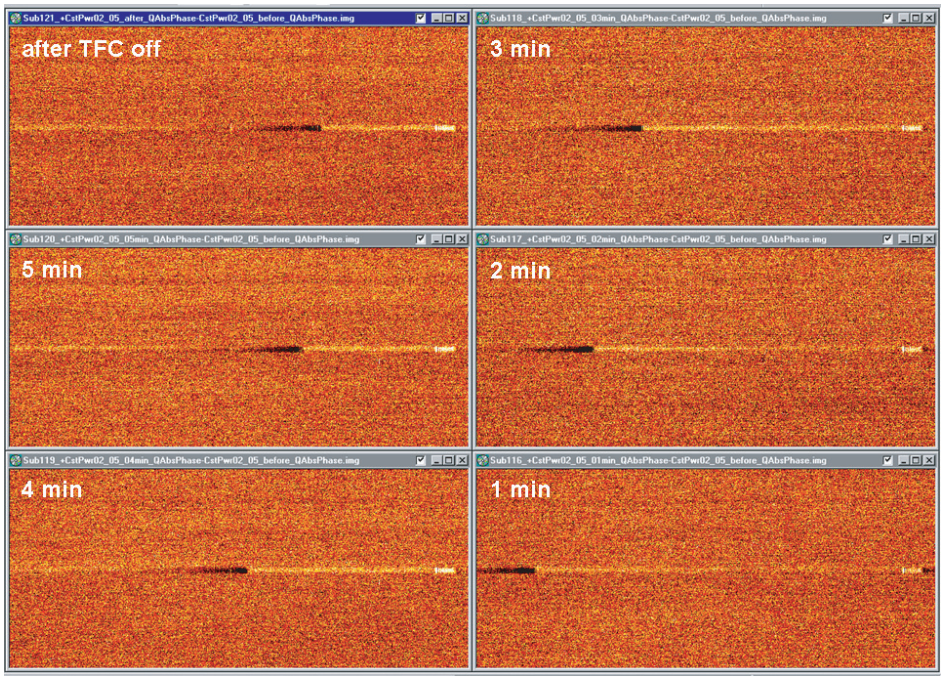

Figure 3.18: OSA scans showing lubricant pooling and transport for a 5 minute dwell test with $3mW$ overpush using ABS-2

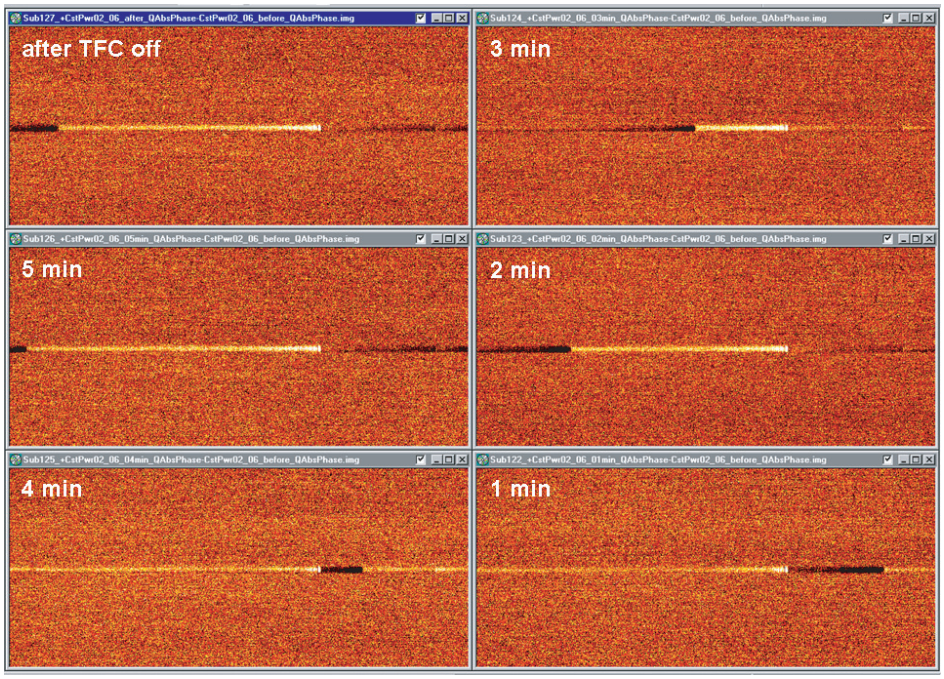

Figure 3.19: OSA scans showing lubricant pooling and transport for a 5 minute dwell test with $7mW$ overpush using ABS-2

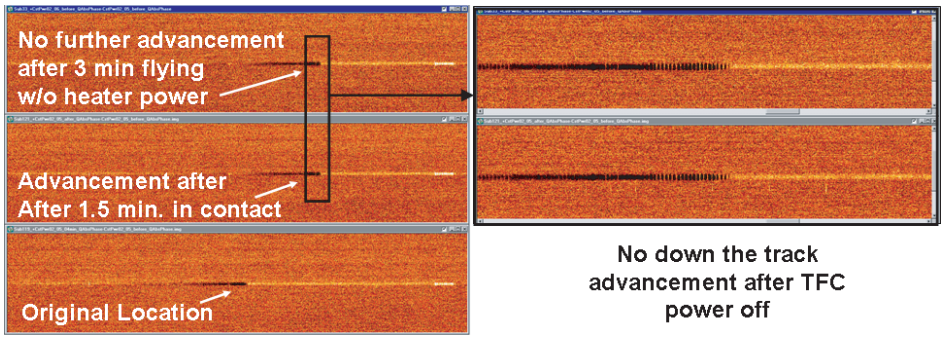

Figure 3.20: OSA scans showing that the transport of pooled lubricant stops without TFC contact

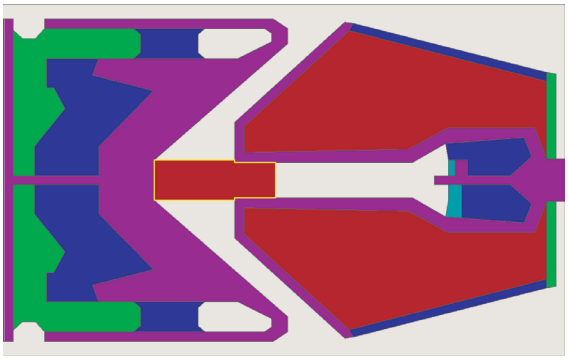

Figure 3.21: Reconstructed ABS-1 model for CMLAir simulations

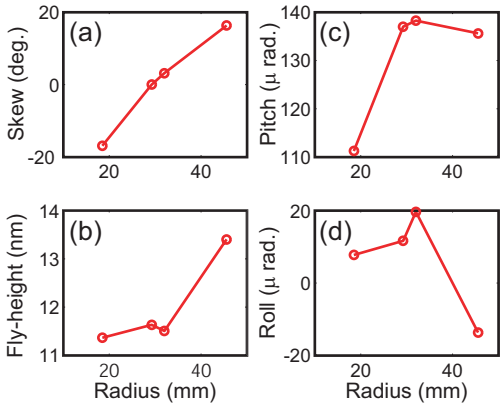

Figure 3.22: Simulation results for ABS-1 at 7200 RPM with no thermal protrusion (a) Skew-radius relationship (b) Fly-height at the trailing edge center (c) Pitch (d) Roll

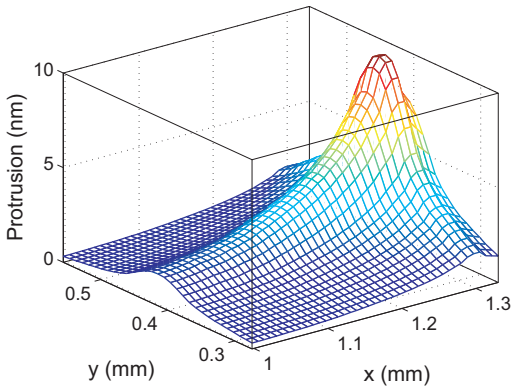

Figure 3.23: Representative thermal protrusion profile with $10nm$ maximum protrusion

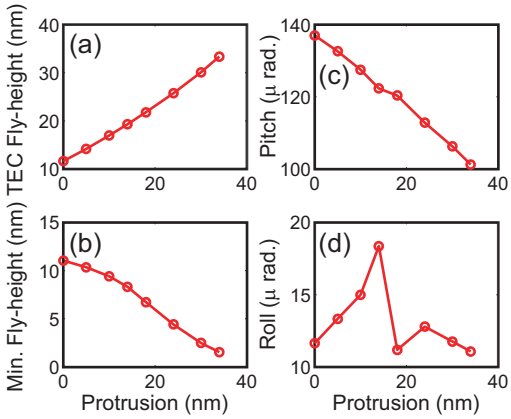

Figure 3.24: Simulation results for ABS-1 with thermal protrusion at 7200 RPM, $29.25mm$ radius and 0^o skew (a) Fly-height at the trailing edge center (b) Minimum fly-height (c) Pitch (d) Roll

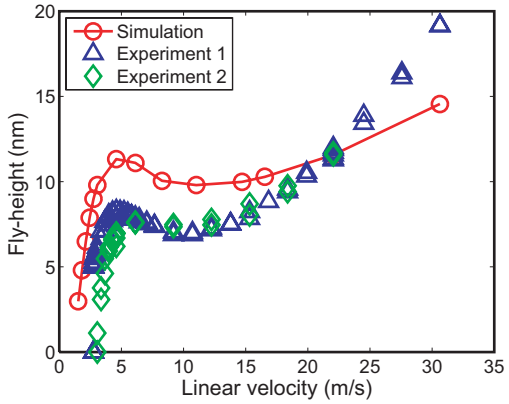

Figure 3.25: Comparison of experimental and simulation fly-height for ABS-1 at different disk linear velocity

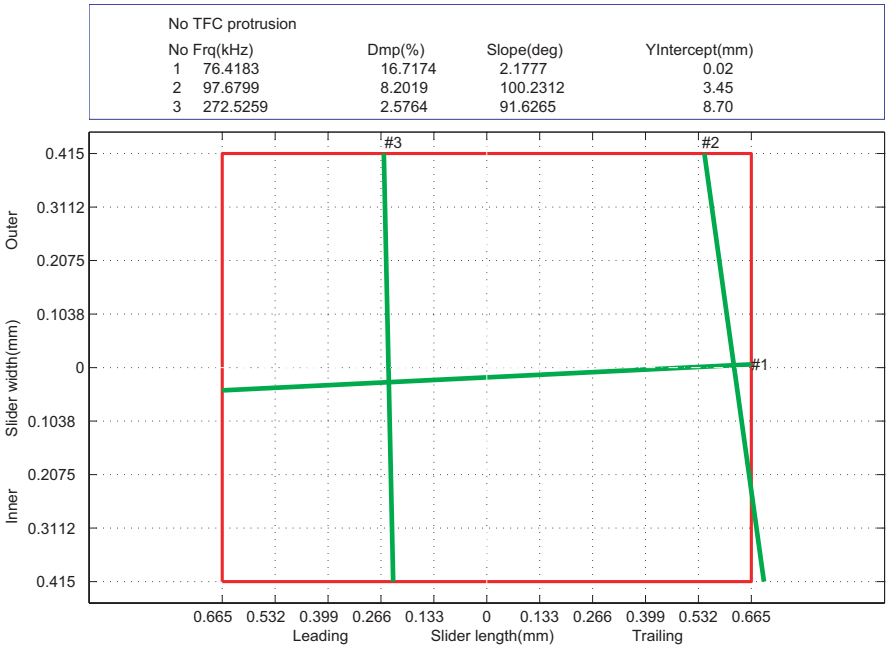

Figure 3.26: Simulated nodal lines for ABS-1 with no thermal protrusion

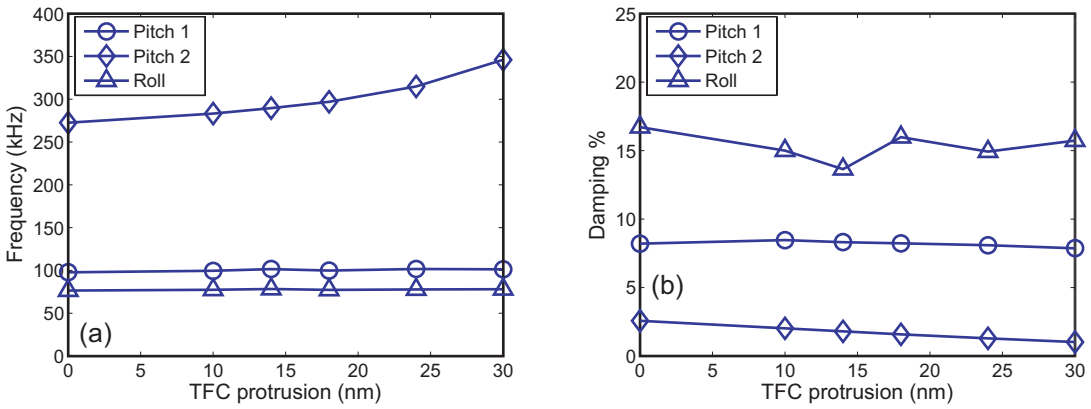

Figure 3.27: Effect of thermal protrusion on the air bearing (a) natural frequency (b) damping ratio

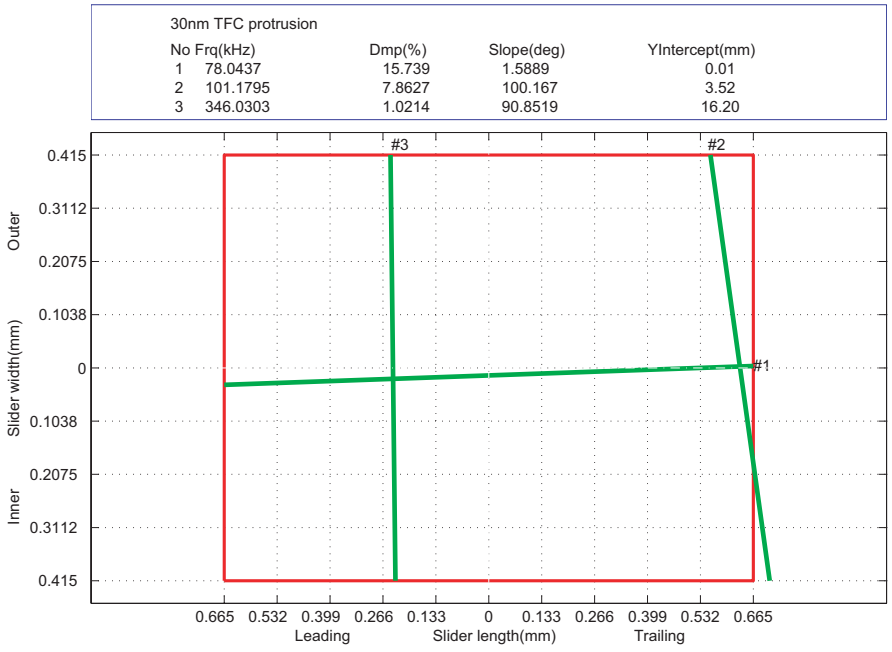

Figure 3.28: Simulated nodal lines for ABS-1 with $30nm$ maximum thermal protrusion

Chapter 4

Thermal Fly-height Control Slider Dynamics in the Lubricant Contact Regime

The experimental capabilities developed to successfully investigate thermal fly-height control (TFC) slider dynamics are presented in Chapter 3. In this chapter, TFC sliders that are capable of subnanometer level actuation are used to investigate the 3D (vertical, down-track and off-track) slider dynamics in slider-disk lubricant contact. The motivation is to further explore the proposed recording strategy where a portion of the TFC protrusion is in intermittent or continuous contact with the lubricant layer of the disk [Liu et al. 2008]. It is observed from the current work that slider-lubricant contact introduces significant excitation in all three directions, and the slider dynamics is dependent on the degree of lubricant contact. The lubricant surface has a significant role in determining the physical spacing (clearance) and slider fly-height. While slider-lubricant contact may be successfully achieved by carefully controlling the heater power, improved slider designs and associated heater induced protrusion profiles are necessary to successfully mitigate contact induced vibrations and meet the challenges for future hard disk drives.

4.1 Experiments

The experiments are performed with 'pemto' TFC sliders ($1.25mm \times 0.85mm$) on a $95mm$ media coated with 13Å perfluoropolyether (PFPE) lubricant (60% bonded ratio). Slider vibration is measured using Laser Doppler Vibrometer (LDV), contact at the HDI is monitored using an Acoustic Emission (AE) sensor, and lubricant profile changes are measured using an *in-situ* Optical Surface Analyzer (OSA) (Fig 4.1). Power to the slider's heater is supplied using a data acquisition board and amplifier circuit controlled by a custom written Labview code. The power input system offers the flexibility of supplying programmable waveforms together with submilliwatt power resolution. The touchdown power (TDP) is measured using an automated program that gradually increases the heater power using AE signal as feedback. The power corresponding to a sudden jump in the AE signal is defined as the TDP, and the heater power is automatically turned off upon touchdown detection (Fig 4.2a). The difference in the lubricant profile after and before the test shows changes at

discrete locations under the protruded center-pad and sometimes under the side-pad (owing to slider roll) where slider-lubricant contact occurs (Fig 4.2b).

4.1.1 Establishing slider-lubricant contact

Since the objective of this work is to investigate slider dynamics in contact with the lubricant, experiments are first conducted on a partly delubed disk to establish slider-lubricant contact. Delubing is performed by immersing part of the disk in a HFE solution for 10 minutes. The section of the disk immersed in the HFE is stripped of the 'mobile' and some 'bonded' lubricant and is left only with a 'bonded' lubricant layer. Therefore, it has a lower lubricant thickness than the lubed section. Assuming 50% lubricant removal, the thickness difference between the lubed and delubed sections would be about 6.5Å. In this work, results are reported for a slider flown over a test track that has 75% lubed and 25% delubed sections.

The experimental procedure is as follows: The slider is loaded and flown passively (no heater power) for 20 minutes on the experimental track. The TDP is measured. The slider is then subject to an input power profile (Fig 4.3a) with a dwell time of 5 seconds at the maximum power. The maximum power is varied from 0.8TDP to 1.3TDP in steps of $2.5mW$, and the slider's vertical velocity is captured at a $1MHz$ sampling rate. OSA scans of the disk surface before and after the test are used to monitor the change in lubricant profile. All tests are performed at 0^o skew and design linear velocity of $22m/s$ unless mentioned otherwise.

4.1.2 Slider dynamics under lubricant contact

Once the conditions that correspond to slider-lubricant contact are established, detailed investigations are carried out to understand the effect of lubricant contact on the three dimensional slider dynamics (vertical, down-track and off-track) by flying the slider on a fully lubed disk. For simplicity, the directions normal to the slider's faces are referred to as the down-track and off-track directions, even for nonzero skew. The power profile (Fig 4.3b) input to the heater for these investigations consist of four cycles of a sine waveform with a time period of two seconds.

4.2 Results and Discussion

4.2.1 Establishing slider-lubricant contact

The touchdown power for the experiments on a partly delubed disk is determined to be $77mW$. When the heater maximum power is $3mW$ above TDP (Fig 4.3a), the slider contacts only the lubed section of the disk (Fig 4.4). As shown in the schematic (Fig 4.5), such a condition reflects contact with only the mobile lubricant. Tests for repeatability confirm that such a condition of contact with only the mobile lubricant layer can be established when the heater power is slightly above the TDP.

This experiment shows that the slider flies with a lower clearance from the lubricant top surface in the lubed section of the disk compared to the top surface in the delubed section of the disk (Fig 4.5). This decrease in clearance may be attributed to molecular

nonuniformity/rough nature of the mobile lubricant layer in the lubed section. For a slider flying at a given clearance from the mean lubricant surface, the extended backbones of the mobile lubricant or areas of thicker lubricant films can come into strong interaction/contact with the slider if the nonuniformity/roughness is sufficiently large. Based on the experimental observations, it is inferred that the lubricant nonuniformity/roughness (or viewed differently, the glide height) of the mobile lubricant (lubed section) is higher than that for the bonded lubricant (delubed section), and hence the clearance is lower in the lubed section.

Interestingly, based on surface energy arguments, lubricant nonuniformity/roughness should lead to a reduction in clearance. It is well known that the disk surface energy is strongly influenced by the thickness of the lubricant (the dispersive part varies inversely as the square of the lubricant thickness; the polar part has a different dependence on lubricant thickness [Tyndall et al. 1998, Waltman 2004]). Therefore, the total surface energy of a nonuniform lubricant film averaged over an area will be greater compared to that for a uniform lubricant film of the same mean thickness, and this increase in surface energy, in effect, tends to reduce the clearance. It is envisioned that deliberate patterning/roughening of the lubricant may be used to reduce the clearance, provided the patterning/roughening is chosen optimally to avoid enhanced slider-lubricant interactions at the thickest lubricant areas and the reliability of the HDI can be ensured.

When the heater power is increased to $13mW$ above TDP, slider contact is established with the lubed and delubed sections of the disk (Fig 4.6). Contact with the delubed section is assumed to be contact with only the bonded lubricant, while contact with the lubed section at this power is contact with the top mobile plus underlying bonded lubricant layer.

The change in slider dynamics during lubricant contact is indicated by the spectrum of the slider's vertical velocity. When flying without contact (no heater power, Fig 4.7a) the slider's vertical velocity is not excited at any specific frequency. Contact with only the mobile lubricant causes slider excitation at $129kHz$ (Fig 4.7b), presumed to be the first pitch mode. A significant change in the slider's vertical dynamics occurs when contact is established with the bonded lubricant (Fig 4.7c) with the slider's excitation shifting to $231kHz$, presumed to be another dominant vibration mode for this slider. The presence of the mobile lubricant does not have a significant influence on the slider's dynamics when contact is established with the bonded lubricant layer (Fig 4.7c,d).

Based on these results it is concluded that at the onset of lubricant contact, the slider is excited at the first pitch mode ($129kHz$). A stronger lubricant contact condition excites the slider at its dominant secondary mode ($231 - 233kHz$). These excitation frequencies are observed for this slider design in experiments conducted at differing disk rotation speeds implying that the slider responds at its natural modes, determined by the air-bearing and suspension stiffness, and not at any forced excitation frequencies within the system, such as those from disk waviness/roughness.

4.2.2 Contact loss above a critical power beyond the TDP

For this particular slider design, when the heater power is increased well beyond the TDP, the AE signal is suddenly suppressed (Fig 4.8c) indicating a possible loss of contact (or reduction in contact intensity) above a critical power. This phenomenon is repeatable for this slider design when experiments are performed over different media. It is speculated

that this condition corresponds to the case of lube-surfing, where only a part of the TFC protrusion is in contact with the lubricant, and the slider's dynamics as well as AE signal are damped out by the lubricant [Liu et al. 2008]. Another distinct possibility is that the air-bearing pressure due to TFC protrusion is altered in a way that makes it able to support the slider and it flies at a secondary stable fly-height without lubricant contact.

Analysis of the slider's vertical dynamics (Fig 4.8b) shows that the vertical velocity spectrum at higher heater power (Fig 4.8d) is similar to that for passive flying (Fig 4.7a), except for small changes around $270kHz$. In addition, OSA scans reveal that while there is a significant change in the lubricant profile when the maximum power is below the critical power (Fig 4.9a,b), the change is insignificant when the heater power is above the critical power (Fig 4.9c). The evidence from slider vertical dynamics combined with the lack of lubricant profile changes at higher heater power supports the argument that when the heater power is increased beyond a critical power, the slider's attitude may adjust so as to achieve a stable flying condition with no contact.

It is pointed out that such a loss of contact above a critical power is a slider design specific phenomenon. The 3σ of the AE signal and vertical velocity are plotted for a 'femto' slider design that shows no loss of contact when the heater power is increased to 30% above the TDP (Fig 4.10a). A similar plot for the 'pemto' slider considered in this work shows loss of contact above a critical power (Fig 4.10b). It is also noted that the slider's stability and HDI reliability for prolonged flying at high heater powers requires further investigation. Preliminary experiments show that when the slider is flown at higher heater power for 5 minutes, the high pressure under the TFC protrusion creates a lubricant depletion track superposed with lubricant rippling at the airbearing frequencies even when the AE signal remains suppressed (Fig 4.11c). Such a lubricant profile change under the TFC protrusion may excite slider dynamics and eventually lead to slider instability, contact and HDI failure [Dai et al. 2003, 2004b].

4.2.3 3D slider dynamics under lubricant contact

The three dimensional slider dynamics under lubricant contact are measured by conducting experiments on fully lubed disk. The 3σ of the vertical, down-track and off-track velocity signals for the first cycle of the sine waveform (Fig 4.3b) from experiments conducted at -15^o skew and a linear velocity of $14.6m/s$ are shown in Fig 4.12 together with the AE signal and power profile. The peak power of the sine waveform in these tests is TDP+$23mW$. These figures confirm the sudden increase in slider excitation during lubricant contact, and the sudden drop in slider velocity excitation in all three directions when the heater power is above a critical power.

The data in Fig 4.12 is presented as hysteresis plots for displacements, velocities and AE signal against power in Fig 4.13. Based on the AE signal data, it is seen that the power required for onset of slider-lubricant contact during the power-up phase (i.e. touchdown power TDP) is $2mW$ lower than the power at which slider-lubricant contact ceases in the power-down phase (i.e takeoff power TOP). Although not shown here, the TDP and TOP for the remaining three cycles of the sine power waveform are the same as the first, implying that slider or lubricant burnishing is not the cause for the difference in TDP and TOP, and it also requires further investigation. The repeatability of the hysteresis plots for the four

cycles adds confidence to the experimental method, in addition to verifying the robustness of the HDI to short duration slider-lubricant contact.

Interestingly, Fig 4.13 shows that while the slider's vertical and down-track velocity magnitudes change significantly during contact, the displacement magnitude (computed by integration of the velocity signal) does not show such a stark change. In contrast, however, the off-track displacements show the greatest increase during contact, even though it appears that the off-track velocity is not significantly affected. This behavior may be explained by understanding the dominant frequency content of these signals.

Fig 4.14 shows the spectrum of the vertical, down-track and off-track velocities for lubricant contact. Comparing the slider's vertical velocity spectrum Fig 4.14a to Fig 4.7, it is inferred that contact with the mobile lubricant occurs at TDP+3mW, contact with the mobile and bonded lubricant occurs at TDP+8mW. While excitation at the air bearing frequencies (129kHz, 234kHz) is seen in all three directions, suspension related frequencies ($< 50kHz$) are seen only in the off-track direction (Fig 4.14c,d). The contribution to displacement (computed by integrating velocities) is greater from excitation at the lower frequencies than it is from higher frequencies. Since off-track excitation has the lower frequency content from suspension modes, the off-track displacements are significantly larger than the vertical or down-track displacements during lubricant contact. This result reveals that slider-lubricant contact poses a serious challenge to servo track seek/follow operations.

At TDP+23mW, the heater power is beyond the critical power. It was argued earlier that the slider flies stably without contact at such high heater power. The lack of down-track excitation at high power (Fig 4.14b) supports this argument because contact events should result in friction forces that are aligned mainly in the down-track direction and thereby excite the slider down-track dynamics significantly.

While the slider may fly without contact at TDP+23mW, its dynamics is slightly different from the passive flying condition (no heater power) as reflected by the presence of vertical excitation at 270kHz (Fig 4.14a) and off-track excitation at 20kHz (Fig 4.14d).

4.3 Conclusion

Slider-lubricant contact is established by carefully controlling the TFC heater power and the three dimensional slider dynamics under lubricant contact is investigated. Lubricant contact excites the vertical, down-track and off-track dynamics with greatest displacement change occurring in the off-track direction (for nonzero skew experiments). The degree of slider-lubricant contact determines the slider's vibration modes. In general, vertical and down-track dynamics are excited at the air bearing frequencies while off-track excitation occurs at air bearing as well as suspension frequencies. For specific slider designs, there is a sudden drop in the AE signal and slider excitation when the heater power is increased above a critical power (beyond TDP). This phenomenon has been speculated elsewhere to be the lube-surfing regime, but the evidence in this work points to the contrary: the slider appears to attain a secondary (stable) flying state without any lubricant contact and requires further investigation. The lubricant surface nonuniformity/roughness may have a significant influence on the head-disk clearance and the slider's flying height similar in fashion to the slider-disk roughness. Deliberate 'patterning' of the lubricant is envisioned as a novel

technique to reduce the slider's fly-height and the head-disk clearance.

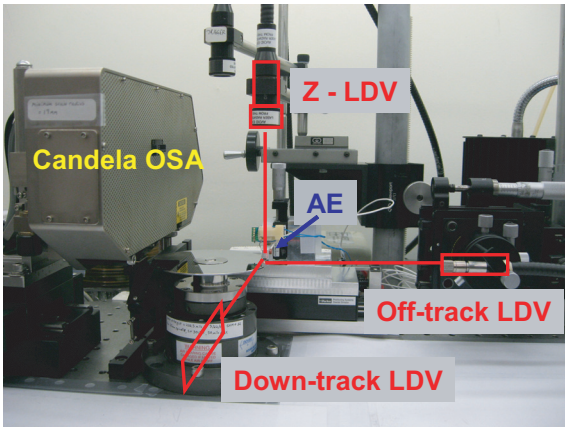

Figure 4.1: The spin stand experimental set-up

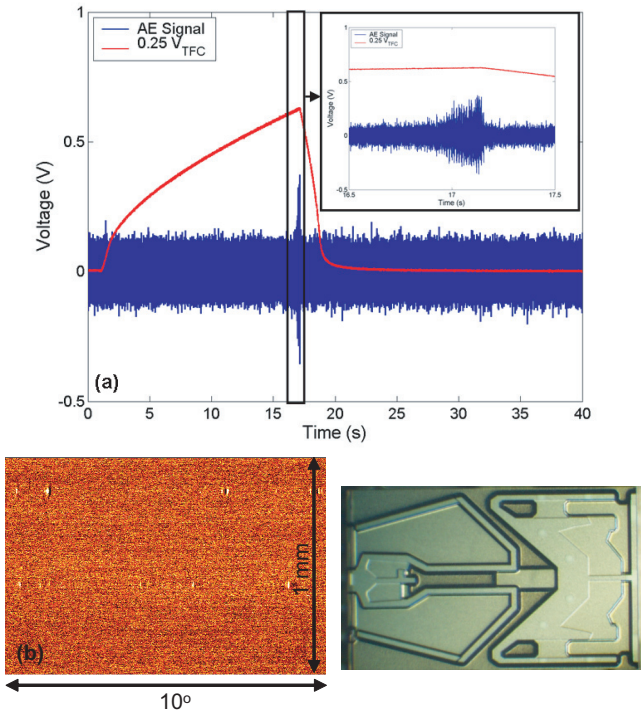

Figure 4.2: Touchdown detection test (a) AE signal (b) Lubricant profile change

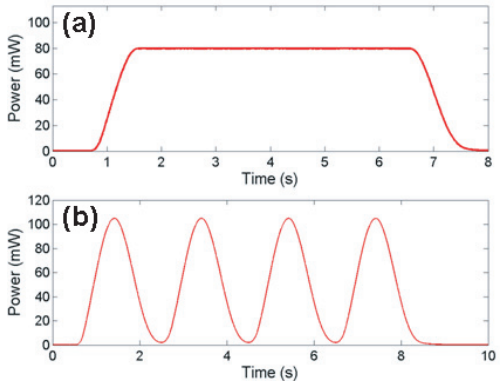

Figure 4.3: Power input profile for (a) establishing slider-lubricant contact (b) slider dynamics investigations

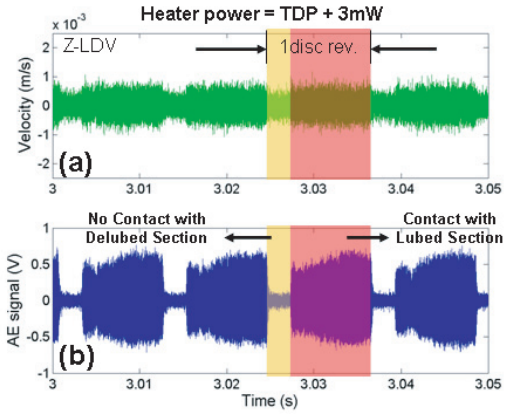

Figure 4.4: Contact with lubed section (a) Slider's vertical velocity (b) AE signal

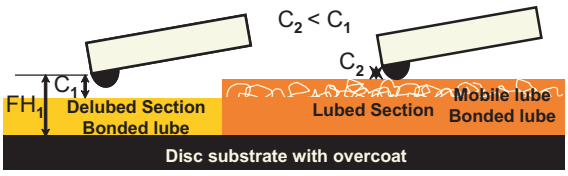

Figure 4.5: Schematic: Clearance loss in the lubed section

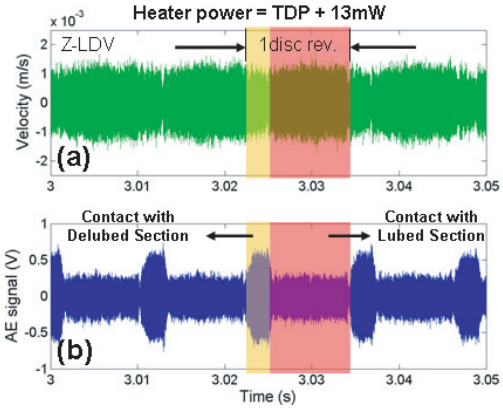

Figure 4.6: Contact with lubed and delubed sections (a) Slider's vertical velocity (b) AE signal

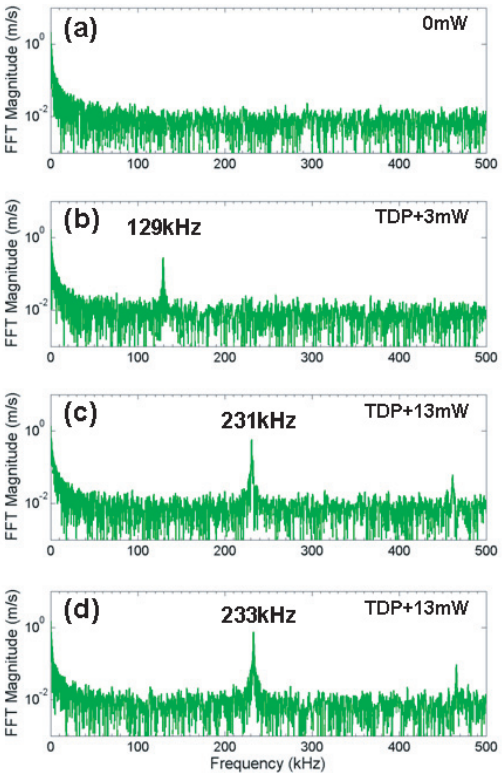

Figure 4.7: Spectrum of slider's vertical velocity (a) Passive flying (no heater power) (b) Contact with mobile lube (c) Contact with bonded lube (d) Contact with mobile and bonded lube

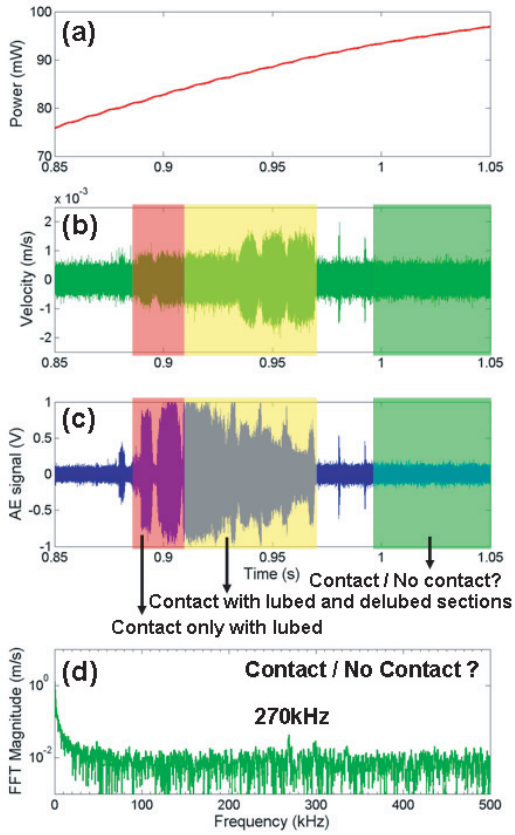

Figure 4.8: Possible contact loss at higher power (a) TFC heater power (b) Slider's vertical velocity (c) AE signal (d) Vertical velocity spectrum

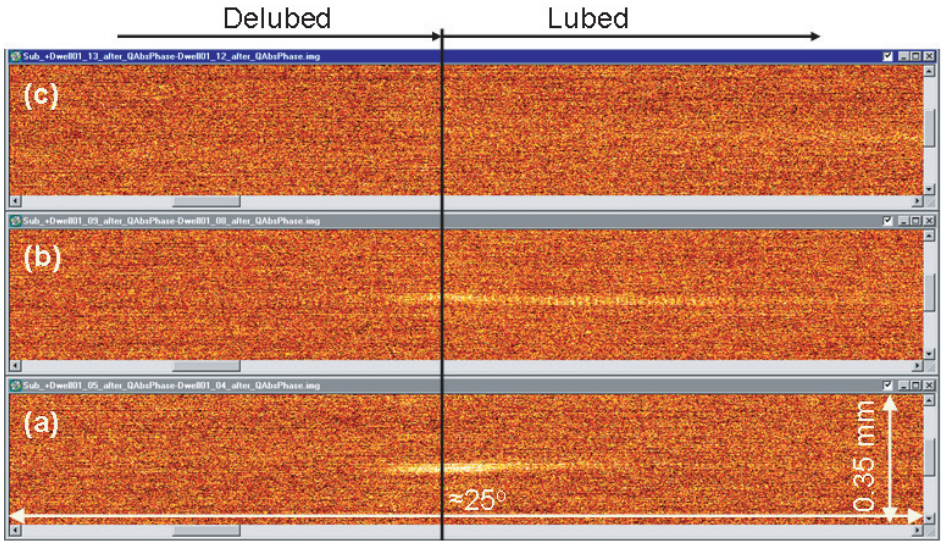

Figure 4.9: Lubricant profile change after $5s$ (partly delubed disk) (a) TDP+$3mW$ (b) TDP+$13mW$ (c) TDP+$23mW$

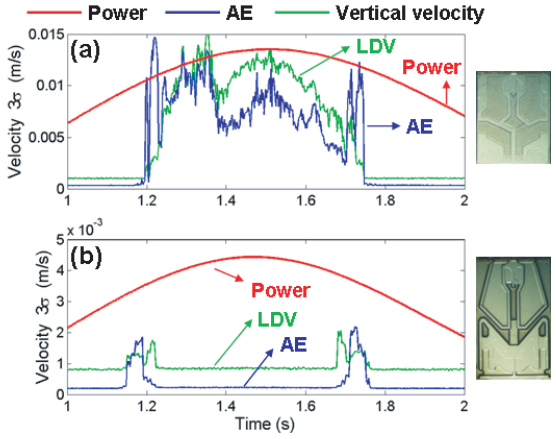

Figure 4.10: Response at high heater power (max power = 1.3TDP) is slider design dependent (a) No loss of contact (b) Loss of contact above a critical power

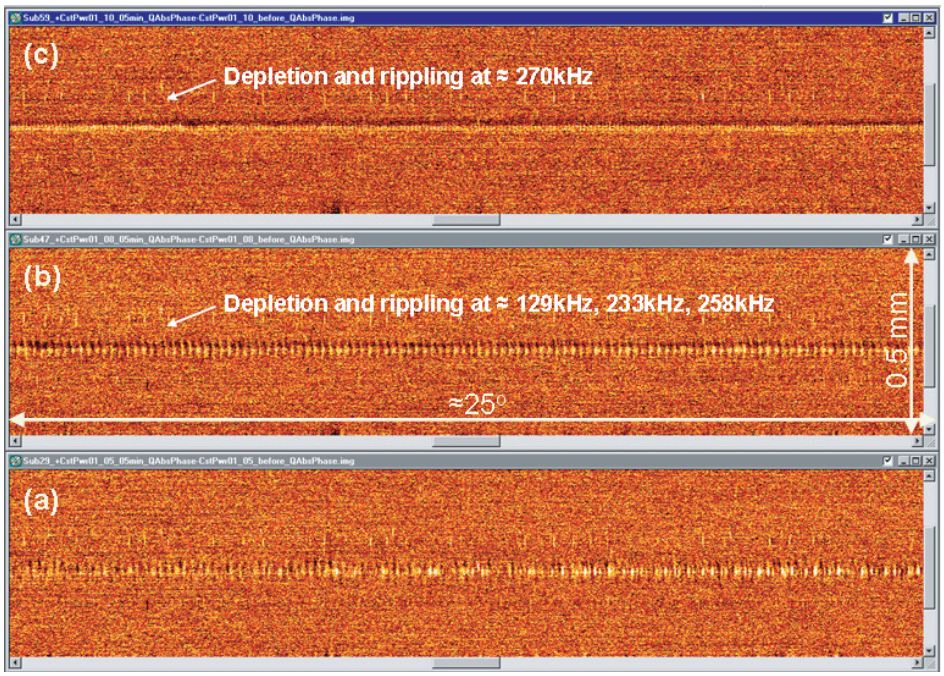

Figure 4.11: Lubricant profile change after $5min.$ (fully lubed disk) (a) TDP+$2mW$: contact with mobile lube (b) TDP+$13mW$: contact with mobile and bonded lube (c) TDP+$25mW$: above critical power with suppressed AE signal

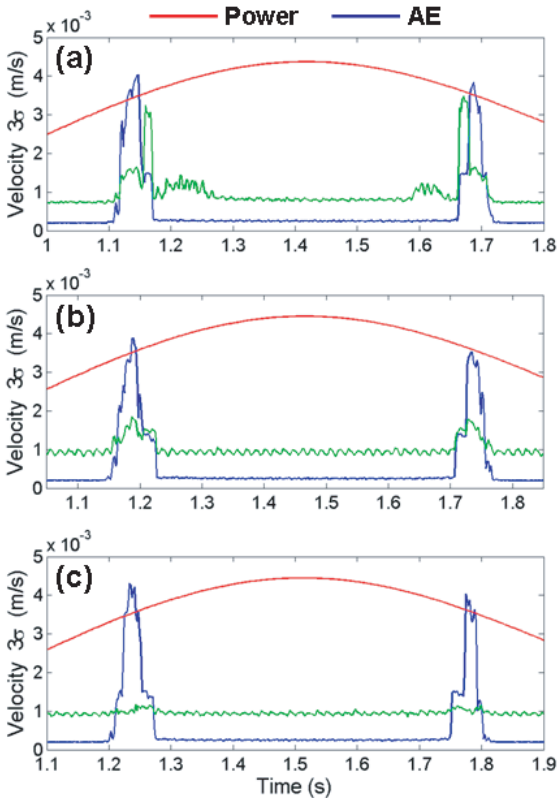

Figure 4.12: Time history of heater power, 3σ of AE signal and 3σ of velocity signal (a) Vertical (b) Down-track (c) Off-track

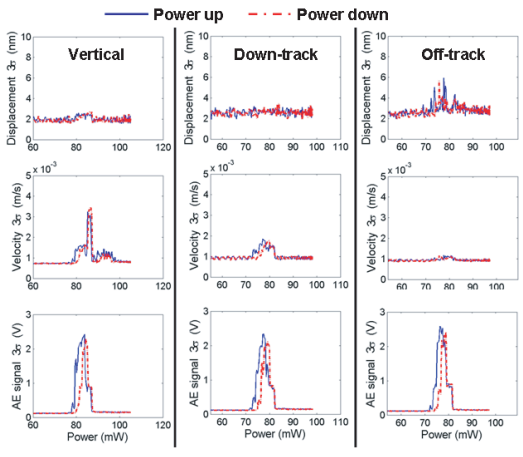

Figure 4.13: Hysteresis plots against power (maximum power is TDP+$23mW$). First row: displacement; second row: velocity; third row: AE signal

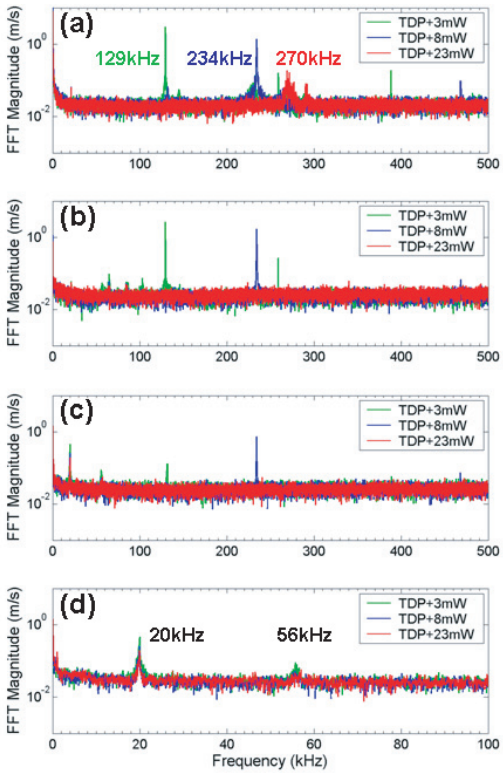

Figure 4.14: Frequency spectrum for transient tests at -15^o skew (a) Vertical (b) Down-track (c) Off-track (d) Off-track zoomed

Chapter 5

Thermal Fly-height Control Slider Instability and Dynamics at Touchdown: Explanations using Nonlinear Systems Theory

The dynamics of thermal fly-height control (TFC) sliders in contact with the lubricant are discussed in Chapter 4. Slider-lubricant contact at touchdown power (TDP) causes significant vibrations (instability) in the vertical, down-track and off-track directions. For particular slider designs, however, this vibration suddenly gets suppressed (stability) above a critical heater power beyond the TDP. While this stable condition is attributed to a lube-surfing regime [Liu et al. 2008], the physics behind this phenomena is not fully understood. Modeling efforts considering the static case show that stable flying-heights are possible under lubricant contact due to the nonlinearity of the external forces (the net effect of air bearing pressure, adhesion, contact, etc.) [Yu et al. 2009, Zheng and Bogy 2010] but these results do not readily extend to the dynamic case where the external forces also vary with time. Numerical simulations for the dynamic case can predict the slider's motion for particular sets of head-disk interface (HDI) parameters, initial conditions and a chosen nonlinear model [Liu et al. 2009, Vakis et al. 2009], but they are inadequate for explaining the origin and physics of the problem.

This chapter presents continued investigations on the topic of slider instability and dynamics at touchdown/contact through experiments and analytical modeling. Experiments reveal that the frequency spectrum of slider vibrations at touchdown consists of peaks at the first pitch mode, its harmonics, and additionally, several peaks at frequencies lower and higher than the first pitch mode. A simple analytical model which accounts for thermal protrusion and the special dynamic case of periodic external forcing is used to predict and offer explanations for slider instability and response observed in the experiments. The slider is represented by a two-degree of freedom model (accounting for the vertical and pitch motions), and the load carrying air-bearing surface (ABS) is represented by two springs, one each for the leading and trailing ends. The thermal protrusion is modeled as a relative change in the nonlinear stiffness of the trailing end spring, compared to the linear stiffness of the leading end spring. The coupled nonlinear equations for slider motion are derived and

studied analytically using nonlinear systems theory.

Thermal protrusion continuously changes the system's natural frequencies through the change in the trailing end stiffness (section 3.2.3), and interesting slider dynamics occur for particular protrusion ranges. Nonlinear systems theory is used to highlight slider instabilities arising from an unfavorable coupling of system vibration modes through an internal resonance condition, as well as the favorable suppression of instabilities through a jump condition. Excitation frequencies that may lead to large amplitude slider vibrations and the dominant frequencies at which the slider's response occurs are also predicted from theory, and they correspond to the primary and combination resonance conditions resulting in *subharmonics*, *superharmonics* and *fractional harmonics* of the nonlinear system. Using parameters representative of the slider used in experiments, the theoretically predicted frequencies are shown to be in excellent agreement with experimental results. This analytical study highlights some important ABS design considerations that can help prevent slider instability as well as help mitigate unwanted slider vibrations thereby ensuring the reliability of the HDI at extremely low head-disk clearances.

5.1 Experiments

Experiments are performed with 'pemto' TFC sliders ($1.25mm \times 0.85mm$) on a $95mm$ media coated with perfluoropolyether (PFPE) lubricant. The spin stand is instrumented with a laser doppler vibrometer (LDV) to measure the slider's vertical vibration, an acoustic emission (AE) sensor to monitor contact at the HDI and an *in-situ* optical surface analyzer (OSA) to investigate changes in the lubricant surface (Fig 5.1). A custom written Labview code together with a data acquisition board and amplifier circuit is used to input pre-programmed power profiles to the TFC heater with submilliwatt resolution. The test procedure is as follows: The slider is loaded onto the rotating disk and moved to the desired track. The TDP is measured using the automated Labview program which uses the AE signal as feedback and records the power at which there is a sudden change in the AE signal as the TDP [Vangipuram Canchi and Bogy 2010]. Once the TDP is determined, the transient slider dynamics under contact are investigated by supplying a power profile that consists of four sinusoidal waves having a $1s$ time period [Vangipuram Canchi and Bogy 2010]. The peak power of this waveform is TDP+$20mW$ in these investigations. All tests are conducted at 0^o skew and at the slider's design linear velocity of $22m/s$.

The time history of the slider's vertical velocity, AE signal and supplied heater power are shown in Fig 5.2 for the first cycle of the sinusoidal power waveform. For this particular ABS design (shown in Fig 5.2), peculiar dynamics are observed during the transient test. The slider shows significant vibrations (denoted as the 'unstable' region) when the heater power is increased slightly above the TDP. However, when the heater power is increased above a critical power beyond the TDP, the slider's vibrations as well as the AE signal are suddenly suppressed (denoted as the 'stable' region). Previous researchers have speculated that this condition of suppressed vibrations corresponds to a case of lube-surfing, where a small portion of the thermal protrusion is in continuous contact with the lubricant [Liu et al. 2008, 2009]. However, as reported previously, evidence from *in-situ* lubricant scans support the distinct possibility of the slider flying at a secondary stable flying-height without lubricant-contact

at higher heater powers [Vangipuram Canchi and Bogy 2010]. Further investigations are ongoing to fully understand the physics of this phenomenon.

The current experiments also reveal that the frequency spectrum of slider vibrations at TDP (unstable region) consists of peaks at the first pitch mode ($128kHz$), its harmonics, and additionally, several peaks at frequencies lower and higher than the first pitch mode (Fig 5.3). The appearance of multiple peaks in the frequency spectrum highlights the effect of nonlinearities, and similar results have been reported for traditional (non-TFC) sliders in proximity from experiments and simulation [Thornton and Bogy 2003a]. Motivated by this observation, the slider air bearing nonlinear system is analytically investigated with a focus on understanding whether it is possible for the slider to have 'unstable' dynamics for certain range(s) of heater power (i.e. thermal protrusion), whether slider dynamics could be rendered 'stable' because of interacting nonlinearities, and whether the experimentally observed peaks in the frequency spectrum of slider vibrations are explained by theory.

5.2 Analytical Model

The slider is modeled as a rigid body with only two degrees of freedom, corresponding to the pitch and vertical motion. The air bearing is represented by springs and dampers, one each for the trailing and leading ends (Fig 5.4). The spring at the trailing end is assumed to be nonlinear (with quadratic and cubic force terms) accounting for air bearing stiffness changes due to spacing changes from the slider's vibrations as well as other nonlinearities at the HDI, such as those arising from electrostatic forces, intermolecular forces and slider contact with the lubricant or disk, to mention a few. Since the focus of this work remains on understanding the effect of nonlinearities on slider dynamics and stability, it is not of concern as to where these nonlinearities arise, but only that they are represented by quadratic and cubic terms as an approximation, thus keeping the math tractable. Thermal protrusion is modeled as an increase in the stiffness of the spring at the trailing end compared to the fixed stiffness of the spring at the leading end (through a multiplicative factor α) as explained in section 5.2.1.

5.2.1 Equations of motion

The equations of motion for the system (Fig 5.4) are easily derived using Lagrange's equations or other techniques. Assuming the leading and trailing end spring stiffnesses to have the form

$$\begin{aligned} k_1 &= k_{11} - k_{12}z + k_{13}z^2 \\ k_2 &= k_{21} \end{aligned} \tag{5.1}$$

the nondimensional equations of motion are

$$\begin{aligned} \ddot{\zeta} = F_1 &- \zeta - \Lambda_1 \sin\theta - \delta_1\dot{\zeta} - \delta_2\dot{\theta}\cos\theta \\ &+ \Lambda_4\zeta^2 - \Lambda_5\zeta^3 + \Lambda_6\zeta\sin\theta - \Lambda_7\zeta^2\sin\theta \end{aligned} \tag{5.2a}$$

$$\begin{aligned} \Lambda_3\ddot{\theta} = F_2 &- \Lambda_1\zeta\cos\theta - \Lambda_2\sin\theta\cos\theta - \delta_2\dot{\zeta}\cos\theta - \delta_3\dot{\theta}\cos^2\theta \\ &+ \Lambda_6\zeta^2\cos\theta - \Lambda_7\zeta^3\cos\theta + \Lambda_8\zeta\sin\theta\cos\theta - \Lambda_9\zeta^2\sin\theta\cos\theta \end{aligned} \tag{5.2b}$$

where the dot implies derivatives with respect to the nondimensional time τ, ζ is the nondimensional displacement in the vertical direction, θ is the pitch angle, and the other quantities are related to the system parameters by

$$\begin{aligned}
\tau &= \omega t & \zeta &= \frac{z}{L} & \omega^2 &= \frac{k_{11}+k_{21}}{m} \\
\Lambda_1 &= \frac{k_{11}L_1 - k_{21}L_2}{mL\omega^2} & \Lambda_2 &= \frac{k_{11}L_1^2 + k_{21}L_2^2}{mL^2\omega^2} & \Lambda_3 &= \frac{I}{mL^2} \\
\Lambda_4 &= \frac{k_{12}}{m\omega^2} & \Lambda_5 &= \frac{k_{13}L^2}{m\omega^2} & \Lambda_6 &= \frac{k_{12}L_1}{m\omega^2} \\
\Lambda_7 &= \frac{k_{13}L_1L}{m\omega^2} & \Lambda_8 &= \frac{k_{12}L_1^2}{m\omega^2} & \Lambda_9 &= \frac{k_{13}L_1^2}{m\omega^2} \\
\delta_1 &= \frac{b_1+b_2}{m\omega} & \delta_2 &= \frac{b_1L_1 - b_2L_2}{mL\omega} & \delta_3 &= \frac{b_1L_1^2 + b_2L_2^2}{mL^2\omega} \\
F_1 &= \frac{F}{mL\omega^2} & F_2 &= \frac{M}{mL^2\omega^2} &&
\end{aligned} \tag{5.3}$$

where m and I represent the slider's mass and moment of inertia, respectively, F and M represent the force and moment about the slider's center of mass G, respectively, and L is an arbitrary length scale (chosen to be $1nm$ unless mentioned otherwise). Note that the model is set-up such that $(\zeta, \theta) = (0, 0)$ is the equilibrium state. (In reality, the slider has a non-zero pitch at equilibrium, but it can be neglected in this work for convenience and to keep the math tractable).

Since the range of pitch motion during slider vibration is very small (a few *microradians*), the approximations $\sin\theta \approx \theta$ and $\cos\theta \approx 1$ are valid, and the equations of motion (5.2) may be written in matrix form after making these approximations as

$$\mathbf{M}\ddot{\mathbf{x}} + \mathbf{C}\dot{\mathbf{x}} + \mathbf{K}\mathbf{x} + \mathbf{h}(\mathbf{x}) = \mathbf{F} \tag{5.4}$$

$$\begin{aligned}
\mathbf{M} &= \begin{pmatrix} 1 & 0 \\ 0 & \Lambda_3 \end{pmatrix} & \mathbf{C} &= \begin{pmatrix} \delta_1 & \delta_2 \\ \delta_2 & \delta_3 \end{pmatrix} & \mathbf{K} &= \begin{pmatrix} 1 & \Lambda_1 \\ \Lambda_1 & \Lambda_2 \end{pmatrix} \\
\mathbf{x} &= \begin{pmatrix} \zeta \\ \theta \end{pmatrix} & \mathbf{h}(\mathbf{x}) &= \begin{pmatrix} h_1(\zeta,\theta) \\ h_2(\zeta,\theta) \end{pmatrix} & \mathbf{F} &= \begin{pmatrix} F_1 \\ F_2 \end{pmatrix}
\end{aligned}$$

$$\begin{aligned}
h_1(\zeta,\theta) &= -\Lambda_4\zeta^2 - \Lambda_6\zeta\theta + \Lambda_5\zeta^3 + \Lambda_7\zeta^2\theta \\
h_2(\zeta,\theta) &= -\Lambda_6\zeta^2 - \Lambda_8\zeta\theta + \Lambda_7\zeta^3 + \Lambda_9\zeta^2\theta
\end{aligned}$$

The nonlinearities of the quadratic and cubic forms are evident and contained in $\mathbf{h}(\mathbf{x})$. (Note: The higher order approximation $\sin\theta \approx \theta - \frac{\theta^3}{6}$, $\cos\theta = 1 - \frac{\theta^2}{2}$ may also be used, and in that case, additional nonlinear (cubic) terms of the form $\zeta\theta^2$ and θ^3 would appear in the expression for $\mathbf{h}(\mathbf{x})$. However, the magnitudes of these newly introduced (cubic) nonlinearities are much smaller than those arising from the nonlinear spring stiffness and hence they can be neglected).

Considering only the linear part of (5.4), the natural frequencies ω_1 and ω_2 (also called the linear natural frequencies, where $\omega_1 < \omega_2$) and mode shapes are easily computed for

a chosen set of system parameters through an eigenvalue analysis. The slider air bearing system has two modes: the air bearing first pitch mode corresponding to ω_1 is the rotation of the slider about a point close to the trailing end, while the air bearing second pitch mode corresponding to ω_2 is the rotation of the slider about a point closer to the leading end (Fig 5.5a).

In this work, the system parameters are chosen to match the slider used in the experiment. The slider's mass and moment of inertia are readily calculated from the slider's dimensions and material density (Table 5.1) and the spring stiffness values are chosen so that the first pitch mode frequency matches the experimentally observed value of $128kHz$ for this slider. Accordingly, the stiffness value $k_{21} = 3.3 \times 10^5 N/m$ is used, while the stiffness value k_{11}, which depends on the thermal protrusion is given by $k_{11} = \alpha k_{21}$ where $\alpha(> 1)$ increases with increasing protrusion.

The effect of thermal protrusion on the linear natural frequencies (ω_1, ω_2) is shown in Fig 5.5b. It is evident that increasing α (i.e. the thermal protrusion) does not change the first pitch mode frequency ω_1 significantly. However, the second pitch mode frequency ω_2 increases monotonically with α. It is verified that the mode shapes (Fig 5.5a) are not significantly altered by a change in α. This result essentially emulates the simulation results presented in section 3.2.3 using the full ABS model and CMLAir PIP software.

It is well known from nonlinear systems theory that when the linear natural frequencies of a two degree of freedom nonlinear system are commensurable or nearly commensurable, a strong coupling of the (otherwise decoupled) modes can occur, and this condition is called an internal resonance [Nayfeh and Mook 1979]. The occurrence of an internal resonance depends strongly on the system parameters, and the commensurability conditions for a two degree of freedom system are given by $\omega_2 \approx 2\omega_1$ when quadratic nonlinearities are present, and $\omega_2 \approx 3\omega_1$ when cubic nonlinearities are present.

Considering the slider air bearing system, based on the preceding calculations for ω_1 and ω_2 as a function of α, it is possible that for particular slider designs that have $\omega_1 < \omega_2 < 2\omega_1$ with no thermal protrusion (i.e. zero heater power), the thermal protrusion induced by increasing heater power can cause ω_2 to increase through an internal resonance condition ($\omega_2 \approx 2\omega_1$ or $\omega_2 \approx 3\omega_1$). For example, Fig 5.5b shows that $\omega_2 \approx 2\omega_1$ when $\alpha \approx 2.075$ and $\omega_2 \approx 3\omega_1$ when $\alpha \approx 5$ for the system parameters shown in Table 5.1. An internal resonance could result in large amplitude response depending on the system parameters. Therefore, for particular ranges of heater power, when an internal resonance condition occurs, large amplitude slider vibrations are possible, and they can lead to slider-lubricant/disk contact, or enhance the degree of existing slider-lubricant/disk contact.

The nonlinear equations (5.4) for the slider air bearing system are investigated for internal resonance and large amplitude response. This paper presents results only for the internal resonance condition $\omega_2 \approx 2\omega_1$ arising from quadratic nonlinearities. The analysis when $\omega_2 \approx 3\omega_1$ may be treated in a similar fashion [Nayfeh and Mook 1979].

5.2.2 Analysis of the nonlinear equations

The equations of motion are transformed and written in terms of the modal coordinates η and ϕ as

$$\ddot{\eta} + \omega_1^2\eta = -2\hat{\mu}_1\dot{\eta} + A_1\eta^2 + A_2\eta\phi + A_3\phi^2 + B_1\eta^3 + B_2\eta^2\phi + B_3\eta\phi^2 + B_4\phi^3 + \hat{F}_1 \tag{5.5a}$$

$$\ddot{\phi} + \omega_2^2\phi = -2\hat{\mu}_2\dot{\phi} + A_4\eta^2 + A_5\eta\phi + A_6\phi^2 + B_5\eta^3 + B_6\eta^2\phi + B_7\eta\phi^2 + B_8\phi^3 + \hat{F}_2 \tag{5.5b}$$

$$\begin{aligned}
A_1 &= \gamma_1(\Lambda_4\gamma_1^2 + \Lambda_6\gamma_1\gamma_3) + \gamma_3(\Lambda_6\gamma_1^2 + \Lambda_8\gamma_1\gamma_3)\\
A_2 &= \gamma_1(\Lambda_4 2\gamma_1\gamma_2 + \Lambda_6(\gamma_1\gamma_4 + \gamma_2\gamma_3)) + \gamma_3(\Lambda_6 2\gamma_1\gamma_2 + \Lambda_8(\gamma_1\gamma_4 + \gamma_2\gamma_3))\\
A_3 &= \gamma_1(\Lambda_4\gamma_2^2 + \Lambda_6\gamma_2\gamma_4) + \gamma_3(\Lambda_6\gamma_2^2 + \Lambda_8\gamma_2\gamma_4)\\
A_4 &= \gamma_2(\Lambda_4\gamma_1^2 + \Lambda_6\gamma_1\gamma_3) + \gamma_4(\Lambda_6\gamma_1^2 + \Lambda_8\gamma_1\gamma_3)\\
A_5 &= \gamma_2(\Lambda_4 2\gamma_1\gamma_2 + \Lambda_6(\gamma_1\gamma_4 + \gamma_2\gamma_3)) + \gamma_4(\Lambda_6 2\gamma_1\gamma_2 + \Lambda_8(\gamma_1\gamma_4 + \gamma_2\gamma_3))\\
A_6 &= \gamma_2(\Lambda_4\gamma_2^2 + \Lambda_6\gamma_2\gamma_4) + \gamma_4(\Lambda_6\gamma_2^2 + \Lambda_8\gamma_2\gamma_4)
\end{aligned} \tag{5.6}$$

$$\begin{aligned}
B_1 &= -\gamma_1(\Lambda_5\gamma_1^3 + \Lambda_7\gamma_1^2\gamma_3) - \gamma_3(\Lambda_7\gamma_1^3 + \Lambda_9\gamma_1^2\gamma_3)\\
B_2 &= -\gamma_1(\Lambda_5 3\gamma_1^2\gamma_2 + \Lambda_7(2\gamma_1\gamma_2\gamma_3 + \gamma_1^2\gamma_4)) - \gamma_3(\Lambda_7 3\gamma_1^2\gamma_2 + \Lambda_9(2\gamma_1\gamma_2\gamma_3 + \gamma_1^2\gamma_4))\\
B_3 &= -\gamma_1(\Lambda_5 3\gamma_1\gamma_2^2 + \Lambda_7(2\gamma_1\gamma_2\gamma_4 + \gamma_2^2\gamma_3)) - \gamma_3(\Lambda_7 3\gamma_1\gamma_2^2 + \Lambda_9(2\gamma_1\gamma_2\gamma_4 + \gamma_2^2\gamma_3))\\
B_4 &= -\gamma_1(\Lambda_5\gamma_2^3 + \Lambda_7\gamma_2^2\gamma_4) - \gamma_3(\Lambda_7\gamma_2^3 + \Lambda_9\gamma_2^2\gamma_4)\\
B_5 &= -\gamma_2(\Lambda_5\gamma_1^3 + \Lambda_7\gamma_1^2\gamma_3) - \gamma_4(\Lambda_7\gamma_1^3 + \Lambda_9\gamma_1^2\gamma_3)\\
B_6 &= -\gamma_2(\Lambda_5 3\gamma_1^2\gamma_2 + \Lambda_7(2\gamma_1\gamma_2\gamma_3 + \gamma_1^2\gamma_4)) - \gamma_4(\Lambda_7 3\gamma_1^2\gamma_2 + \Lambda_9(2\gamma_1\gamma_2\gamma_3 + \gamma_1^2\gamma_4))\\
B_7 &= -\gamma_2(\Lambda_5 3\gamma_1\gamma_2^2 + \Lambda_7(2\gamma_1\gamma_2\gamma_4 + \gamma_2^2\gamma_3)) - \gamma_4(\Lambda_7 3\gamma_1\gamma_2^2 + \Lambda_9(2\gamma_1\gamma_2\gamma_4 + \gamma_2^2\gamma_3))\\
B_8 &= -\gamma_2(\Lambda_5\gamma_2^3 + \Lambda_7\gamma_2^2\gamma_4) - \gamma_4(\Lambda_7\gamma_2^3 + \Lambda_9\gamma_2^2\gamma_4)
\end{aligned} \tag{5.7}$$

where ω_1 and ω_2 are the linear natural frequencies, $\hat{\mu}_1$ and $\hat{\mu}_2$ represent the modal damping values (the damping matrix $\mathbf{C}$ is diagonalized by the modal matrix $\mathbf{V}$ by an assumption of Raleigh damping), and $\mathbf{V}$ is given by

$$\mathbf{V} = \begin{pmatrix}\gamma_1 & \gamma_2\\ \gamma_3 & \gamma_4\end{pmatrix}; \qquad \begin{pmatrix}\zeta\\ \theta\end{pmatrix} = \mathbf{V}\begin{pmatrix}\eta\\ \phi\end{pmatrix}; \qquad \begin{pmatrix}\hat{F}_1\\ \hat{F}_2\end{pmatrix} = \mathbf{V}^T\begin{pmatrix}F_1\\ F_2\end{pmatrix} \tag{5.8}$$

The coupled equations (5.5) are in their simplest form accounting for the most general case of quadratic and cubic nonlinearities.

Considering the forcing term to be sinusoidal in nature, the nonlinear coupled equations (5.5) are analyzed using the method of multiple scales closely following the methods outlined in [Nayfeh and Mook 1979]. The first order uniform solution of the form

$$\eta = \epsilon\eta_1 + \epsilon^3\eta_3 \tag{5.9a}$$

$$\phi = \epsilon\phi_1 + \epsilon^3\phi_3 \tag{5.9b}$$

is sought, where ϵ is a small parameter. Defining the different time scales $T_0 = \tau$, $T_2 = \epsilon^2\tau$, and $D_k = \frac{d}{dT_k}$ for $k = 0, 2, \ldots$ the time derivative is represented by

$$\frac{d}{d\tau} = D = D_0 + \epsilon^2 D_2 + \ldots \tag{5.10a}$$

$$\frac{d^2}{d\tau^2} = D^2 = D_0^2 + \epsilon^2 2D_0D_2 + \ldots \tag{5.10b}$$

In the following analysis, two cases require slightly different consideration: the primary resonance case, when the frequency of the forcing term (Ω) is close to one of the system linear natural frequencies ω_1 or ω_2, and the secondary resonance (or nonresonant) case, when Ω is far away from ω_1 or ω_2.

The analysis presented for the primary resonance and the secondary resonance cases cover the most general external forcing experienced by the slider. Periodic lubricant rippling has a significant affect on slider dynamics at low spacing and in light contact conditions [Dai et al. 2004a]. Slider response to such a periodic single frequency external force is covered by the primary resonance analysis. Slider-media contact results in a more complex forcing which may be written, in general, as a Fourier series sum consisting of many frequency components and the slider's response to such an excitation is covered by the secondary resonance analysis.

Primary resonance ($\Omega \approx \omega_1$)

The primary resonance condition considered in this work corresponds to $\Omega \approx \omega_1$, such as that occurring when the lubricant is rippled at the first pitch mode and feeds into system excitation and resonance [Dai et al. 2004a]. Strictly speaking, the forcing term is also dependent on the system state variables $(\zeta, \theta, \dot{\zeta}, \dot{\theta})$, however, the analysis is simplified by assuming that the forcing term is independent of state variables and dependent exclusively on time.

The scaling of quantities is to be chosen such that the forcing term, the nonlinearities and the damping interact at the same order. In the problem of slider vibration with small amplitudes (onset of instability), the damping and quadratic terms are of comparable order, while the cubic terms are of higher order. However, when the vibration amplitudes grow to become sufficiently large, the cubic terms can have the same order as the quadratic and damping terms. In order to simplify the analysis, it is assumed that quadratic as well as cubic nonlinearities are of the same order, corresponding to the case of large amplitude slider vibrations. The solution for the case, where cubic terms are absent, is easily found by setting the coefficients corresponding to the cubic terms to zero. Accordingly, the ordering of quantities is given by

$$\hat{\mu}_i = \epsilon^2 \mu_i \qquad A_j = \epsilon \alpha_j \qquad B_k = \beta_k \qquad \hat{F}_i = \epsilon^3 f_i \cos(\Omega\tau + \tau_i)$$
$$i = 1, 2 \; ; \quad j = 1, 2 \ldots, 6 \; ; \quad k = 1, 2, \ldots, 8 \tag{5.11}$$

Substituting (5.9), (5.10), (5.11) into (5.5), and collecting terms of order ϵ and order ϵ^3 gives

$$D_0^2 \eta_1 + \omega_1^2 \eta_1 = 0 \tag{5.12a}$$
$$D_0^2 \phi_1 + \omega_2^2 \phi_1 = 0 \tag{5.12b}$$

$$\begin{aligned} D_0^2 \eta_3 + \omega_1^2 \eta_3 = & -2D_0 D_2 \eta_1 - 2\mu_1 D_0 \eta_1 + \alpha_1 \eta_1^2 + \alpha_2 \eta_1 \phi_1 + \alpha_3 \phi_1^2 \\ & + \beta_1 \eta_1^3 + \beta_2 \eta_1^2 \phi_1 + \beta_3 \eta_1 \phi_1^2 + \beta_4 \phi_1^3 + f_1 cos(\Omega T_0 + \tau_1) \end{aligned} \tag{5.13a}$$

$$\begin{aligned} D_0^2 \phi_3 + \omega_2^2 \phi_3 = & -2D_0 D_2 \phi_1 - 2\mu_2 D_0 \phi_1 + \alpha_4 \eta_1^2 + \alpha_5 \eta_1 \phi_1 + \alpha_6 \phi_1^2 \\ & + \beta_5 \eta_1^3 + \beta_6 \eta_1^2 \phi_1 + \beta_7 \eta_1 \phi_1^2 + \beta_8 \phi_1^3 + f_2 cos(\Omega T_0 + \tau_2) \end{aligned} \tag{5.13b}$$

The solution to (5.12) is given by

$$\eta_1 = P(T_2)e^{i\omega_1 T_0} + cc \tag{5.14a}$$
$$\phi_1 = Q(T_2)e^{i\omega_2 T_0} + cc \tag{5.14b}$$

where P and Q are complex quantities, and cc denotes complex conjugate of all preceding terms. Substitution of (5.14) into (5.13) gives secular terms in the RHS of (5.13). Particularly, in the presence of an internal resonance condition arising from quadratic nonlinearities ($\omega_2 \approx 2\omega_1$) and primary resonance ($\Omega \approx \omega_1$), the secular terms are collected and set to zero to obtain the solvability conditions

$$2i\omega_1(D_2P + \mu_1 P) = \alpha_2 \bar{P}Qe^{i\sigma_1 T_0} + 3\beta_1 P^2\bar{P} + 2\beta_3 PQ\bar{Q} + \frac{1}{2}f_1 e^{i(\sigma_2 T_2 + \tau_1)} \tag{5.15a}$$
$$2i\omega_2(D_2Q + \mu_2 Q) = \alpha_4 P^2 e^{-i\sigma_1 T_0} + 3\beta_8 Q^2\bar{Q} + 2\beta_6 P\bar{P}Q \tag{5.15b}$$

where the overbar denotes the complex conjugate, and σ_1 and σ_2 are detuning parameters, (measures of the closeness to the internal resonance condition and the primary resonance condition, respectively), given by

$$\omega_2 = 2\omega_1 + \epsilon^2\sigma_1 \tag{5.16a}$$
$$\Omega = \omega_1 + \epsilon^2\sigma_2 \tag{5.16b}$$

Assuming P and Q to be of the form

$$P = \frac{1}{2}r_1(T_2)e^{i\psi_1(T_2)} \qquad Q = \frac{1}{2}r_2(T_2)e^{i\psi_2(T_2)} \tag{5.17}$$

where $r_i,\ \psi_i,\ (i = 1, 2)$ are real quantities that are functions of T_2, substituting (5.17) into (5.15), and separating the real and imaginary parts of the resulting equations give the differential equations for the evolution of $r_i,\ \psi_i,\ (i = 1, 2)$ as

$$4\omega_1(r_1' + \mu_1 r_1) - \alpha_2 r_1 r_2 \sin\nu_1 - 2f_1 \sin\nu_2 = 0 \tag{5.18a}$$
$$4\omega_2(r_2' + \mu_2 r_2) + \alpha_4 r_1^2 \sin\nu_1 = 0 \tag{5.18b}$$
$$8\omega_1 r_1\psi_1' + 3\beta_1 r_1^3 + 2\beta_3 r_1 r_2^2 + 2\alpha_2 r_1 r_2 \cos\nu_1 + 4f_1 \cos\nu_2 = 0 \tag{5.18c}$$
$$8\omega_2 r_2\psi_2' + 3\beta_8 r_2^3 + 2\beta_6 r_1^2 r_2 + 2\alpha_4 r_1^2 \cos\nu_1 = 0 \tag{5.18d}$$

where prime denotes differentiation with respect to T_2, and

$$\nu_1 = \sigma_1 T_2 + \psi_2 - 2\psi_1$$
$$\nu_2 = \sigma_2 T_2 + \tau_1 - \psi_1$$

The final solution (the time history of the modal coordinates) is given by

$$\eta(\tau) = \epsilon r_1(\epsilon^2\tau)\cos(\Omega\tau + \tau_1 - \nu_2) \tag{5.19a}$$
$$\phi(\tau) = \epsilon r_2(\epsilon^2\tau)\cos(2\Omega\tau + 2\tau_1 - 2\nu_2 + \nu_1) \tag{5.19b}$$

and may be written in terms of the original variables ζ and θ using (5.8).

The steady state amplitudes of oscillations are obtained by setting $r_i' = \nu_i' = 0$ $(i = 1, 2)$ in (5.18) which reduce to

$$4\omega_1\mu_1 r_1 - \alpha_2 r_1 r_2 \sin\nu_1 - 2f_1 \sin\nu_2 = 0 \tag{5.20a}$$
$$4\omega_2\mu_2 r_2 + \alpha_4 r_1^2 \sin\nu_1 = 0 \tag{5.20b}$$
$$8\omega_1\sigma_2 + 3\beta_1 r_1^3 + 2\beta_3 r_1 r_2^2 + 2\alpha_2 r_1 r_2 \cos\nu_1 + 4f_1 \cos\nu_2 = 0 \tag{5.20c}$$
$$8\omega_2(2\sigma_2 - \sigma_1) + 3\beta_8 r_2^3 + 2\beta_6 r_1^2 r_2 + 2\alpha_4 r_1^2 \cos\nu_1 = 0 \tag{5.20d}$$

The coupled nonlinear equations (5.20) may be solved to obtain the frequency response plot, which shows the steady state modal amplitudes r_1^{ss} and r_2^{ss} as functions of the detuning σ_2 (i.e. the forcing frequency Ω) as well as plots to understand the effect of the detuning σ_1 (which depends on the thermal protrusion 'α') on the steady state amplitude. The solutions of (5.20) are obtained numerically and presented in section 5.3.

Secondary resonance

For the nonresonant case (Ω far away from ω_1 or ω_2) the ordering is to be chosen so that the forcing term appears at order ϵ, while the damping and nonlinearities appear at order ϵ^3. In addition, to include the case of combination resonances, which occur when the forcing consists of a multifrequency excitation, a two frequency excitation occurring at Ω_1 and Ω_2 $(\Omega_1 < \Omega_2)$ is considered. Accordingly, the ordering of quantities is given by

$$\hat{\mu}_i = \epsilon^2\mu_i \qquad A_j = \epsilon\alpha_j \qquad B_k = \beta_k \qquad \hat{F}_i = \epsilon(f_{i1}\cos(\Omega_1\tau + \tau_{i1}) + f_{i2}\cos(\Omega_2\tau + \tau_{i2}))$$
$$i = 1, 2\ ; \quad j = 1, 2\ldots, 6\ ; \quad k = 1, 2, \ldots, 8 \tag{5.21}$$

Substituting (5.9), (5.10), (5.21) into (5.5) and collecting terms of order ϵ and order ϵ^3 gives

$$D_0^2\eta_1 + \omega_1^2\eta_1 = f_{11}cos(\Omega_1 T_0 + \tau_{11}) + f_{12}cos(\Omega_2 T_0 + \tau_{12}) \tag{5.22a}$$
$$D_0^2\phi_1 + \omega_2^2\phi_1 = f_{21}cos(\Omega_1 T_0 + \tau_{21}) + f_{22}cos(\Omega_2 T_0 + \tau_{22}) \tag{5.22b}$$

$$D_0^2\eta_3 + \omega_1^2\eta_3 = -2D_0D_2\eta_1 - 2\mu_1 D_0\eta_1 + \alpha_1\eta_1^2 + \alpha_2\eta_1\phi_1 + \alpha_3\phi_1^2 + \beta_1\eta_1^3 + \beta_2\eta_1^2\phi_1 + \beta_3\eta_1\phi_1^2 + \beta_4\phi_1^3 \tag{5.23a}$$
$$D_0^2\phi_3 + \omega_2^2\phi_3 = -2D_0D_2\phi_1 - 2\mu_2 D_0\phi_1 + \alpha_4\eta_1^2 + \alpha_5\eta_1\phi_1 + \alpha_6\phi_1^2 + \beta_5\eta_1^3 + \beta_6\eta_1^2\phi_1 + \beta_7\eta_1\phi_1^2 + \beta_8\phi_1^3 \tag{5.23b}$$

The solution to (5.22) is given by

$$\eta_1 = P(T_2)e^{i\omega_1 T_0} + \Gamma_{11}e^{i\Omega_1 T_0} + \Gamma_{12}e^{i\Omega_2 T_0} + cc \tag{5.24a}$$
$$\phi_1 = Q(T_2)e^{i\omega_2 T_0} + \Gamma_{21}e^{i\Omega_1 T_0} + \Gamma_{22}e^{i\Omega_2 T_0} + cc \tag{5.24b}$$

where

$$\Gamma_{ij} = \frac{f_{ij}e^{\tau_{ij}}}{2(\omega_i^2 - \Omega_j^2)^2} \qquad i = 1, 2; \quad j = 1, 2$$

The response for the nonresonant case consists of the forced response at the excitation frequencies Ω_1 and Ω_2 as well as the free response close to the system natural frequencies. Typically, the free response term decays to zero owing to system damping, however, under particular conditions and a suitable set of system parameters, the free response term does not decay but has a steady state amplitude for a long time. This condition leads to a secondary resonance, and is the topic of investigation.

Substituting (5.24) into (5.23) reveals that additional secular terms appear in the RHS when the excitation frequencies are related to the linear natural frequencies by the following conditions

$$\begin{aligned}
\Omega_1 &\approx \frac{\omega_1}{3} & \Omega_2 &\approx \frac{\omega_1}{3}\\
\Omega_1 &\approx \frac{\omega_1}{2} & \Omega_2 &\approx \frac{\omega_1}{2}\\
\Omega_1 &\approx \frac{3\omega_1}{2} & \Omega_2 &\approx \frac{3\omega_1}{2}\\
\Omega_1 &\approx 2\omega_1 & \Omega_2 &\approx 2\omega_1\\
\Omega_1 &\approx 3\omega_1 & \Omega_2 &\approx 3\omega_1\\
\Omega_1 &\approx 4\omega_1 & \Omega_2 &\approx 4\omega_1\\
\Omega_1 &\approx 5\omega_1 & \Omega_2 &\approx 5\omega_1\\
\Omega_2 \pm \Omega_1 &\approx \omega_1 & \Omega_2 \pm \Omega_1 &\approx 3\omega_1\\
2\Omega_1 \pm \Omega_2 &\approx \omega_1 & 2\Omega_2 \pm \Omega_1 &\approx \omega_1\\
\Omega_2 - 2\Omega_1 &\approx \omega_1
\end{aligned} \tag{5.25}$$

$$\begin{aligned}
\Omega_1 &\approx \frac{\omega_2}{4} & \Omega_2 &\approx \frac{\omega_2}{4}\\
\Omega_1 &\approx \frac{\omega_2}{3} & \Omega_2 &\approx \frac{\omega_2}{3}\\
\Omega_1 &\approx \frac{\omega_2}{2} & \Omega_2 &\approx \frac{\omega_2}{2}\\
\Omega_1 &\approx \frac{3\omega_2}{4} & \Omega_2 &\approx \frac{3\omega_2}{4}\\
\Omega_1 &\approx \frac{3\omega_2}{2} & \Omega_2 &\approx \frac{3\omega_2}{2}\\
\Omega_1 &\approx 2\omega_2 & \Omega_2 &\approx 2\omega_2\\
\Omega_2 \pm \Omega_1 &\approx \frac{\omega_2}{2} & \Omega_2 \pm \Omega_1 &\approx \frac{3\omega_2}{2}\\
\Omega_2 \pm \Omega_1 &\approx \omega_2 & \Omega_2 \pm \Omega_1 &\approx 2\omega_2\\
2\Omega_1 \pm \Omega_2 &\approx \omega_2 & 2\Omega_2 \pm \Omega_1 &\approx \omega_2\\
\Omega_2 - 2\Omega_1 &\approx \omega_2
\end{aligned} \tag{5.26}$$

Equations (5.25) and (5.26) only list conditions for which additional secular terms appear in the solvability conditions. The existence of a nontrivial solution to the solvability conditions implies the existence of a nonzero free response, i.e. occurrence of a secondary resonance, and it depends strongly on the system parameters. The focus in this chapter is to identify

excitation frequencies and their combinations that potentially lead to a secondary resonance. The existence of nontrivial solutions to the solvability conditions for each case is therefore not discussed.

5.3 Results and Discussion

The discussion pertains to results presented for the system parameters in Table 5.1 unless mentioned otherwise. The force displacement relation for the trailing end spring using these parameters is plotted in Fig 5.6 for the linear as well as nonlinear cases.

5.3.1 Primary resonance ($\Omega \approx \omega_1$)

Linear damped system ($k_{12} = 0$, $k_{13} = 0$)

For the linear system (i.e. when nonlinearities are absent: $k_{12} = 0$, $k_{13} = 0$) the responses of the two modes η and ϕ are decoupled. The frequency response plot, which shows the steady state amplitude of oscillations as a function of detuning σ_2 (a measure of the closeness of to primary resonance condition) is shown by the dotted curves in Fig 5.7. For the linear damped case, the frequency response curve is always a single valued function of σ_2, and it has a peak in the first modal coordinate (η) at $\sigma_2 = 0$ corresponding to a resonance condition of the linear system. The steady state amplitude of forced oscillations in the second modal coordinate (ϕ) is small compared to that for η because the frequency of excitation Ω is far away from ω_2.

Nonlinear damped system with only quadratic nonlinearities ($k_{12} \neq 0$, $k_{13} = 0$)

When nonlinearities of only the quadratic form are included ($k_{12} \neq 0$, $k_{13} = 0$), the frequency response curves for both modes can be significantly altered depending on the system parameters. Two important cases need consideration when nonlinearities are included: (a) when ω_2 is far away from $2\omega_1$ (no internal resonance), and (b) when $\omega_2 \approx 2\omega_1$ (internal resonance).

When ω_2 is far away from $2\omega_1$ (no internal resonance), the system modes are decoupled to first order, and the frequency response curves are equivalent to that of the linear case. However, when $\omega_2 \approx 2\omega_1$ (internal resonance), the frequency response curve is significantly altered from that of the linear case. The two modes become strongly coupled and the curve may become a multivalued function of σ_2 depending on the system parameters. The frequency response plot is shown in Fig 5.7 for $\omega_2 \approx 2\omega_1$ (i.e. $\sigma_1 \approx 0$). It is evident that in certain ranges, for example, when $\sigma_2 \approx \pm 6$, there are two values at which the response could occur for a given value of σ_2. The actual amplitude of the system response is determined by the initial condition. A strong coupling of modes due to internal resonance leads to a much higher response in the second mode in the nonlinear case compared to the linear case. Additionally, the single peak in the first mode at $\sigma_2 = 0$ for the linear case is altered into two peaks at $\sigma_2 \approx \pm 6$ for the nonlinear case, implying that the largest response in the first mode occurs when Ω is slightly away from ω_1. As the system parameter σ_2 is changed (i.e the excitation frequency Ω is increased or decreased), the well known jump phenomena

characteristic to nonlinear systems occurs. When σ_2 is increased from the left the amplitude of steady state oscillations follows the solid line, and when σ_2 is decreased from the right the amplitude of steady state oscillations follows along the dashed line. Two jumps are evident in both cases (increasing and decreasing σ_2) corresponding to the region where the response curve is a multivalued function of σ_2. A jump occurs when the system moves from a region of multivalued solutions to a region with unique solution as discussed below considering a damped system including cubic and quadratic nonlinearities.

Nonlinear damped system with cubic and quadratic nonlinearities ($k_{12} \neq 0$, $k_{13} \neq 0$)

For a damped system with cubic and quadratic nonlinearities ($k_{12} \neq 0$, $k_{13} \neq 0$), the frequency response curve depends on whether internal resonance occurs or not. An internal resonance could occur when $\omega_2 \approx 2\omega_1$, arising from quadratic nonlinearities, or when $\omega_2 \approx 3\omega_1$, arising from cubic nonlinearities. In this work the focus is on the first case as it is relevant to the values of ω_1 and ω_2 typically observed in the problem of slider air bearing systems with thermal protrusion.

When internal resonance is absent (ω_2 is far away from $2\omega_1$), the two modes are decoupled to first order. The response of the second mode (ϕ) is the same as that for linear forced response shown in Fig 5.7b. However, the response of the first mode (η) is altered from the linear response as shown in Fig 5.8. The effect of the cubic nonlinearity is to bend the linear response curve (to the right, because the cubic nonlinearity stiffens the system in this case), and the curve may become a multivalued function of σ_2. The curve presented for the nonlinear case in Fig 5.8 is obtained from an analytical closed form expression derived in [Nayfeh and Mook 1979]. As σ_2 is increased from the left, the steady state amplitude of oscillations change along the curve $ABCEF$, while the steady state amplitude of oscillations trace the curve $FEDBA$ as σ_2 is decreased. The jump down CE in the forward direction, and the jump up DB in the reverse direction arise because the response curves move from a region of σ_2 where multiple solutions exist, to a region where only a unique solution exists to the response amplitude. The difference in the location of the jumps for increasing and decreasing σ_2 leads to a hysteresis loop. The portion DC of the response curve which lies in the hysteresis loop corresponds to unstable equilibria of (5.20) that are not physically realizable. The jumps in Fig 5.7 are similar to the jumps in Fig 5.8. In Fig 5.7, the branch of unstable equilibria between the two hysteresis loops (similar to the portion DC of Fig 5.8) is not shown because it is not detected by the simple numerical scheme used in this work to compute the equilibria of (5.20).

When an internal resonance occurs ($\omega_2 \approx 2\omega_1$), the two modes get strongly coupled. The frequency response curves for this case are shown in Fig 5.9. The amplitude of the second mode is significantly higher in this case even when the excitation frequency is far away from ω_2. Comparing the frequency response curves for the first mode with previous cases, it is noted that the response curve for this case is similar to that in Fig 5.7 with the two peaks altered in amplitude and bent (to the right) because of the inclusion of cubic nonlinearities. The jump occurring near $\sigma_2 = 0$ for the chosen set of parameters is of particular interest because it implies that when Ω is close to ω_1, as would happen in the slider air bearing system model where the lubricant rippling occurs close to the first pitch mode frequency

for the slider, a very small change in Ω could lead to a very large change in the resulting amplitude of oscillations. Depending on other system parameters, the detuning between the lubricant rippling frequency Ω and the first pitch mode frequency ω_1 dictates whether the slider has a large amplitude response or a suppressed amplitude response suggesting a good explanation for the suppressed amplitude of the slider vibrations observed in experiments.

The frequency response curves are plotted in Fig 5.10 for various values of α (the measure of thermal protrusion). Noting that changing α changes the detuning σ_1 (Fig 5.11), these plots may also be viewed as frequency response curves for changing σ_1 (a measure of closeness to the internal resonance condition $\omega_2 = 2\omega_1$). In Fig 5.10, by fixing the excitation frequency at say $\Omega = \omega_1$ ($\sigma_2 = 0$), it is seen that the amplitude of oscillations for particular values of α (or σ_1) are given by the points where the line $\sigma_2 = 0$ (the *ordinate*) intersects the frequency response curves. In particular, from Fig 5.10, it is evident that for $\alpha = 2.000$ and $\alpha = 2.075$ the *ordinate* intersects the frequency response curves at two points, but for $\alpha = 2.150$ the *ordinate* intersects the frequency response curves at only one point. The locus of the points of intersection of the frequency response curves with $\sigma_2 = 0$ is plotted as a function of σ_1 in Fig 5.12, where the solid and dashed lines denote the points of intersection of the *ordinate* with the solid and dashed lines, respectively, in frequency response curves of Fig 5.10. The plots reveal that near $\sigma_1 \approx 0$, a very slight change in σ_1 could lead to a very large change in the amplitude of oscillations. Particularly, increasing σ_1 above zero results in a sudden drop in the amplitude of oscillations of the first mode. This result is very interesting because it implies that for the slider air bearing system, assuming that the excitation frequency (lubricant rippling Ω) is perfectly tuned to the air bearing first pitch mode ω_1, a small change in the thermal protrusion could lead to a sudden suppression of slider vibration amplitude, offering a very plausible explanation of the suppressed vibration 'stable' zone seen in experiments at high heater power.

Similar plots are shown in Fig 5.13 for $\sigma_2 = \pm 0.5$. It is interesting to note that when $\sigma_2 = -0.5$, an increase in σ_1 does not lead to a downward jump in the amplitude of oscillations of the first mode. Such a condition may also occur for a different set of system parameters even when $\sigma_2 = 0$. In other words, certain slider designs may not exhibit the sudden suppression in vibrations for increasing thermal protrusion. The experimental results for one such case are shown in Fig 5.14, where an increase in heater power beyond the TDP does not show any suppression of the slider vibrations or AE signal.

The time histories of responses are plotted in Fig 5.15 for the linear case, and the two solutions for the nonlinear case when $\alpha = 2.075$ ($\sigma_1 = .0463$) and $\sigma_2 = 0$. The amplitudes of oscillations (ζ,θ) are much smaller for one solution of the nonlinear case and corresponds to the case of suppressed vibrations.

The key findings from the foregoing nonlinear analysis may be summarized to explain the peculiar slider dynamics seen in experiments. When the thermal protrusion causes the natural frequencies of the slider air bearing system to pass through an internal resonance, the amplitude of vibrations can significantly increase because of an unfavorable coupling of modes. Depending on system parameters a further change in thermal protrusion can result in a sudden suppression of vibrations because of the way nonlinearities interact within the system.

The external force (F) and system damping can also have a dramatic influence on the amplitude of oscillations. To demonstrate this effect Fig 5.16 and Fig 5.17 show the frequency

response plots for different values of external force and damping, respectively. The other system parameters used in this calculation are listed in Table 5.1. It is evident from these figures that the occurrence as well as location of jumps, and the amplitude of oscillations are strongly influenced by the external force and damping. At a given damping percentage, a jump (multiple response amplitudes for a given σ_2) can occur only if the external force amplitude is above a critical value, and similarly for a given external force amplitude, a jump can occur only if the damping is below a critical value. The magnitude of external force and damping, together with the frequency of the external forcing can therefore significantly alter the nonlinear system's response.

Dynamic frequency response plots

The frequency response plots presented so far show the amplitude of oscillations at steady state as a function of σ_2. They are called the *stationary* frequency response curves, and are the solutions of the equilibrium equations (5.20) associated with the differential equations (5.18). The *dynamic* frequency response curves can be obtained by integration of (5.18) from σ_{2i} to σ_{2f} and assuming $\sigma_2 = \sigma_{2i} + sT_2$ where s is the rate of change of σ_2. These dynamic curves may be viewed as the envelope of the transient time histories of oscillations of the two modes as σ_2 is increased or decreased (i.e. when passing through a resonance). The equilibrium solution of (5.20) with $\sigma_2 = \sigma_{2i}$ is used as the initial condition for this integration. The dynamic frequency response plots obtained in this manner are plotted for the case of only quadratic nonlinearities (Fig 5.18), and for the case of cubic as well as quadratic nonlinearities (Fig 5.19) for $s = 0.5$. It is evident that the dynamic curves follow the stationary curves fairly well but show oscillations after encountering a jump. Smaller values of s cause the dynamic curves to asymptote to the stationary curves, while larger values of s cause them to deviate from the stationary curves.

5.3.2 Secondary resonance

For the nonresonant case (Ω far away from ω_1 or ω_2), the nonlinear analysis shows that when the excitation frequencies are related to ω_1 and ω_2 through one of the particular combinations listed in (5.25) and (5.26) a secondary resonance can potentially occur and result in interesting system dynamics.

For the two frequency excitation case considered in this work, two of the conditions in (5.25) and (5.26) (also referred to as the secondary resonance conditions), can be satisfied simultaneously. Considering the special case of internal resonance ($\omega_2 \approx 2\omega_1$), the combinations under which two secondary resonance conditions are satisfied simultaneously are calculated. The result obtained is that two secondary resonance conditions are satisfied simultaneously when the excitation frequencies Ω_1 and Ω_2 are related to ω_1 through a multiplicative constant c and satisfy two of the conditions listed in (5.25) or (5.26). The actual manifestation of this secondary resonance is determined by the system parameters, and it occurs only when the solvability conditions for a simultaneous occurrence of secondary resonance has nontrivial solutions. The possible values that the parameter c may take are listed

below

$$c = 1, 2, 3, \ldots, 14 \tag{5.27a}$$

$$c = \frac{1}{3}(1, 2, 4, 5, 7, 8, 10, 11, 13, 14) \tag{5.27b}$$

$$c = \frac{1}{2}(1, 3, 5, 7, 9) \tag{5.27c}$$

$$c = \frac{1}{6}(5, 7) \tag{5.27d}$$

$$c = \frac{1}{4}(3, 5) \tag{5.27e}$$

$$c = \frac{1}{5}(1, 2, 3, 4, 6) \tag{5.27f}$$

For a three frequency excitation, three secondary resonance conditions can be satisfied simultaneously, and the list for c would include more values. When a secondary resonance does occur, the frequency spectrum of the system response consists of a free response close to the linear natural frequencies ω_m tuned by the nonlinearities in addition to the forced response at the excitation frequencies Ω_n. Since the forcing frequencies Ω_n are related to ω_m through various fractions c, the system response spectrum shows peaks corresponding to these *fractional harmonics*, which include *superharmonics* and *subharmonics* of the second and third order arising from the system quadratic and cubic nonlinearities, respectively [Nayfeh and Mook 1979].

The theoretical predictions of fractional harmonics arising from the two simultaneous secondary resonance conditions are shown in Table 5.2. The value $\omega_1 = 128kHz$ is the experimentally observed air bearing first pitch mode frequency for this slider air bearing system. All of the frequencies experimentally observed in the spectrum of slider vibrations (Fig 5.3) are well predicted by this theory. The only significant peak that appears in the experimental results, but is not predicted from theory is at $233kHz$. Investigation reveals that this frequency corresponds to the fractional harmonic with $c = \frac{11}{6}$, and it is predicted from theory if a three term excitation is considered. It is pointed out that not all of the theoretically predicted frequencies are seen in the experiments. This is not surprising since even though a secondary resonance is potentially predicted from theory, it may not actually occur because nontrivial solutions to the solvability conditions do not exist for the chosen set of system parameters.

5.3.3 HDI design considerations

The results of the analytical work reveal important insight into the dynamics of a slider under the effect of thermal protrusion. It is shown that, depending on the system parameters, the nonlinearities at the HDI in combination with thermal protrusion can lead to interesting system dynamics for particular ranges of protrusion. These include the strong coupling of modes through internal resonance leading to large amplitude oscillations and the sudden suppression/increase in oscillation amplitude due to jump conditions.

An internal resonance can lead to a large amplitude slider response because of an unfavorable coupling of vibration modes, and this can result in slider-lubricant/disk contact

or enhance existing slider-lubricant/disk contact. In order to avoid this condition, the ABS should be designed to have pitch mode frequencies such that $\omega_2 > 2\omega_1$ with zero heater power, so that thermal protrusion results in the system response moving away from an internal resonance condition (because ω_2 increases and ω_1 remains largely unaffected by thermal protrusion). If $\omega_2 < 2\omega_1$ with zero heater power, it may be desirable to transition through the internal resonance condition in the low heater power range, because in that case, the thermal protrusion is small and the head-disk clearance is relatively large, leaving a greater margin to accommodate any large amplitude vibrations arising from an internal resonance. Internal resonance and the resulting large amplitude vibrations can also be used favorably, for example, by intentionally inducing internal resonance and detecting slider vibrations with a magnetic signal, one can ascertain the fly-height of the slider.

Only the pitch and vertical degrees of freedom are considered in this work, but the analysis can be extended to a three degree of freedom model that includes slider roll. The internal resonance conditions for the three degree of freedom model are $\omega_m \approx 2\omega_n$ or $\omega_m \approx 3\omega_n$ for $m, n = 1, 2, 3$, and a coupling of modes as well as interesting system dynamics can occur when thermal protrusion leads to an internal resonance condition.

This analytical study also highlights the role of lubricant rippling, or other periodic excitation in determining slider dynamics. Since a small difference in the frequency of the excitation and the first pitch mode frequency of the slider can result in very different amplitudes of response, it is inferred that the ability of the lubricant to ripple as well as recover/relax needs important consideration from the perspective of having favorable slider dynamics.

5.4 Conclusion

Slider instability and dynamics at touchdown/contact are investigated in this chapter through experiments and analytical modeling. The experiments reveal that for certain slider designs, when the heater power is increased beyond a critical power above the TDP the slider vibrations are suddenly suppressed. A simple two degree of freedom model that accounts for nonlinearities at the HDI through quadratic and cubic approximations is used to analytically investigate the interesting features of this problem. It is shown that the thermal protrusion induced by the heater can cause the system modes to couple unfavorably for certain heater power ranges. This condition can manifest as large amplitude slider vibrations and result in slider-lubricant/disk contact or enhance the existing slider-lubricant/disk contact. System nonlinearities can also lead to a favorable suppression/reduction of slider vibration amplitudes through the jump phenomena characteristic to many nonlinear systems. Excitation frequencies that result in large amplitude slider vibrations, and the dominant frequencies at which the slider's response occurs are also predicted by the theory, and they are in excellent agreement with the experimental results. The theoretical analysis in this work highlight HDI design considerations that can prevent slider instability as well as mitigate unwanted slider vibrations ensuring HDI reliability at extremely low head-disk clearance.

System Parameter	Value
Slider density (ρ)	$4425kg/m^3$
Slider length (L_s)	$1.33mm$
Slider width (w_s)	$0.83mm$
Slider height (h_s)	$0.23mm$
L_1	$L_s/2$
L_2	$0.75\ L_s/2$
k_{21}	$3.3 \times 10^5 N/m$
k_{11}	$\alpha k_{21}\ N/m$
k_{12}	$5 \times 10^7 k_{11}\ N/m^2$
k_{13}	$10^{15} k_{11}\ N/m^3$
$\hat{\mu}_1$	$0.01\omega_1$ (1%)
$\hat{\mu}_2$	$2\mu_1$
F	$2.3\ mN$
M	FL_1

Table 5.1: System parameters

Experimental: $\omega_1 = 128kHz$		
$c = p/q$	$\Omega = c\ \omega_1$	Seen in Experiments?
1/5	26	
1/3	43	
2/5	51	
1/2	64	
3/5	77	
2/3	85	Yes
3/4	96	
4/5	102	
5/6	107	Yes
1	128	Yes
7/6	149	
6/5	154	
5/4	160	
4/3	171	
3/2	192	Yes
5/3	213	Yes
2	256	Yes
7/3	299	Yes
5/2	320	
8/3	341	Yes
3	384	Yes
10/3	427	
7/2	448	
11/3	469	
4	512	

Table 5.2: Possible fractional harmonics when two secondary resonance conditions are simultaneously satisfied

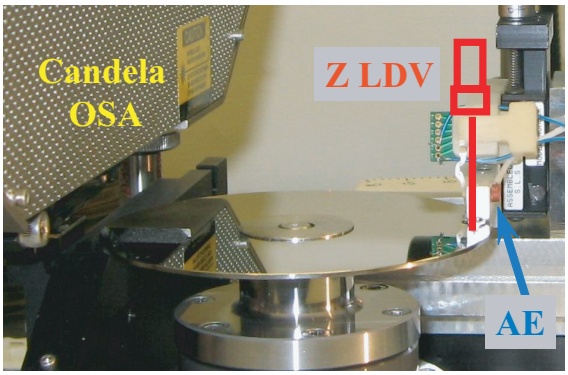

Figure 5.1: The spin stand experimental set-up with Candela OSA, AE sensor and LDV

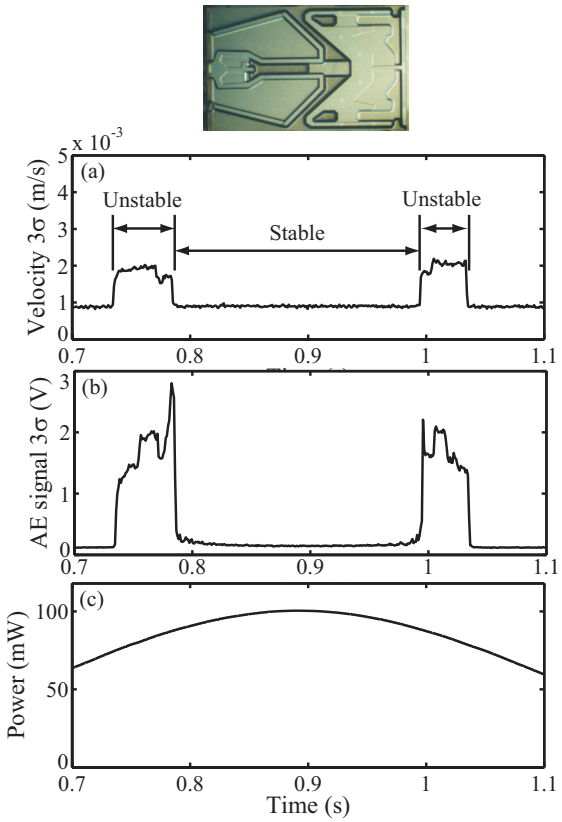

Figure 5.2: Experimental result for the 'pemto' slider: Time history of (a) slider's vertical velocity 3σ (b) AE signal 3σ (c) TFC heater power

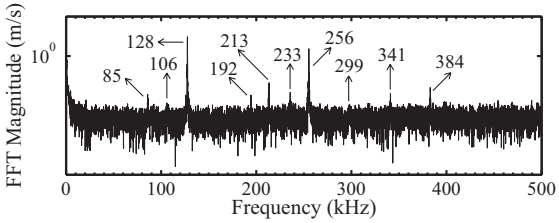

Figure 5.3: Frequency spectrum of the slider's vertical velocity in the 'unstable' zone

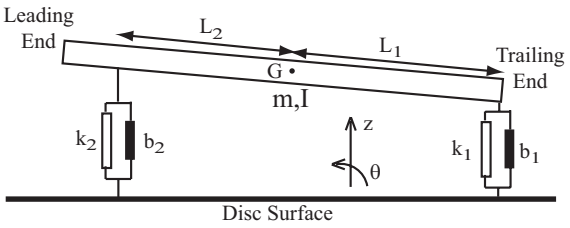

Figure 5.4: Schematic of the two degree of freedom model for slider air bearing system

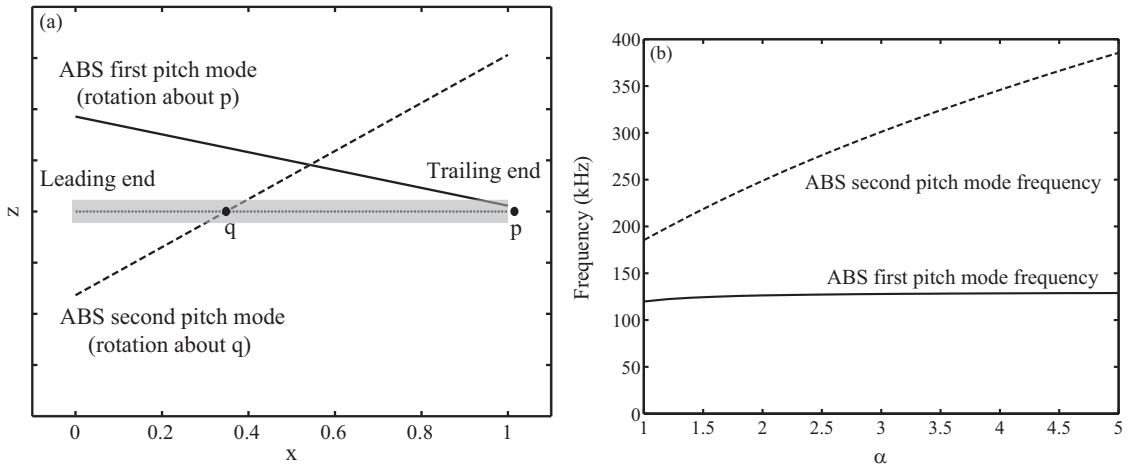

Figure 5.5: Linear model analysis: (a) Air bearing first and second pitch mode shapes (b) first and second pitch mode frequencies as a function of thermal protrusion 'α'

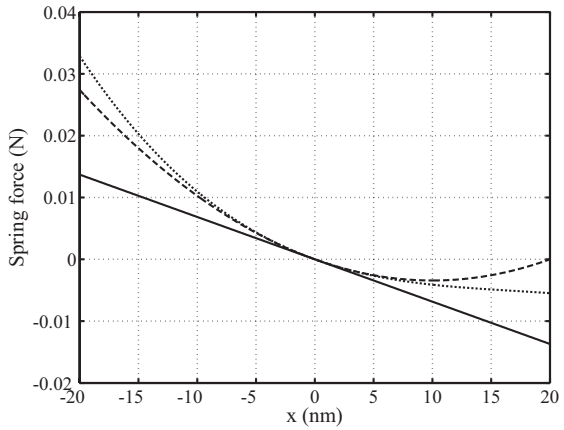

Figure 5.6: Displacement-force plot for the trailing edge spring; $k_{21} = 3.3 \times 10^5$, $\alpha = 2.075$; — linear: $k_{11} = \alpha k_{21}$, $k_{12} = k_{13} = 0$; $--$ quadratic nonlinearity: $k_{11} = \alpha k_{21}$, $k_{12} \neq 0$, $k_{13} = 0$; $\cdots$ quadratic and cubic nonlinearity: $k_{11} = \alpha k_{21}$, $k_{12} \neq 0$, $k_{13} \neq 0$

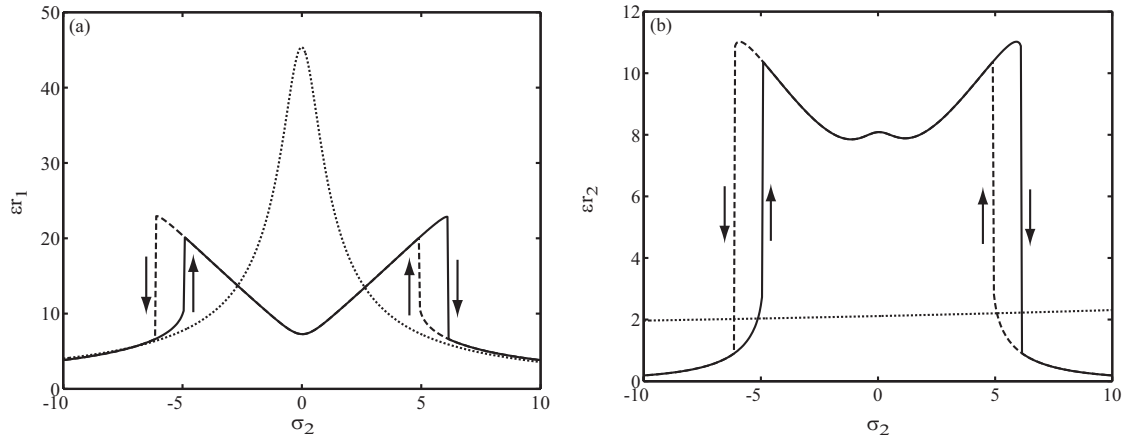

Figure 5.7: Frequency response plot for the linear damped system and the damped system with only quadratic nonlinearities when $\omega_2 \approx 2\omega_1$ (a) First modal coordinate η (b) Second modal coordinate ϕ; $\cdots$ linear case; — nonlinear case with increasing σ_2; $--$ nonlinear case with decreasing σ_2

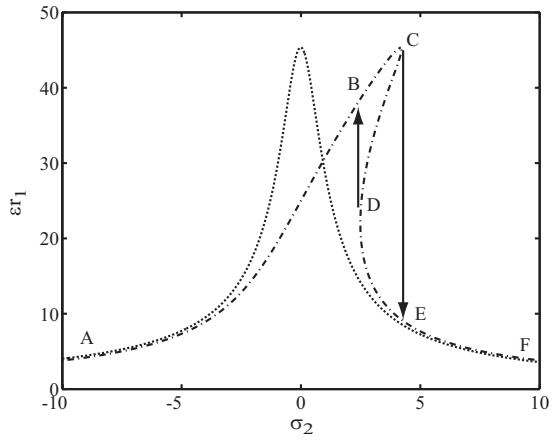

Figure 5.8: Frequency response plot for the first modal coordinate η; $\cdots$ linear damped case; $-\cdot-$ damped case with cubic nonlinearities but no internal resonance

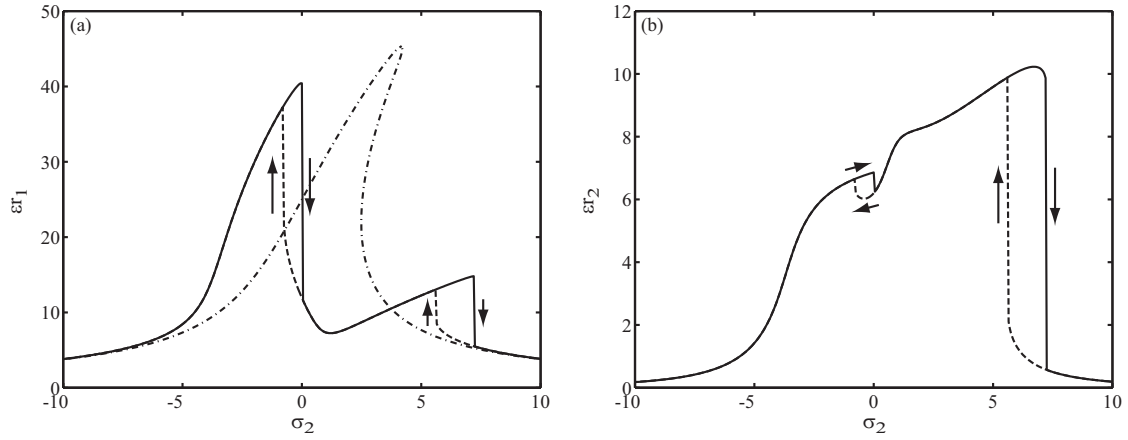

Figure 5.9: Frequency response plot for the damped system with quadratic and cubic nonlinearities (a) First modal coordinate η (b) Second modal coordinate ϕ; $-\cdot-$ no internal resonance; — internal resonance ($\omega_2 \approx 2\omega_1$) with increasing σ_2; $--$ internal resonance ($\omega_2 \approx 2\omega_1$) with decreasing σ_2

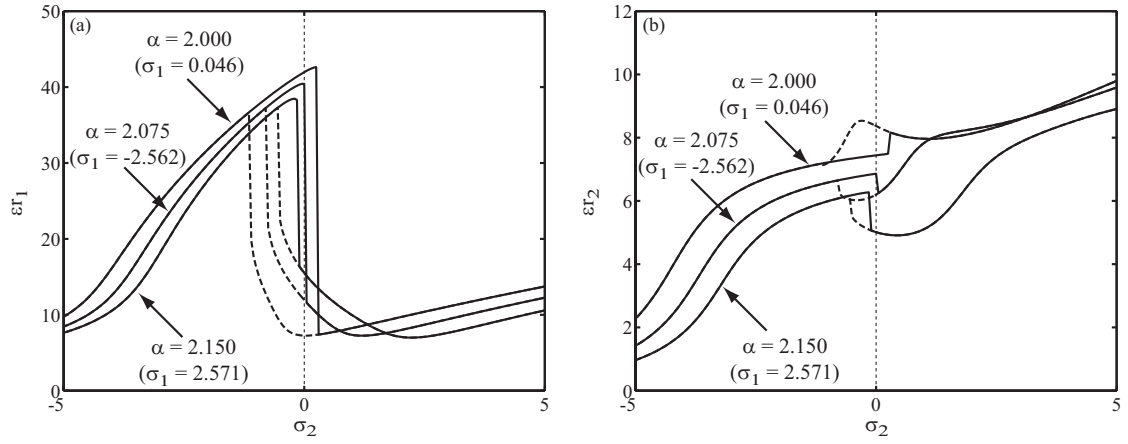

Figure 5.10: Frequency response plot for the damped system with quadratic and cubic nonlinearities showing the effect of α (a) First modal coordinate η (b) Second modal coordinate ϕ; — internal resonance ($\omega_2 \approx 2\omega_1$) with increasing σ_2; $--$ internal resonance ($\omega_2 \approx 2\omega_1$) with decreasing σ_2

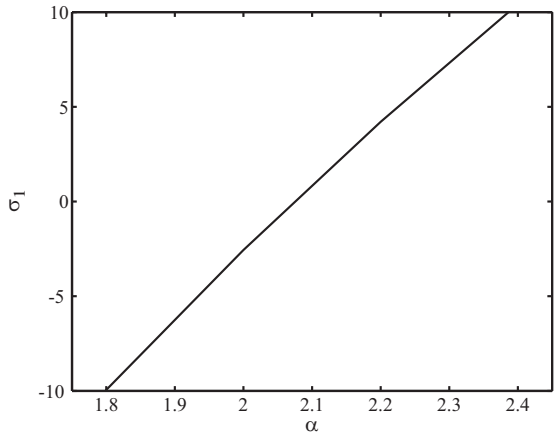

Figure 5.11: Effect of thermal protrusion 'α' on the internal resonance detuning parameter 'σ_1'

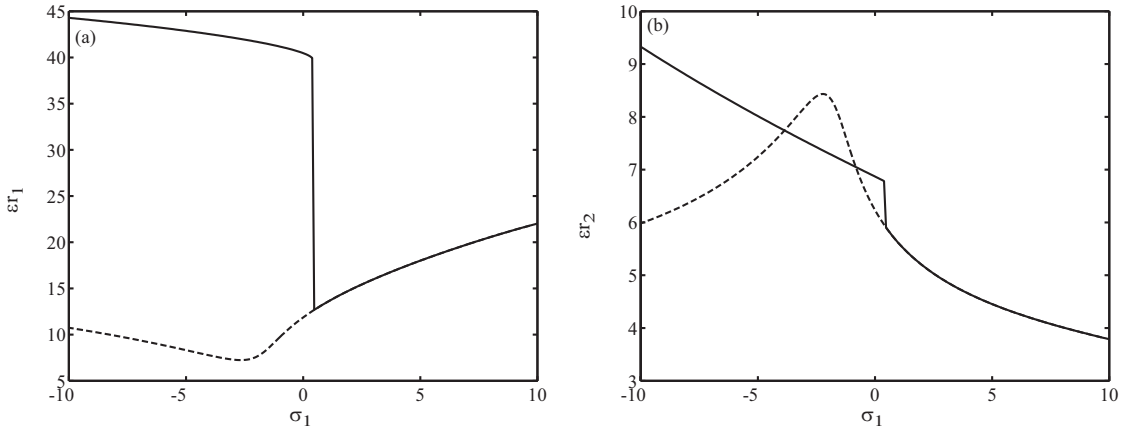

Figure 5.12: Response amplitude as function of σ_1 for $\sigma_2 = 0$ for the damped system with quadratic and cubic nonlinearities (a) First modal coordinate (b) Second modal coordinate

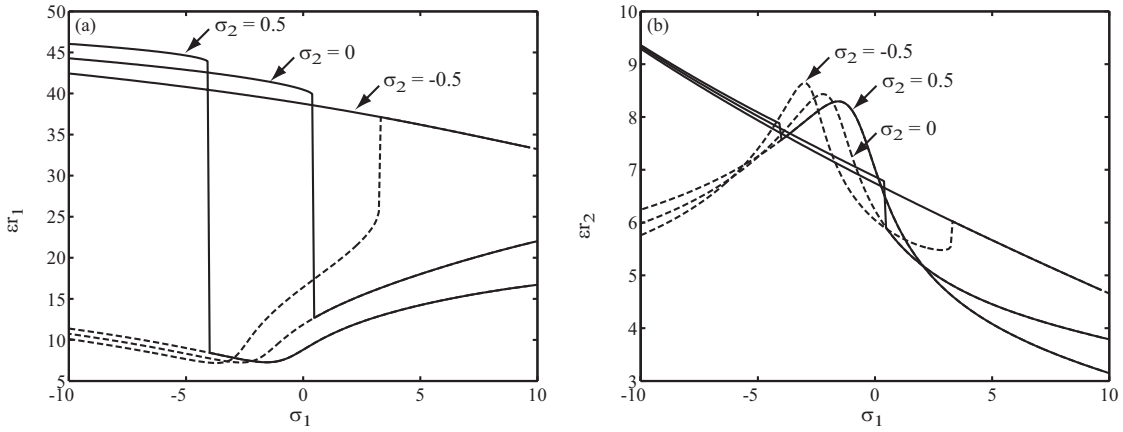

Figure 5.13: Response amplitude as function of σ_1 for the damped system with quadratic and cubic nonlinearities showing the effect of σ_2 (a) First modal coordinate (b) Second modal coordinate

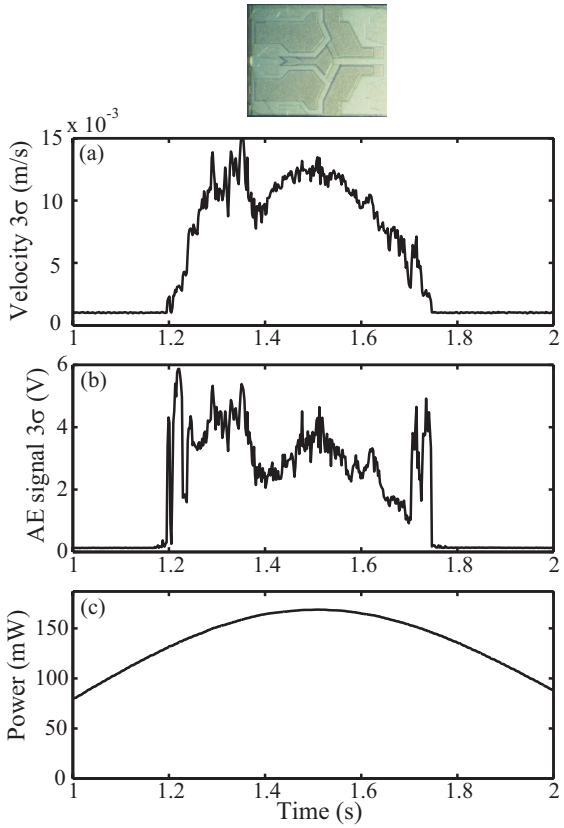

Figure 5.14: Experimental result for the 'femto' slider: Time history of (a) slider's vertical velocity 3σ (b) AE signal 3σ (c) TFC heater power

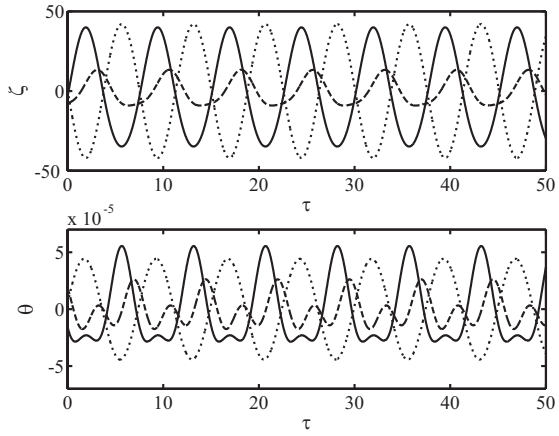

Figure 5.15: Time history of response for linear damped system and damped system with quadratic and cubic nonlinearities when $\alpha = 2.075$ ($\sigma_1 = 0.046$) and $\sigma_2 = 0$; $\cdots$ linear case; — nonlinear case with large amplitude response; $--$ nonlinear case with suppressed amplitude response

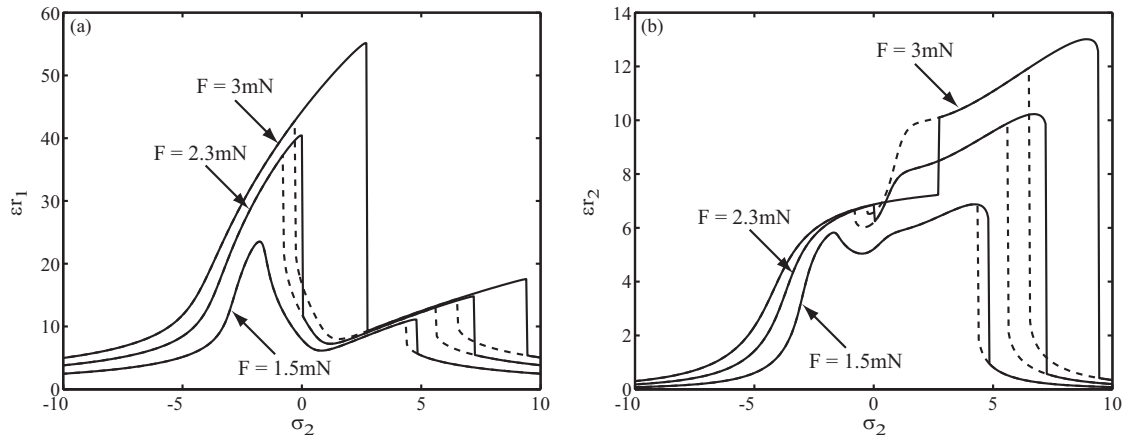

Figure 5.16: Effect of external force on the frequency response plot for the damped system with quadratic and cubic nonlinearities and internal resonance ($\alpha = 2.075$) (a) First modal coordinate (b) Second modal coordinate; — increasing σ_2; $--$ decreasing σ_2

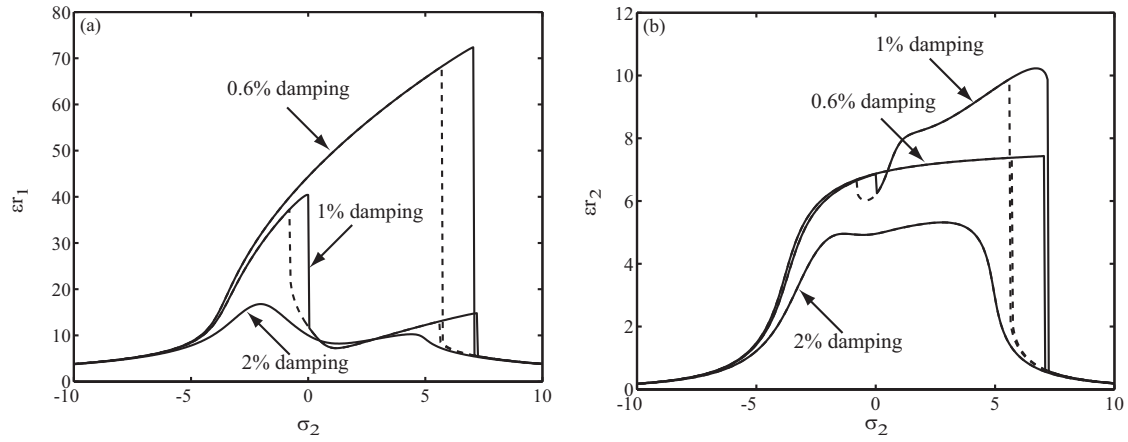

Figure 5.17: Effect of damping on the frequency response plot for the damped system with quadratic and cubic nonlinearities and internal resonance ($\alpha = 2.075$) (a) First modal coordinate (b) Second modal coordinate; — increasing σ_2; −− decreasing σ_2

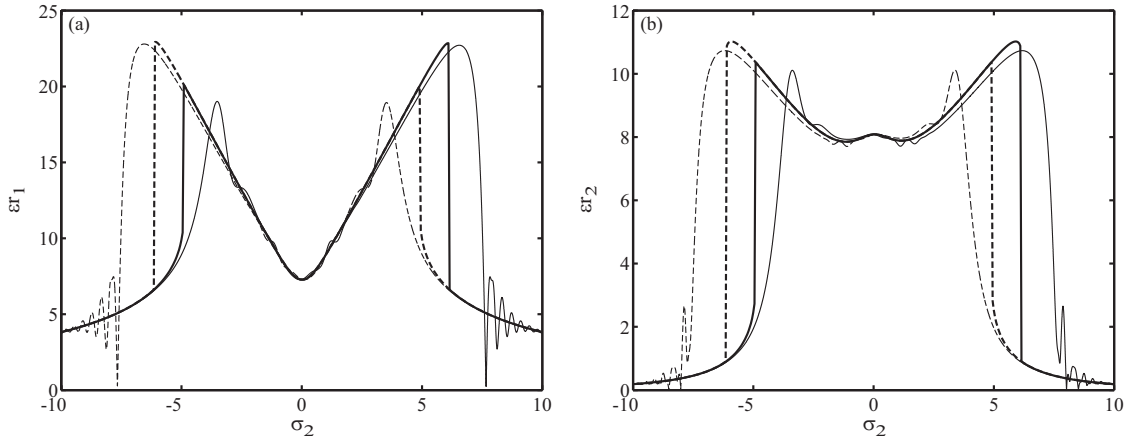

Figure 5.18: Dynamic and stationary frequency response plot for the damped system with only quadratic nonlinearities and internal resonance ($\alpha = 2.075$) (a) First modal coordinate (b) Second modal coordinate; — increasing σ_2; −− decreasing σ_2; bold lines represent the *stationary* curves

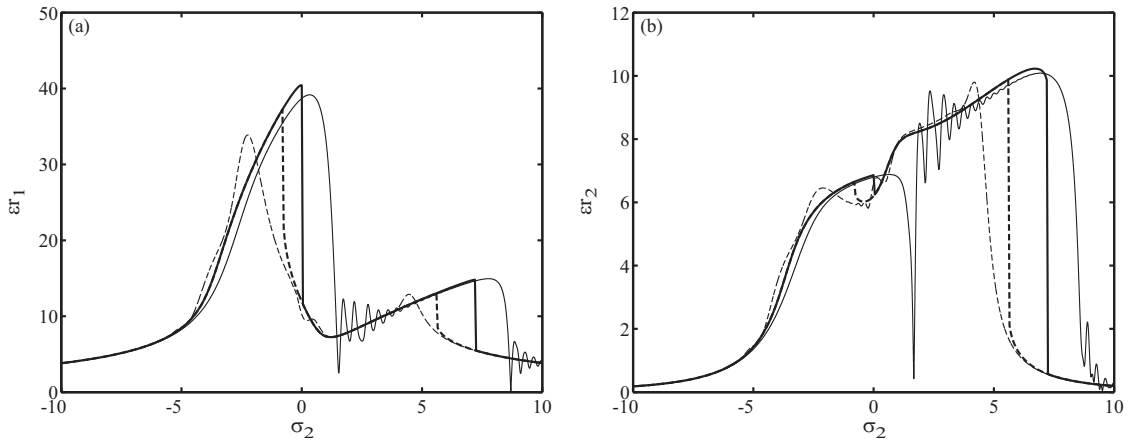

Figure 5.19: Dynamic and stationary frequency response plot for the damped system with quadratic and cubic nonlinearities and internal resonance ($\alpha = 2.075$) (a) First modal coordinate (b) Second modal coordinate; — increasing σ_2; −− decreasing σ_2; bold lines represent the *stationary* curves

Chapter 6

Parametric Investigations at the Head-Disk Interface of Thermal Fly-height Control Sliders in Contact

The touchdown and contact dynamics of thermal fly-height control (TFC) sliders is explained in Chapter 4 and Chapter 5 through experiments and modeling. Accurate touchdown power (TDP) detection is a pre-requisite for head-disk spacing calibration and control in current hard-disk drives (HDD), especially as the physical spacing targets reach subnanometer values. Slider and head gimbal assembly (HGA) designs have a significant influence on the touchdown behavior, and this chapter reports parametric investigations conducted to understand the touchdown process. The dominant modes/frequencies of excitation at touchdown can be significantly different leading to very different touchdown signatures. The pressure under the slider at touchdown and hence the TFC efficiency as well as the propensity for lubricant pick-up show correlation with touchdown behavior and may be used as metrics for designing sliders with good touchdown. Experiments are devised to measure friction at the head-disk interface (HDI) of a TFC slider actuated into contact, and several parametric investigations are conducted to study the effect of disk roughness, disk lubricant parameters and slider design (air bearing surface (ABS) and heater design) on friction as well as slider burnishing.

6.1 Experiments

Experiments are conducted using three different ABS designs mounted on the same suspension on a spin stand equipped with an acoustic emission (AE) sensor to detect contact and a laser doppler vibrometer (LDV) to detect vertical flexure motions on the HGA. The TDP (i.e. power required to achieve zero clearance or contact with the disk lubricant) is determined experimentally by supplying the TFC heater with a square pulse lasting $70ms$ with increasing power. The AE signal standard deviation is monitored during each power pulse, and the power at which the AE signal standard deviation crosses a specified threshold (set to be 20% above baseline) is recorded as the TDP.

6.2 Results and Discussion

6.2.1 Touchdown behavior/characteristics

The touchdown plots for three different ABS designs are shown in Fig 6.1 where ABS-3 shows a favorable 'sharp touchdown' while ABS-1 shows an unfavorable 'gradual touchdown' with a slow rise in AE signal for increasing TFC power. ABS-2 has touchdown performance which falls between ABS-1 and ABS-3. A sharp touchdown behavior is preferred as it better estimates the exact power at which contact with the disk lubricant is achieved.

The sharp touchdown for ABS-3 is characterized by strong individual spikes in the time history of the AE signal while the gradual touchdown for ABS-1 shows a uniformly increased AE signal during the TFC pulse as shown in Fig 6.2. (The AE signal on these plots have been shifted by $1V$ to show them clearly).

In addition, tests in overpush reveal that ABS-3 with 'sharp touchdown' shows an 'overshoot behavior' with very strong AE indicated contact at powers slightly above the TDP and a subsequent suppression of AE indicated contact when the power increases into overpush as seen in Fig 6.3. In contrast, ABS-1 with the 'gradual touchdown' shows no 'overshoot' behavior but a gradual increase in AE detected contact with overpush. ABS-2 has behavior in between those of ABS-3 and ABS-1.

Simulations for these three ABS designs show that the increasing sharpness of touchdown correlates with decreasing pressure under the TFC protrusion at touchdown, increased TFC efficiency and lower TDP (Table 6.1). It is also observed that lubricant pick-up is higher for ABS-3 compared to ABS-2 or ABS-1.

6.2.2 Analogous experimental results

A separate set of experiments with ABS-2 reveals that the touchdown can be sharp or gradual depending on the disk RPM (or the linear velocity) as shown in Fig 6.4. Specifically, a lower disk RPM increases the touchdown sharpness and a higher disk RPM degrades the touchdown sharpness. It is also observed that the touchdown performance degrades for a burnished slider (which is burnished in a controlled fashion by increasing the TFC power above the TDP on a separate disk track). The results for the 7200 RPM case on Fig 6.4 highlight the possibility of false TDP detection: for the same 20% AE threshold, the unburnished case shows a gradual AE rise untill about $95mW$, that precedes the sharp AE rise at $102mW$ which actually marks the TDP, however, the burnished case reads a false TDP at $93mW$ owing to the gradual rise in AE that occurs before the sharp AE rise marking touchdown. The time history of the AE signal is similar to that observed with the different ABS designs, namely, strong individual AE spikes appear for the 3600 RPM case with sharp touchdown, and a uniformly increased AE signal appears for the 7200 RPM case with gradual touchdown (Fig 6.5). These analogous results for ABS-2 provide a way to probe the same HDI under different disk RPM to understand the changes that occur in the AE and LDV signals for 'sharp' and 'gradual' touchdown signatures as well as in overpush (i.e. TFC power above the TDP).

6.2.3 LDV spectrum and AE signal content

Experiments are conducted with ABS-2 to simultaneously capture LDV (focused on flexure) and AE signals to identify the frequencies that correspond to the flexure and slider vertical motions, and to see how they appear in the AE signal. The tests are conducted with the power increased above the TDP (i.e. into overpush). For this ABS-2 design, the simulated air bearing frequencies at 5400 RPM and $1nm$ minimum spacing are $142kHz$ (roll), $167kHz$ (pitch 1) and $324kHz$ (pitch 2).

The LDV spectrum for overpush tests conducted at different RPM are shown in Fig 6.6, and the dominant excitation frequencies are identified on the plots. It is observed that for 3600 RPM, the lower frequencies (notably 139,148 and $165kHz$ which are close to simulated roll and pitch 1 air bearing frequencies) are dominant, while for the 7200 RPM, the higher air bearing frequency $321kHz$ (corresponding to pitch 2 air bearing frequency) is dominant. This result indicates that the mechanism/nature of touchdown and contact at the HDI is significantly altered by the disk RPM, and it is probably different for the three different ABS designs presented in section 6.2.1 in an analogous fashion.

The components of the AE signal at the different frequencies observed in the LDV signal are plotted in Fig 6.7 to observe how they change as a function of the TFC power. (The cumulative effect of adding all these components would result in the plot shown in Fig 6.4). At 3600 RPM the touchdown is marked by the sharp rise in the $148kHz$ component and there are no components that show gradual rise. At 5400 RPM, the $148kHz$ component shows a gradual rise, but touchdown is marked by a sharp rise in the $321kHz$ component. At 7200 RPM, there are no components with a sharp rise, and the $321kHz$ component shows a gradual rise.

These results indicate that at 3600 RPM the contact is dominated by the slider's pitch 1 and roll motions (together with any suspension related motions that give rise to frequency peaks in the $65-100kHz$ region.) At 7200 RPM, contact is mainly dominated by the vibration of the slider at the pitch 2 frequency. At 5400 RPM, the contact interaction is a combination of the above two modes at lower TFC powers causing a gradual rise, first in the $148kHz$ component, but eventually touchdown causes a strong vibration in the pitch 2 mode ($321kHz$).

These results are in agreement with recent studies that show that at close spacing and at the onset of lubricant-contact, in-plane shear forces and friction can destabilize the slider for certain ABS designs resulting in vibrations dominantly occurring at suspension and lower air bearing frequencies ($60-200kHz$ in our case) while stronger contact with the disk causes slider vibrations with higher frequency content (above $200kHz$) [Zeng et al. 2011].

6.2.4 Friction measurements in contact

Friction forces at the HDI become important during contact conditions and may in fact play a dominant role in HDI performance and slider dynamics. Friction induced slider wear as well as disk lubricant redistribution and disk overcoat damage need to be examined carefully to explore future designs that can accommodate a certain level of head-disk contact.

Experiments are devised to measure the friction forces in the downtrack direction during contact and overpush conditions by instrumenting a strain gage. Once the TDP is determined on the test track, the TFC is powered with a voltage profile having $100ms$ dwell time at the

maximum power. It is noted that strain gages have a low bandwidth and several experiments reveal that a dwell time of at least $100ms$ is necessary to allow the strain gage to respond to the friction force and give good, repeatable measurements. All experiments are conducted with ABS-2 on a reference 'standard disk' unless specified otherwise.

Friction, AE and slider bouncing in contact

Fig 6.8a and Fig 6.8b show the TFC voltage profile and the resulting slider bouncing (displacement and velocity), AE detected contact and the friction force for $10mW$ and $20mW$ overpush, respectively. It is evident that slider bouncing and AE signal remain high throughout the test for $10mW$ overpush and they get suppressed (after an initial overshoot region) for the $20mW$ overpush case. The friction force measured by the strain gage, however, continues to increase with the amount of overpush indicating a higher level of interference and contact for larger overpush powers even though the AE detected contact and slider dynamics get suppressed. (It is noted that the amplitude of the AE signal in the suppressed state is noticeably higher than the baseline AE signal with no TFC power, implying a certain amount of contact).

Effect of disk roughness

Disk roughness plays an important role in HDI performance. The combined slider and disk roughness affect the nominal physical spacing at the HDI, the magnitude of interaction forces (intermolecular/adhesive etc.) as well as the actual area of contact when it occurs, thereby influencing the magnitude of contact and friction forces. A parametric study is conducted with three disk types: Disk A, B and C with decreasing roughness, in that order, and with surface roughness parameters tabulated in Table 6.2, where, R_q is the root mean square roughness, R_p is the maximum peak height, and R_v is the maximum valley depth.

First, several tests are conducted using the same slider to determine the TDP on a standard disk and on each of the disks A,B and C. Table 6.2 presents the change in the TDP (i.e. δTDP) on each of the disks A,B and C compared to the TDP on a standard disk. This difference in TDP is converted into a clearance gain value (i.e. a gain in clearance from that on a standard disk) using a conversion factor of $0.119nm/mW$, which is the TFC efficiency estimated for ABS-2 from simulations. Fig 6.9 shows the same information in graphical form and highlights the linear relationship between the disk roughness (R_p or R_q) and clearance gain. Since the thermal protrusion comes into contact with the peaks of the roughness, the relationship between the clearance gain and R_p (Fig 6.9b) is of importance, and it is seen that for every $1nm$ decrease in R_p, there is a $0.8nm$ actual gain in clearance at the HDI for the range of surface roughness values considered in these experiments.

Next, the dependence of friction on the disk roughness is investigated by conducting a 'friction test' on each of the three disk types. A new (unburnished) slider is flown on a fresh test track, the TDP is determined, and the TFC heater is then supplied the power profile with a $100ms$ dwell time (as shown in Fig 6.8). The peak TFC power is increased from TDP to a maximum of $TDP+50mW$ in $5mW$ increments, and it is then similarly decreased back to TDP. The average friction measured by the strain gage at each power step is tabulated. All tests are conducted on the same disk track. The measured friction values are plotted as those for the 'unburnished' case. The same slider, which is now deemed 'burnished' because

of the overpush testing, is flown on an adjacent track and the friction test is repeated to obtain friction values for the 'burnished' case. Fig 6.10a shows a representative plot for the strain gage measured friction values as a function of overpush power supplied to the TFC heater.

A quadratic curve passing through the origin is fit to the friction measurements for the 'unburnished' and 'burnished' cases, and the slope of this curve at the $10mW$ overpush point is used to obtain the 'friction (μN) per *milliwatt* of overpush power' value. Fig 6.10b plots these friction values measured on the three disk types (A,B and C) based on experiments conducted with three new sliders on each disk type. While there is no particular trend relating the measured friction and surface roughness, the friction is higher for the burnished slider compared to the unburnished slider in all tests. Slider burnishing increases the actual contact area between the thermal protrusion and the disk, thereby resulting in the slightly higher friction force.

In order to directly compare the friction values between the three disk types, another set of experiments is conducted by flying the same 'burnished' slider (burnished in a controlled fashion separately) on the three disk types in succession. The friction against the overpush power is plotted in Fig 6.10c using data from two 'burnished' heads. It is concluded that there is no significant effect of the disk surface roughness on friction based on these results.

Effect of lubricant parameters

Friction tests are conducted to determine the effect of lubricant type/bonding on the friction in contact. Disks with three different lubricant type/bonding ratios are used: Lube A (61% bonded ratio, 10.5Å), Lube A (69% bonded, 10.5Å) and Lube B (82% bonded, 12Å). Fig 6.11a shows the friction measured for the three media for the unburnished and burnished cases (based on three experiments each). The friction values are comparable for the unburnished case for all three disks types. While the friction values for the burnished and unburnished cases are comparable for the disks with Lube A 61% and 69% bonded ratio, the friction for the burnished case on the disk with Lube B 82% bonded ratio is relatively higher than the unburnished case. This result is conistent with results for the change in TDP occurring because of a friction test, since the TDP change after and before a friction test is a measure of slider burnishing. As shown in Fig 6.11b, the highest burnishing (indicated by highest δTDP) occurs with an unburnished slider on the Lube B 82% bonded disk, and as a result, the friction is higher for the subsequent test conducted with this burnished slider.

A direct comparison of friction values is reported in Fig 6.11c based on tests conducted in succession on the three different disks using two 'burnished' sliders, and it shows marginally higher friction values for the disk with Lube B 82% bonded ratio.

Friction tests are conducted to understand the effect of the mobile part of the lubricant on friction and slider burnishing. The disk with Lube A 10.5Å 61% bonded fraction is delubed by immersing it in a solution of Vertrel XF solution to remove the mobile lubricant. The delubed disk has a lubricant thickness of 6Å (bonded lubricant). Fig 6.12a shows the measured friction on the lubed and delubed disks for the unburnished and burnished slider cases. While the friction values are comparable for the unburnished as well as burnished cases of the lubed disk and the unburnished case of the delubed disk, it is substantially higher for the burnished case of the delubed disk. Fig 6.12b shows that slider burnishing

(indicated by δTDP after a friction test) is higher for tests conducted on the delubed disk implying that an unburnished slider is substantially burnished on this disk type, and the friction is higher for the subsequent test conducted with such a burnished slider. Therefore the mobile part of the lubricant plays an important role in reducing friction as well as slider burnishing, thereby increasing the reliability of a HDI with contact.

Effect of TFC efficiency

The thermal protrusion size and shape make a significant difference in the slider's touchdown and contact behavior. The friction during contact for different slider ABS/heater designs are plotted in Fig 6.13 for the unburnished and burnished cases, and the same data is tabulated in Table 6.3 together with each design's TFC efficiency estimated from simulations. It is observed that the friction forces increases as the TFC efficiency increases.

Effect of disk RPM

The similarities between the touchdown plot and contact signature of ABS-2 at different disk RPMs to those of ABS designs with different TFC efficiencies is highlighted in section 6.2.2. Particularly, it is shown that at a higher RPM, ABS-2 behaves like a design with low TFC efficiency (showing a gradual touchdown plot), and at a lower RPM, ABS-2 behaves like a design with high TFC efficiency (showing a sharp touchdown plot).

The friction results in tests with ABS-2 at different RPM are consistent with the above analogy and the results presented in section 6.2.4. Fig 6.14 shows that the friction increases as the disk RPM decreases, i.e. when ABS-2 is made to behave like a slider with high TFC efficiency by decreasing RPM it exhibits the characteristic sharp touchdown plot and higher friction.

6.3 Conclusion

The touchdown behavior of TFC sliders is investigated through experiments. Certain sliders exhibit a sharp rise of acoustic emission (AE) signal at touchdown when the power is increased in milliwatt steps while others show a gradual rise making it difficult to exactly define the TDP to milliwatt resolution. An analogous behavior occurs when the disk RPM is changed for a particular slider ABS. It is found that the dominant modes/frequencies of excitation at touchdown are significantly different in these cases leading to the very different touchdown signatures. Particularly, the sharp touchdown case is characterized by strong individual contact events as observed in the AE signal, and the dominant excitation occurs at frequencies that correspond to the slider's first pitch and roll modes in addition to suspension related frequencies. In contrast, the gradual touchdown case is characterized by a uniform rise in AE signal over the duration of the TFC pulse, and the dominant excitation occurs at the slider's second pitch mode. The pressure under the TFC protrusion at touchdown, the TFC efficiency as well as the propensity for lubricant pick-up show correlation with touchdown behavior and may be used as metrics for designing sliders with good touchdown features. Experiments are devised to measure the friction at the HDI during TFC induced contact, and several parametric investigations are carried out. Disk surface roughness does

not significantly affect the friction during contact. The mobile part of the lubricant plays an important role in reducing friction as well as slider burnishing. A burnished slider shows a higher friction value than an unburnished slider, and sliders with higher TFC efficiency show higher friction compared to sliders with lower TFC efficiency.

ABS design	Simulation TFC efficiency nm/mW	Touchdown power mW	Pressure at touchdown $atm.$
ABS-1	0.108	96	60
ABS-2	0.119	91	38
ABS-3	0.145	69	27

Table 6.1: Simulated results for the three different ABS designs

Disk	R_p nm	R_q nm	R_v nm	δTDP mW	Clearance gain nm
A	2.02	0.49	1.87	0.08	0.01
B	1.89	0.36	1.47	0.97	0.12
C	1.00	0.24	1.11	6.71	0.84

Table 6.2: Disk roughness parameters and its effect on TDP/clearance gain

ABS design	Simulation TFC efficiency nm/mW	Friction Unburnished $\mu N/mW$	Friction Burnished $\mu N/mW$
ABS-A	0.108	9	17
ABS-B	0.111	24	31
ABS-C (ABS-2)	0.119	37	54
ABS-D (ABS-3)	0.145	56	67

Table 6.3: Effect of TFC efficiency (ABS/heater design) on friction

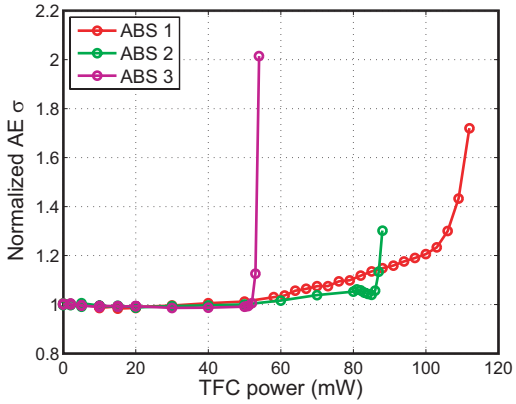

Figure 6.1: Touchdown plots for the three different ABS designs

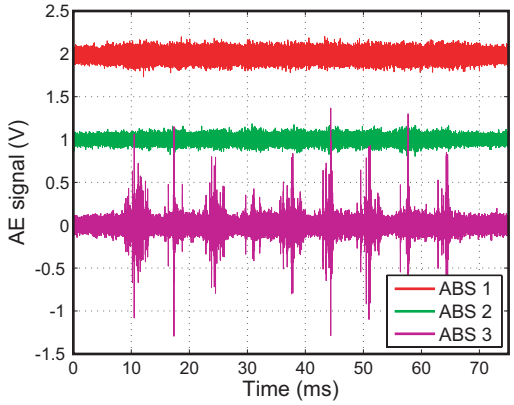

Figure 6.2: Touchdown signature for the three different ABS designs

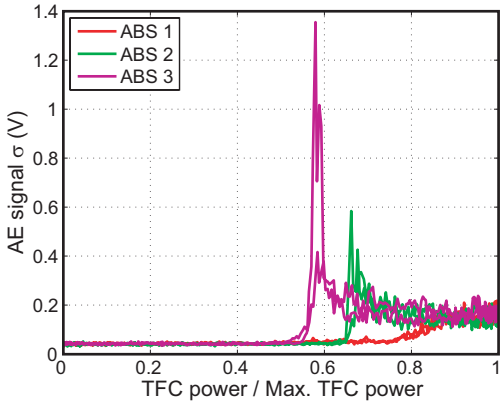

Figure 6.3: Contact behavior in overpush for the three different ABS designs

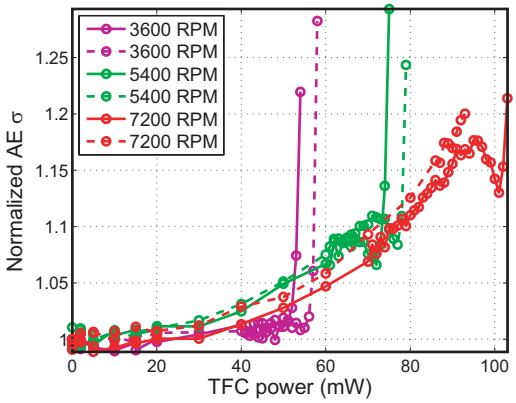

Figure 6.4: Touchdown plots for ABS-2 at different disk RPM

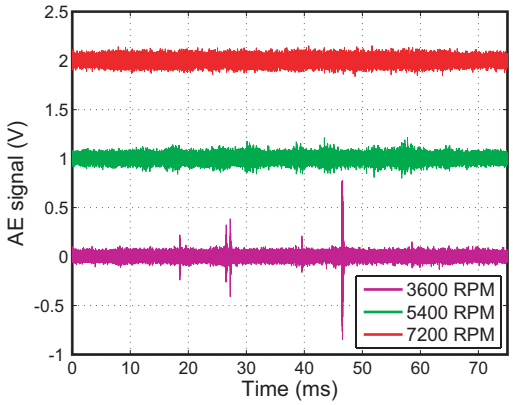

Figure 6.5: Touchdown signature for ABS-2 at different disk RPM

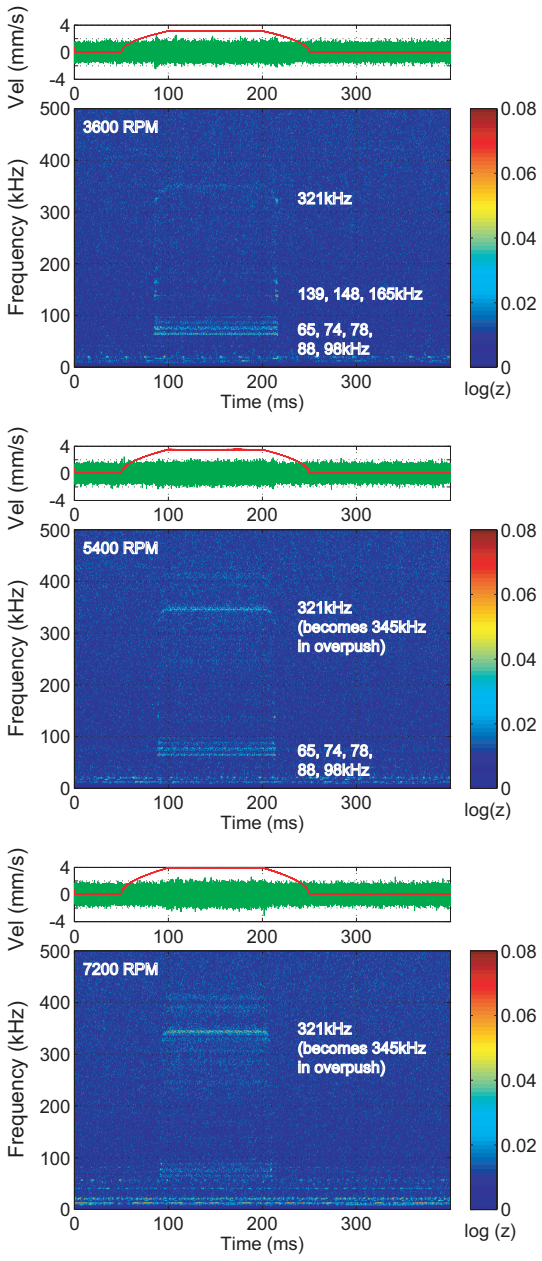

Figure 6.6: Vertical velocity time history and the JFT of vertical velocity for ABS-2 at different disk RPM

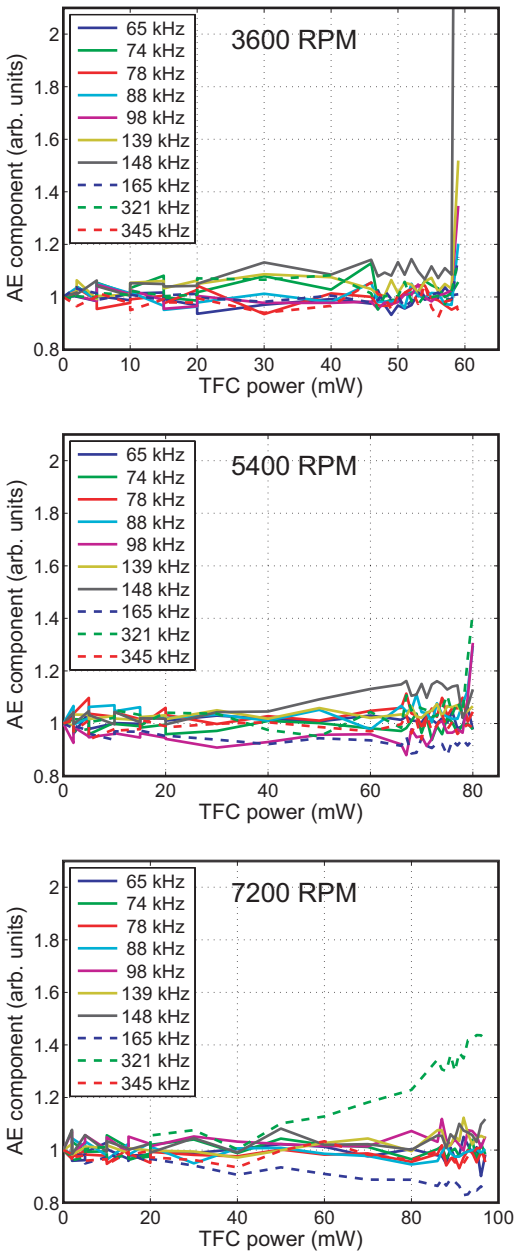

Figure 6.7: AE signal components in the touchdown plot for ABS-2 at different disk RPM

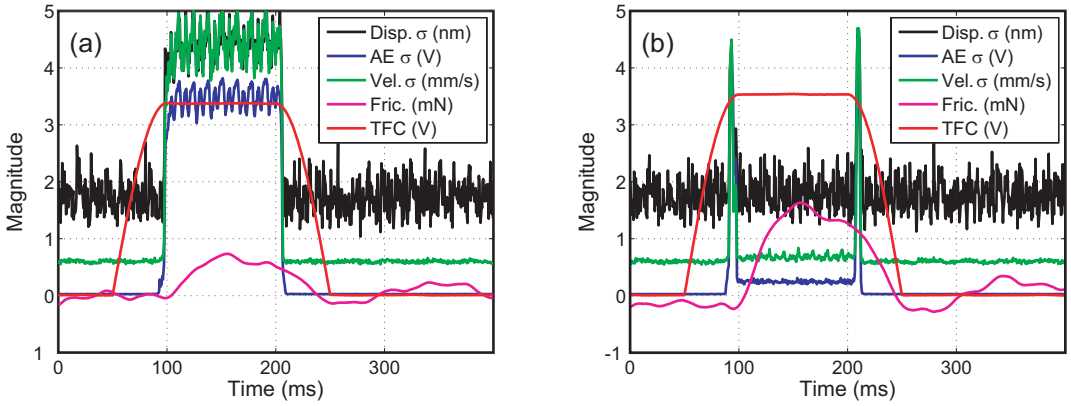

Figure 6.8: Time history of TFC power, vertical displacement, vertical velocity, AE signal and friction (a) $10mW$ overpush (b) $20mW$ overpush

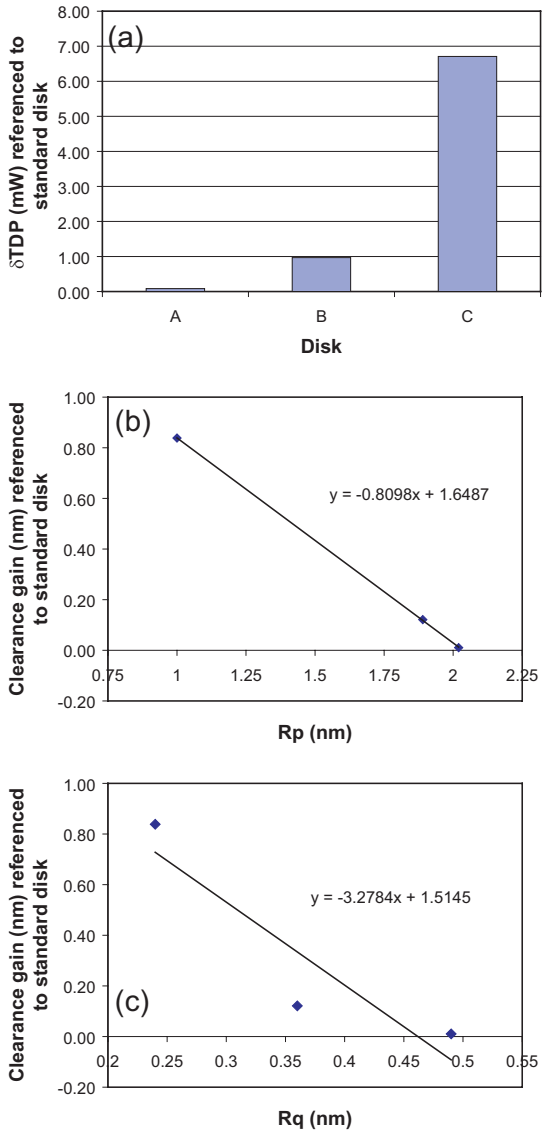

Figure 6.9: Effect of disk roughness on clearance

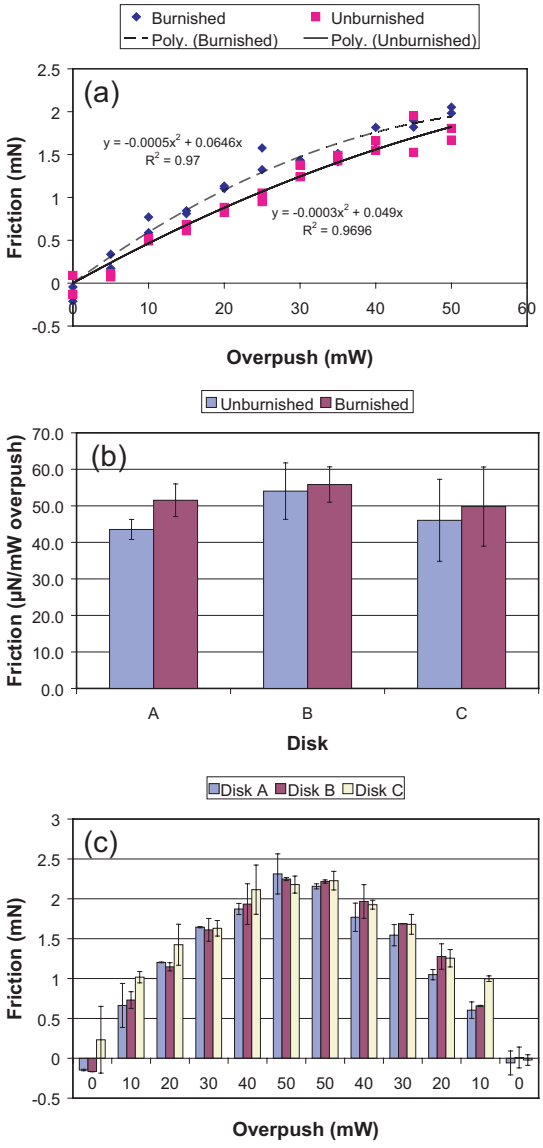

Figure 6.10: Effect of disk roughness on friction

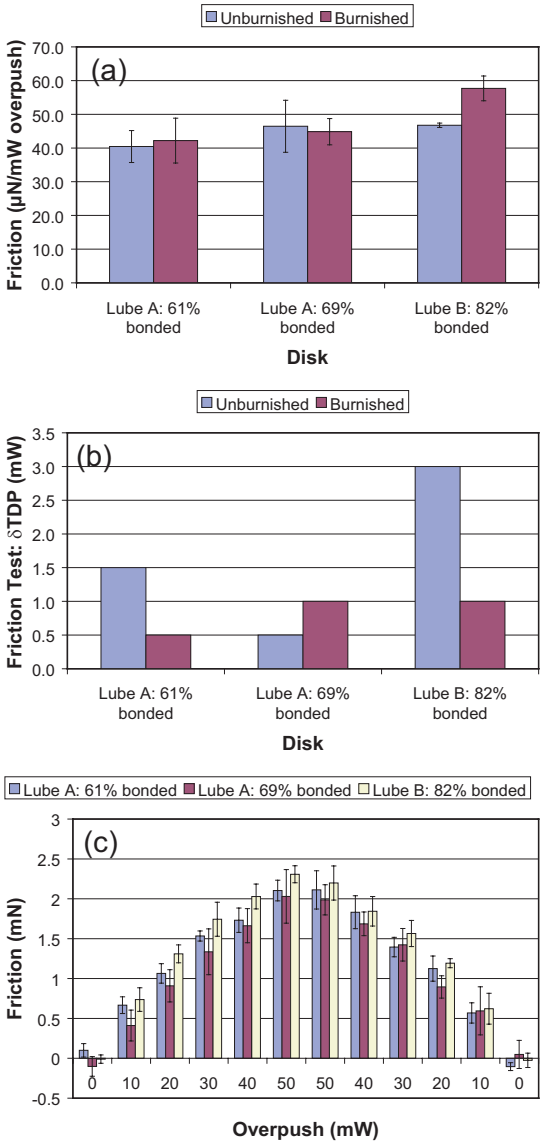

Figure 6.11: Effect of lubricant parameters on friction and slider burnishing

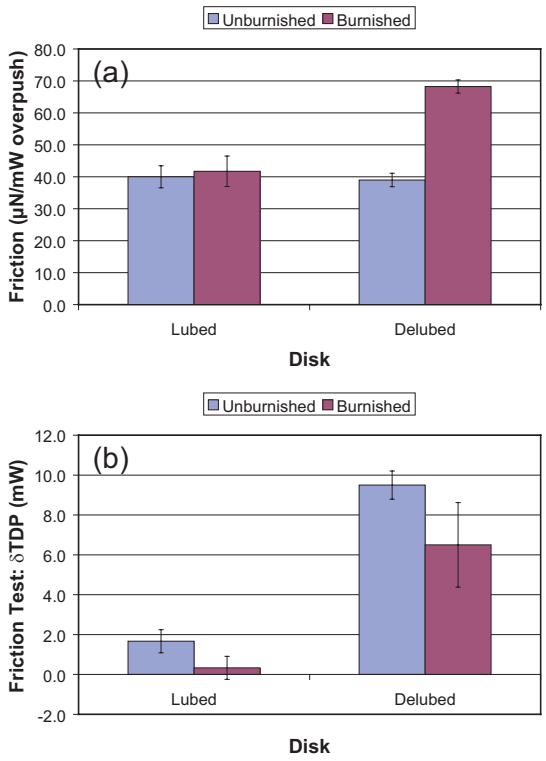

Figure 6.12: Effect of mobile lubricant on friction and slider burnishing

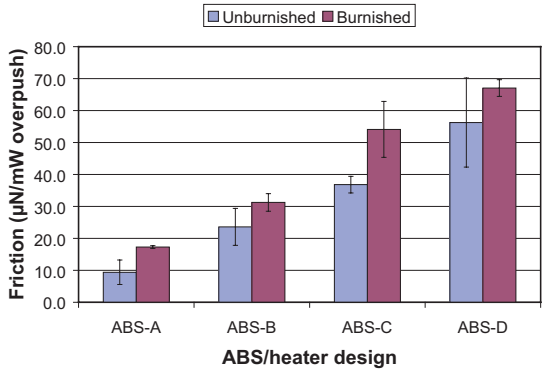

Figure 6.13: Effect of TFC efficiency (ABS/heater design) on friction

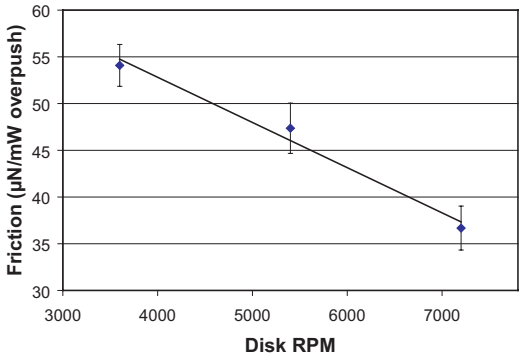

Figure 6.14: Effect of disk RPM on friction for ABS-2

Chapter 7

Lubricant Distribution at the Head-Disk Interface of Thermal Fly-height Control Sliders

The previous chapters of this dissertation focused on understanding the dynamics of thermal fly-eight control (TFC) sliders actuated into contact with the disk/lubricant. This chapter (and the next) focus on understanding the disk lubricant distribution and slider-lubricant interactions during TFC induced contact.

Interactions between the slider and the disk lubricant have become increasingly important as the head-disk clearance shrinks to the subnanometer regime. Abundant literature exists documenting the detrimental effects of slider-lubricant interactions on slider dynamics and on head-disk interface (HDI) performance. The coupled effect of slider dynamics and lubricant modulation on each other (washboarding effect) is a serious concern for HDI reliability [Dai et al. 2004a]. Even for a noncontacting interface, lubricant transfer from the disk to the slider occurs by evaporation/condensation mechanisms and is enhanced by flow and accumulation of the lubricant on the slider's trailing end [Marchon et al. 2003]. Lubricant drop-off from the slider's trailing end to the disk has been experimentally observed and is known to cause magnetic spacing changes that are detrimental to read-write performance [Moseley and Bogy 2009, Pit et al. 2003]. Apparent spacing increases due to lubricant accumulation on the slider's trailing end and the associated 'waterfall effect' pose a challenge to the reliable measurement and calibration of the head-disk clearance in a working drive [Marchon et al. 2009, Mate et al. 2010].

Future magnetic storage density targets necessitate clearances in the neighborhood of $0.25nm$ which essentially falls in the realm of recording with intermittent and possibly continuous contact with the lubricant and disk media. Slider-lubricant contact is expected to significantly alter and enhance the slider-lubricant interactions by promoting meniscus formation and direct lubricant transfer between the disk and the slider [Ambekar and Bogy 2005, 2006]. Recently, the feasibility of recording in a lubricant-surfing regime has been explored [Liu et al. 2009]. Interesting experimental observations have been reported for slider dynamics in the lubricant-contact regime [Vangipuram Canchi and Bogy 2010] and have been partially explained using nonlinear systems theory [Vangipuram Canchi and Bogy 2011a]. However, the challenge of fully understanding slider-lubricant interactions in the presence of

contact still remains and forms an important basis for developing proper design strategies to ensure the long term reliability of a contacting HDI.

Considering the above motivation, this work focuses on experiments to study lubricant distribution and slider-lubricant interactions using TFC actuation to bring the slider's read-write head into proximity and contact with the disk lubricant. Contact between the thermal protrusion and the disk lubricant causes a thickness modulation (rippling) together with lubricant depletion that grows with contact duration. Slider dynamics and lubricant rippling evolve quickly in the first few revolutions of contact and rippling frequencies are strongly correlated with the slider's air bearing frequencies. Peculiar cases where suppressed 'stable' slider dynamics occur for TFC heater power beyond the touchdown power (TDP) correspond to negligible lubricant rippling and this condition may be sustained for fairly long durations in some tests. Experiments with different lubricant types (ZTMD, Z-tetraol+A20H, Z-dol+A20H) and different lubricant thicknesses show that a larger depletion is observed for the thicker lubricant of each type at a given TFC heater power. Lubricants with a lower bonded fraction show shorter recovery times after the slider is unloaded. The current experiments indicate that Z-dol+A20H (30% bonded) lubricant recovers in a time scale of a few hours, while Z-tetraol+A20H (60% bonded) lubricant of comparable thickness takes a few days, and ZTMD (75% bonded) takes weeks to fully recover.

7.1 Experiments

The experiments are conducted on a spin stand equipped with an optical surface analyzer (OSA) for *in-situ* monitoring of the lubricant surface. This set-up allows the observation of the change in the lubricant surface as the slider continues to fly over the test track, and it permits the understanding of how the lubricant recovers/reflows after the slider is unloaded from the test track. The slider's vertical motion is simultaneously monitored using a laser doppler vibrometer (LDV), which is used for correlation with lubricant distribution results.

Previous investigations have shown peculiar slider dynamics when the heater power is increased beyond the TDP. Specifically, the suppression of the intensity of acoustic emission (AE) detected contact and the magnitude of slider motions in all directions (vertical, down-track and off-track) has been reported [Vangipuram Canchi and Bogy 2010] and shown to be attributable to nonlinearities at the HDI [Vangipuram Canchi and Bogy 2011a]. The correlation of lubricant distribution with the slider dynamics in this regime is important and is reported in this chapter. The results for cases when the heater power is reduced below the TDP (backoff), is at the TDP and is above the TDP (overpush) are compared to understand the interplay between slider dynamics and lubricant distribution.

The disks used in this work are coated with different lubricants: Z-dol+A20H (30% bonded) with thickness 9.5Å and 13.7Å, Z-tetraol+A20H (60% bonded) with thickness 9.5Å and 14.5Å, and ZTMD (> 75% bonded) with thickness 10.5Å, 12Å and 14Å. The 'pemto' slider air bearing surface (ABS) used in this work is shown in Fig 7.1a. First, the TDP is determined on the test track using an automated program that uses the AE signal as feedback when the TFC heater is supplied a square pulse with increasing power (in milliwatt steps) and lasting one disk revolution. The power corresponding to a rise in AE signal standard deviation above 50% of the baseline is taken as TDP, and a representative plot is shown in

Fig 7.1b.

The test procedure is as follows: after calibrating the TDP on the test track, the slider is flown with the TFC heater turned 'on' over only one half of the track every disk revolution by synchronizing the heater power input program to the spindle index. By controlling the heater power to be below the TDP (for backoff), at TDP or above the TDP (for overpush), this testing protocol gives good control to observe and compare changes to the lubricant without any thermal protrusion (part of the track with heater turned 'off') and with specified thermal protrusion (part of the track with heater turned 'on'). Additional information on the lubricant behavior in the region where the thermal protrusion comes into contact and leaves contact with the disk lubricant may also be obtained using this method. Fig 7.2 shows a representative OSA scan of the disk lubricant before and after a test with many cycles of overpush power on one half of the test track. The slider flies over the disk track from left to right as indicated by the direction of arrows. A lighter color on the OSA scan implies lubricant depletion, and a darker color implies lubricant accumulation. While there is negligible change in the lubricant surface when there is no thermal protrusion (heater power 'off'), significant change in the lubricant is observed where the thermal protrusion causes lubricant/disk contact.

7.2 Results and Discussion

7.2.1 Correlation of lubricant distribution and slider dynamics

In order to correlate the lubricant distribution and slider dynamics a test is performed to monitor the change in the lubricant surface after 50 synchronized TFC heater pulses (i.e. contacting one half of the disk track 50 times). The OSA scans before and after this test give the cumulative change in the lubricant thickness and the LDV data is used to obtain information on how the slider dynamics changes with contact between the first and the 50^{th} pulse.

Fig 7.3a shows the lubricant profile for tests on a disk with ZTMD lubricant of 14Å thickness with TFC heater power of TDP$-5mW$ (i.e. $5mW$ backoff), TDP, TDP+$10mW$ (i.e. $10mW$ overpush) and TDP+$20mW$ (i.e. $20mW$ overpush). Significant lubricant rippling occurs in this case at TDP and in overpush conditions. Fig 7.3b shows the frequency content of the lubricant rippling profile plotted in Fig 7.3a together with the slider's vertical velocity spectrum for the first and 50^{th} contact pulse at each power level. Frequencies above $50kHz$ (corresponding to the air bearing frequencies) are of primary importance in this work.

From Fig 7.3b, a few important observations can be made. First, the slider dynamics evolves quickly and is different in the 50^{th} pulse compared to the first pulse. This observation is very evident for the overpush cases in this figure, and it is marked by the appearance of a strong peak at $265kHz$ in the 50^{th} pulse. Second, the slider dynamics at TDP is different from the slider dynamics in overpush as indicated by the location of the frequency peaks at $125kHz$ and $265kHz$, respectively, consistent with previously published literature showing the slider dynamics to be strongly dependent on the degree of contact [Shimizu et al. 2010, Vangipuram Canchi and Bogy 2010]. Third, the lubricant spectrum shows no specific peaks at backoff, but significant peaks occur at TDP and in overpush. Lubricant spectrum peaks, when they appear, correspond well with the frequency peaks in the slider's vertical velocity

spectrum (of the 50^{th} pulse) verifying good correlation between the two. It is noted that at TDP several peaks appear in the lubricant spectrum that are below and above 125kHz. Although not evident in the slider's velocity spectrum in this case, such additional peaks have also been observed in the slider's velocity spectrum in other cases, and have been attributed to subharmonics, superharmonics and fractional harmonics of the nonlinear air bearing system [Vangipuram Canchi and Bogy 2011a].

Slider dynamics and lubricant rippling are therefore well correlated with the dominant lubricant rippling frequencies generally matching the slider's vertical bouncing frequencies. It is concluded that lubricant and slider interactions evolve very quickly in the first few revolutions of contact through an interplay similar to the 'washboarding effect' reported in the literature [Dai et al. 2004a].

The more interesting and peculiar case occurs when the slider dynamics and AE detected contact are suppressed in the overpush condition. The lubricant surface changes that occurred for such a case are shown in Fig 7.4a from the experimental results using a disk with ZTMD lubricant of 12Å thickness. While there is stronger lubricant rippling at TDP, the lubricant rippling in overpush is negligible in comparison. The spectrum of the lubricant profile shown in Fig 7.4b reveals the same information: no peaks are present for the TDP+$10mW$ and TDP+$20mW$ cases compared to peaks at $125kHz$ and $250kHz$ (second harmonic) for the TDP case. It is noted that the slider's vertical velocity spectrum also shows the same trend, with no frequency peaks evident in overpush compared to the strong peak at $125kHz$ at the TDP. These results once again show that slider dynamics and lubricant rippling are well correlated. Specifically, the absence of slider dynamics ('stable' condition) in overpush corresponds with the absence of lubricant rippling, and this important observation has not been reported previously in the literature. Although not presented here, such suppression is also observed on media coated with lubricants of other types and thickness (eg. Z-tetraol) and appears to be affected more by the slider (ABS and heater) designs.

For this 'stable' case, where the slider dynamics and lubricant rippling are both absent in overpush, the test is extended to understand the effect of continuing the contact pulses for a longer duration. Fig 7.5a shows the lubricant scans after applying TFC pulses on one half of the track for 1 minute ($\approx$ 3600 pulses) and Fig 7.5b shows the associated spectrum of slider dynamics and lubricant rippling. It is seen from Fig 7.5a that at TDP, the change in the lubricant profile is higher (with stronger evidence of lubricant rippling). The cases with overpush show lesser lubricant change, except at the angular locations marking the onset and the end of contact. Zoomed images of these contact onset and contact end angular locations are shown in Fig 7.6a and Fig 7.6b, respectively. From Fig 7.6a, a region of lubricant accumulation at the onset of contact is observed suggesting the transfer of lubricant from the trailing end of the slider to the disk, which can be explained as follows: the increasing thermal protrusion causes a decreasing head-disk clearance allowing the bridging of lubricant accumulated on the slider's trailing end with the disk, thus facilitating lubricant transfer/drop-off onto the disk. Immediately following this lubricant accumulation region is a strong depletion zone with superposed lubricant rippling. For tests with heater power at TDP, this rippling signature continues for as long as the heater is turned 'on', but for the overpush conditions of TDP+$10mW$ and TDP+$20mW$, the lubricant rippling ceases, leading to a region of negligible lubricant depletion or rippling. Although not shown here, it was possible to sustain such a condition of suppressed AE signal, suppressed slider dynamics

and negligible lubricant change for as long as 20 minutes in some tests.

While it may be speculated that this zone that shows negligible lubricant change and 'stable' slider dynamics corresponds to smooth sliding over the lubricant surface (lubricant surfing regime), conclusive evidence and understanding of the slider-lubricant interactions in this interesting zone is still lacking and requires further research. Other possibilities include contact loss for short durations because the slider bounces off and attains a stable flying state without any lubricant contact. The durability of the interface while operating in this interesting zone also remains an open topic for investigation.

Another peculiar observation in these overpush tests is the presence of a strong depletion zone at the end of contact (Fig 7.6b) suggesting lubricant pick-up onto the slider as the thermal protrusion retracts when the heater is turned 'off'.

This effort to understand lubricant and slider dynamics in contact reveals that the lubricant rippling and slider dynamics frequencies are very well correlated. In particular the peculiar 'stable' condition with negligible slider dynamics in overpush corresponds with negligible lubricant ripping or negligible change in the lubricant surface. This 'stable' condition may be sustained for long durations in some tests, and is presumed to depend on the lubricant as well as the slider's design. The typical lubricant signature for overpush tests shows lubricant accumulation at the onset of contact, followed by a region of either strong rippling with associated slider dynamics or negligible lubricant change with 'stable' slider dynamics, followed by a strong depletion signature at the end of contact.

7.2.2 Lubricant profile evolution under the TFC protrusion

The lubricant profile evolution under the thermal protrusion as well as the subsequent relaxation/recovery of the displaced lubricant is performed using the following post processing steps on the OSA images. The averaged lubricant profile under the thermal protrusion is obtained over the track cross-section as shown in the representative plot Fig 7.7, and it typically shows a region of lubricant depletion (groove) under the TFC protrusion and occasionally a region of lubricant accumulation (ridge) on the side(s) of the TFC protrusion.

The net-depletion (defined as the volume of the groove less the volume of the ridge) generally increases with the duration of contact. Least depletion occurs at back-off powers and depletion is enhanced in overpush because slider-lubricant contact plays a more significant role in lubricant distribution than the high pressure and shear induced lubricant redistribution at back-off powers.

A comparison of Fig 7.8a and Fig 7.8b for ZTMD lubricant with thickness of 10.5Å and 14Å respectively, shows that at a given TFC (overpush) power, the thicker lubricant case has a greater depletion tendency. A similar result is obtained for Z-tetraol+A20H (Fig 7.9) and Z-dol+A20H (Fig 7.10) lubricants as well. It is expected that depletion increases with increasing heater power (i.e for decreasing clearance or increasing interference), but the trend may not always be obvious because slider-lubricant interaction causes complex phenomena such as occasional lubricant drop-off from the slider to the disk and lubricant changes due to occasional slider instability/bouncing periods, and these events potentially introduce substantial test-to-test variations in the results.

An important observation is that the net-depletion in overpush appears to be the least for the 'stable' case when slider dynamics or lubricant rippling is absent. As seen in Fig 7.11,

the net-depletion for the 'stable' overpush case is significantly lower than the other two cases with 'unstable' behavior at overpush power, and the former in fact compares closely to the case with $5mW$ back-off.

Lubricant recovery refers to the ability of the lubricant to recover back to a 'flat' profile (from those shown in Fig 7.7) after the slider is unloaded. This important metric is a measure of how quickly any contact related damage is 'healed' to ensure prolonged HDI reliability. In this work, the standard deviation (σ) of the profile shown in Fig 7.7 is used as a measure of lubricant surface 'nonflatness' ($\sigma = 0$ corresponds to a perfectly flat lubricant surface). After normalizing with the value of σ at one minute after slider unloading, the plots for lubricant recovery to flatness are shown for Z-dol+A20H lubricant and Z-tetraol+A20H lubricant in Fig 7.12. It is seen that after normalization, the dependence of the lubricant recovery curves on the actual heater power is minimal. So the lubricant recovery time obtained with $20mW$ overpush is similar to that with any other overpush power value. Good repeatability is observed between tests conducted on different days giving confidence in this method.

Using this method, the recovery times for the different lubricants used in this work are plotted in Fig 7.13. Lubricant recovery time is strongly influenced by the mobility of the lubricant molecules. In the current experiments, Z-dol+A20H with higher mobile fraction (30% bonded fraction) recovered much quicker than Z-tetraol+A20H with lower mobile fraction (60% bonded), which in turn recovers quicker than ZTMD ($> 75\%$ bonded fraction). Based on the extrapolated data trends shown in Fig 7.13 it is concluded that the recovery time for the Z-dol based lubricant is on the order of a few hours, that for the Z-tetraol based lubricant is a few days, and that for ZTMD is measured in weeks. It is noted from the normalized plots for lubricant recovery, the thinner lubricant case appears to have a faster recovery time. This result is partly an artifact of normalization: the case with thinner lubricant starts with a 'flatter' lubricant profile (at one minute after unload), and therefore it appears to recover faster than the case with the thicker lubricant.

7.3 Conclusion

Investigations to better understand the effect of low clearances and contact on slider dynamics, lubricant distribution and slider-lubricant interactions are important in order to develop design strategies to meet overall HDI reliability goals in future hard-disk drives. The experimental results in this chapter reveal that under contact and overpush conditions slider dynamics and lubricant surface rippling are strongly correlated. In particular, the favorable condition with 'stable' slider dynamics in overpush is also associated with negligible change in the lubricant surface. The mechanism of lubricant transfer from the slider to the disk at the onset of contact as well as strong depletion at the end of contact is demonstrated. Results for lubricant distribution with different lubricant types and thicknesses reveal that the net-depletion is higher for thicker lubricants for all types. Extrapolated lubricant recovery times for the Z-dol based lubricant is shorter (hours) compared to the Z-tetraol based lubricant (days) and the ZTMD lubricant (weeks). Research to empirically relate lubricant evolution (net-depletion) and recovery times with lubricant properties is proposed as future work on this topic.

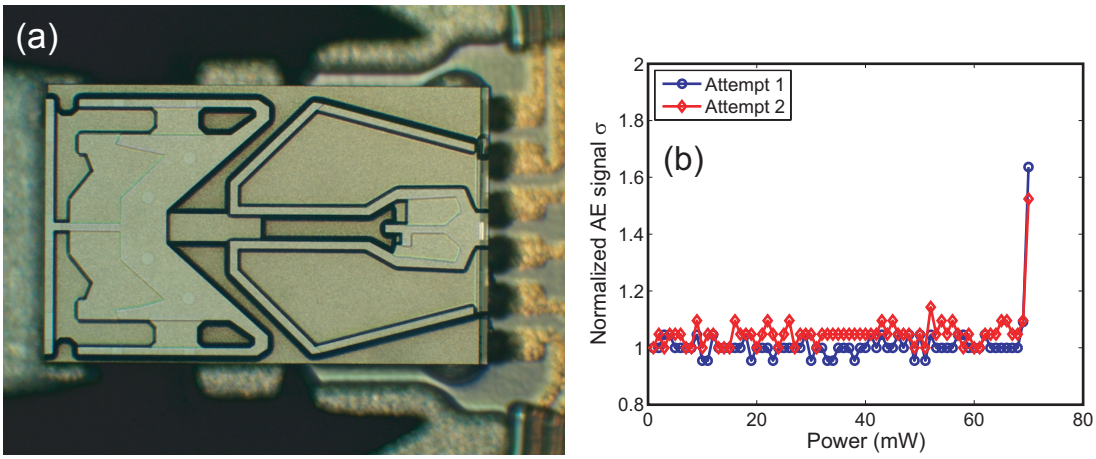

Figure 7.1: (a) Slider ABS design (b) Representative touchdown detection plot

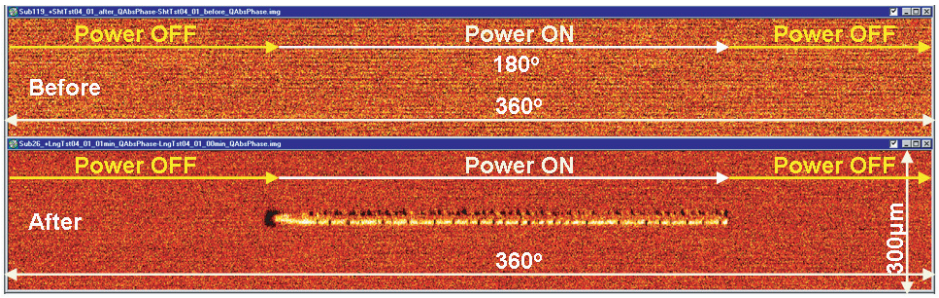

Figure 7.2: Representative OSA scan before and after a test with the heater turned 'on' over one half of the test track

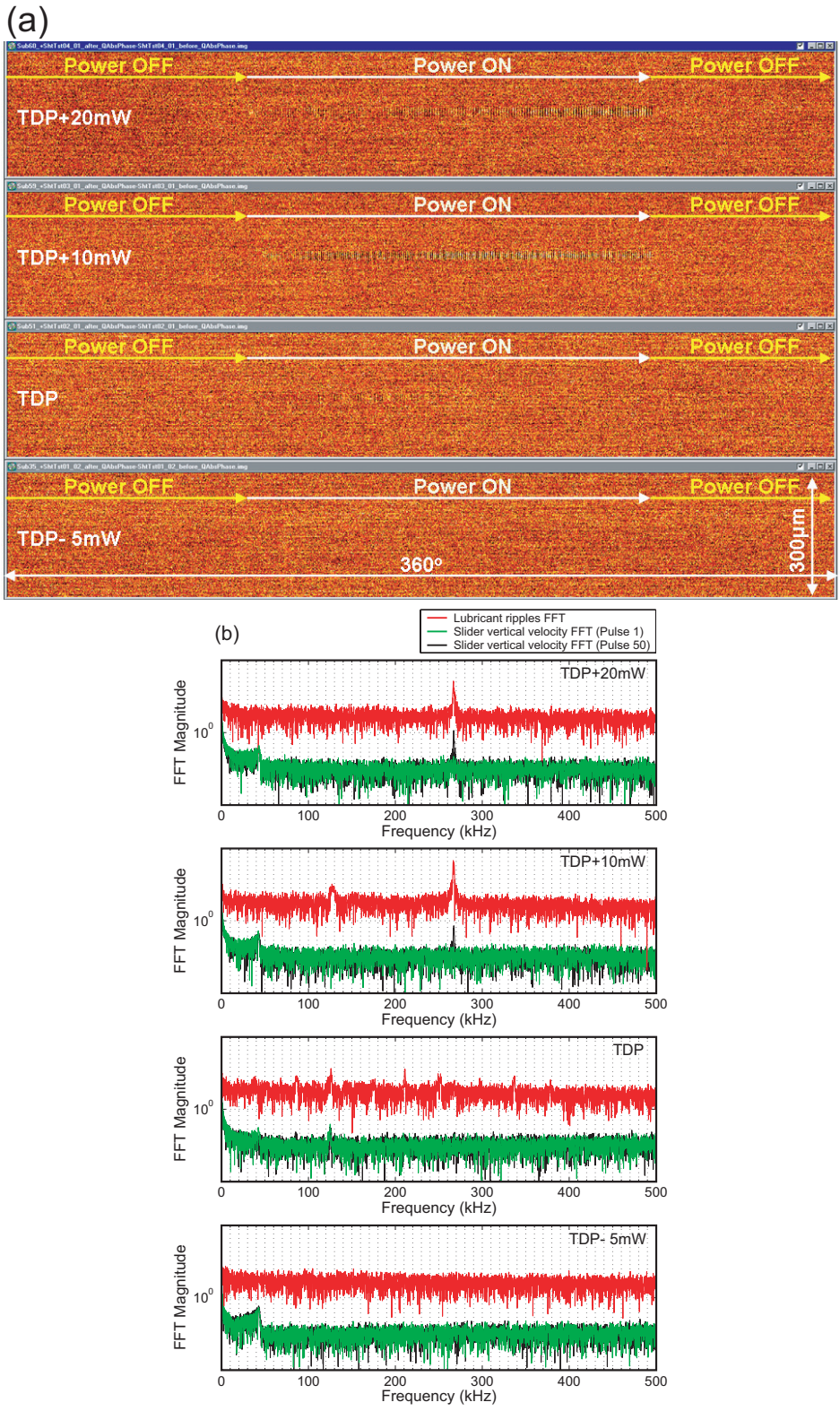

Figure 7.3: Case with strong lubricant rippling and slider dynamics at TDP and in overpush (a) OSA scans showing lubricant surface change after 50 contact pulses for tests with different heater powers (b) Spectrum of the lubricant profile under the thermal protrusion and spectrum of the slider's vertical velocity for the first and 50^{th} contact pulse

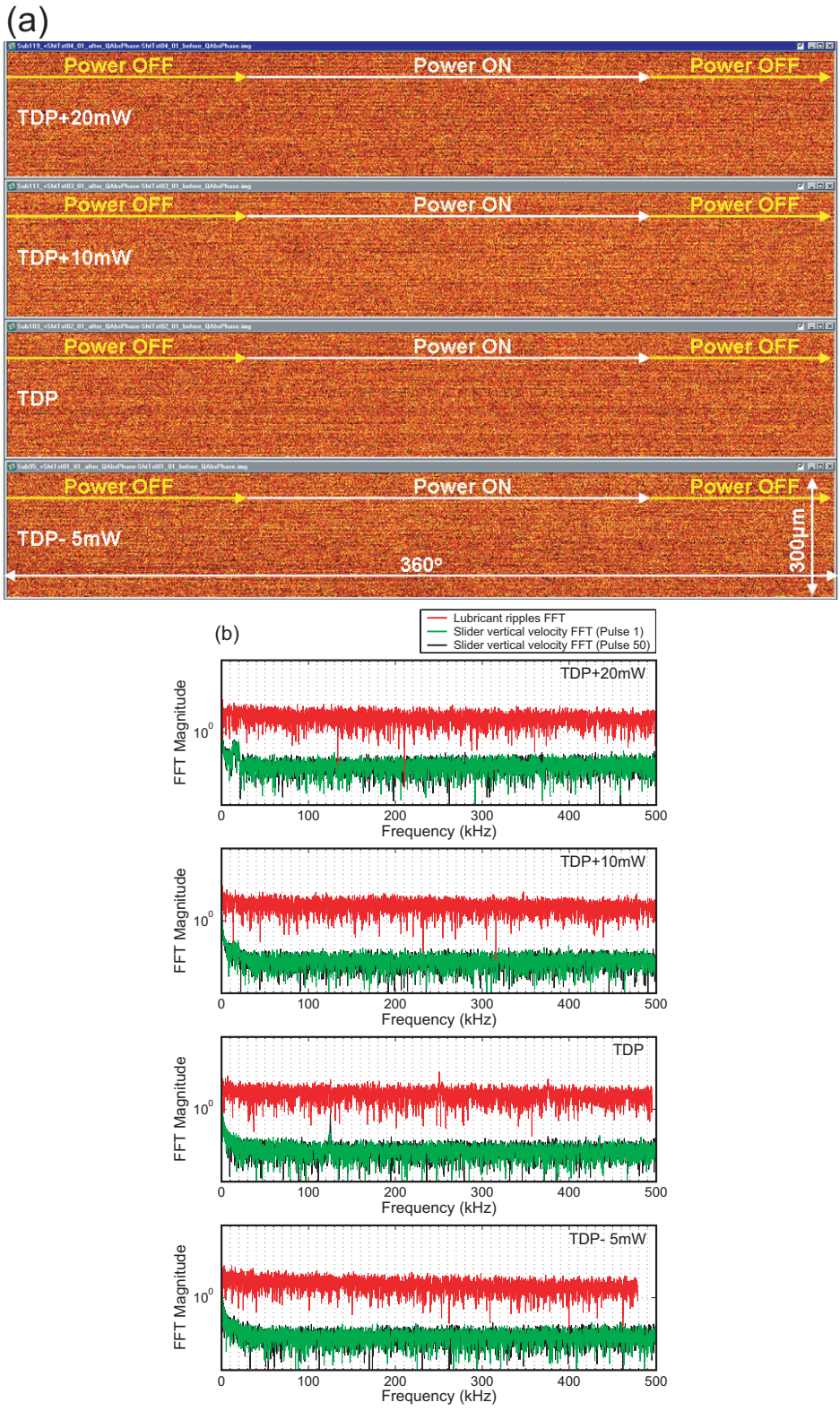

Figure 7.4: Case with negligible lubricant rippling and slider dynamics in overpush (a) OSA scans showing lubricant surface change after 50 contact pulses for tests with different heater powers (b) Spectrum of the lubricant profile under the thermal protrusion and spectrum of the slider's vertical velocity for the first and 50^{th} contact pulse

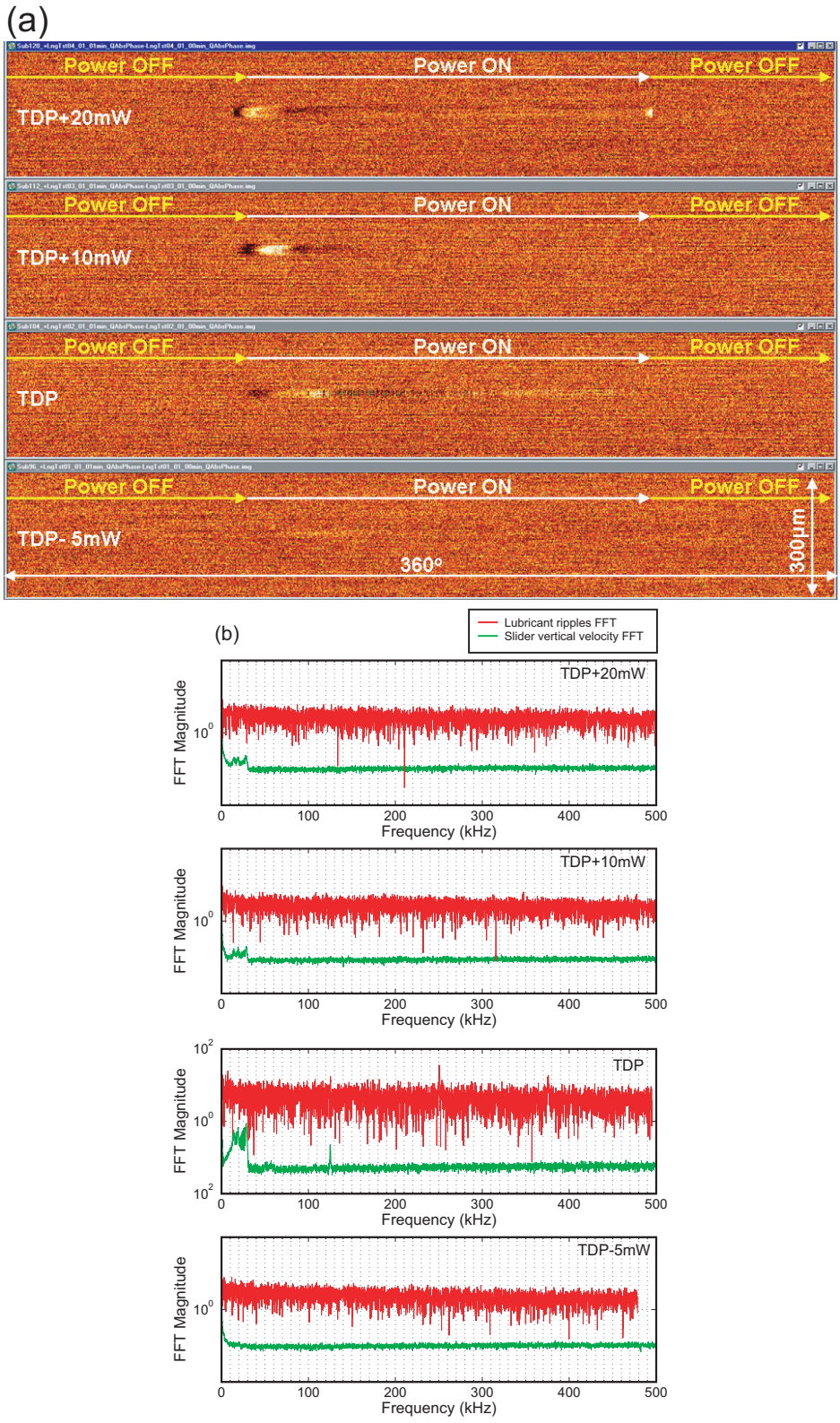

Figure 7.5: Case with negligible lubricant rippling and slider dynamics in overpush (a) OSA scans showing lubricant surface change after 1 minute for tests with different heater powers (b) Spectrum of the lubricant profile under the thermal protrusion and spectrum of the slider's vertical velocity

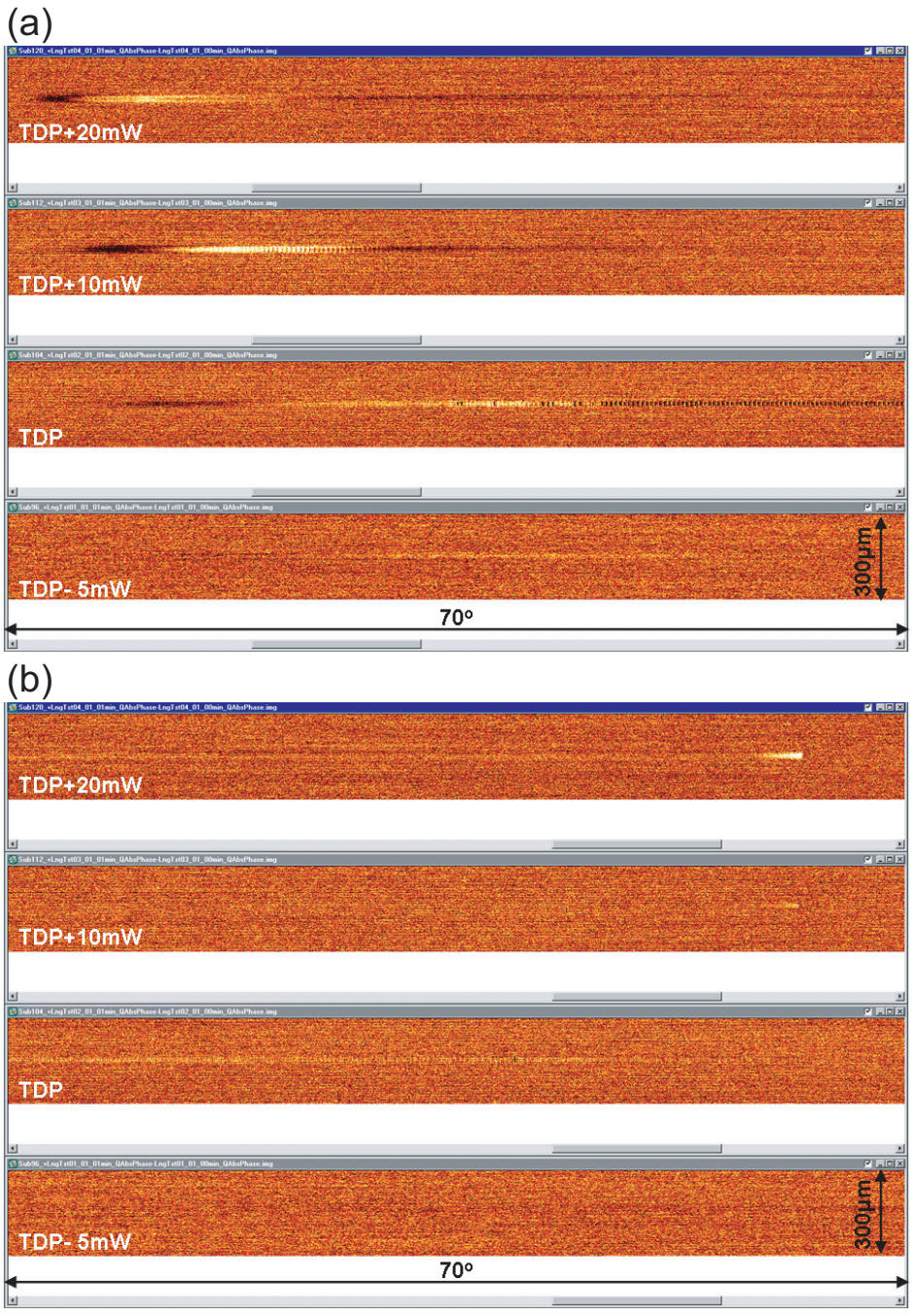

Figure 7.6: Zoom image of OSA scans shown in Fig 7.5. (a) Contact onset region (b) Contact end region

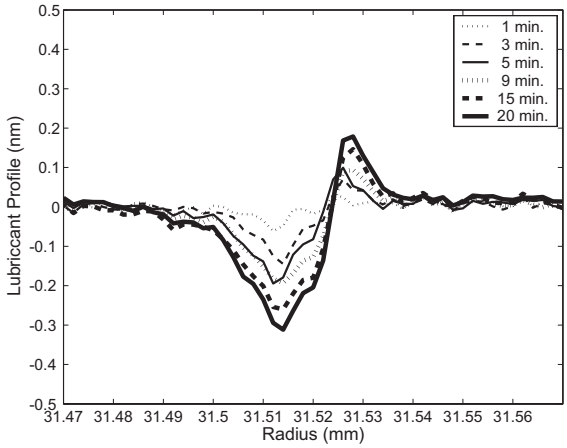

Figure 7.7: Representative lubricant profile cross-section of the test track during a contact test

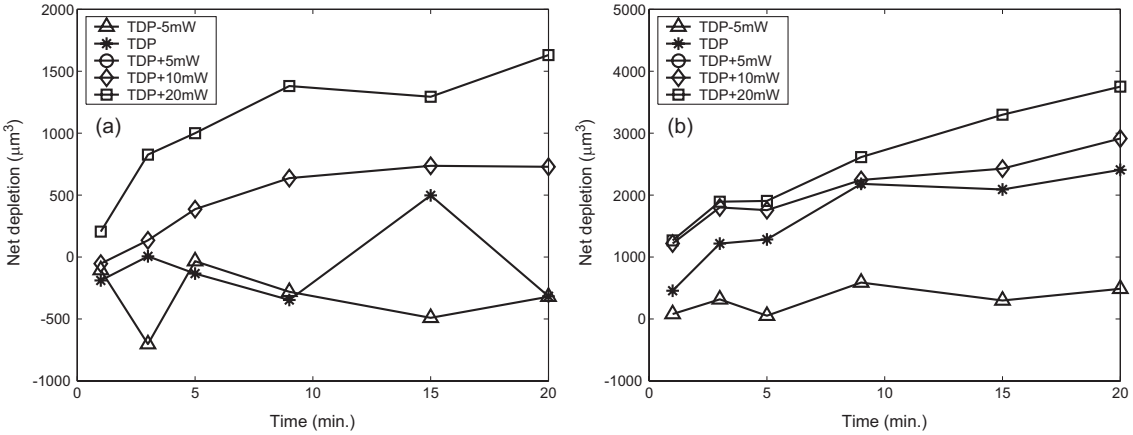

Figure 7.8: Net-depletion with time (a) ZTMD 10.5Å (b) ZTMD 14Å

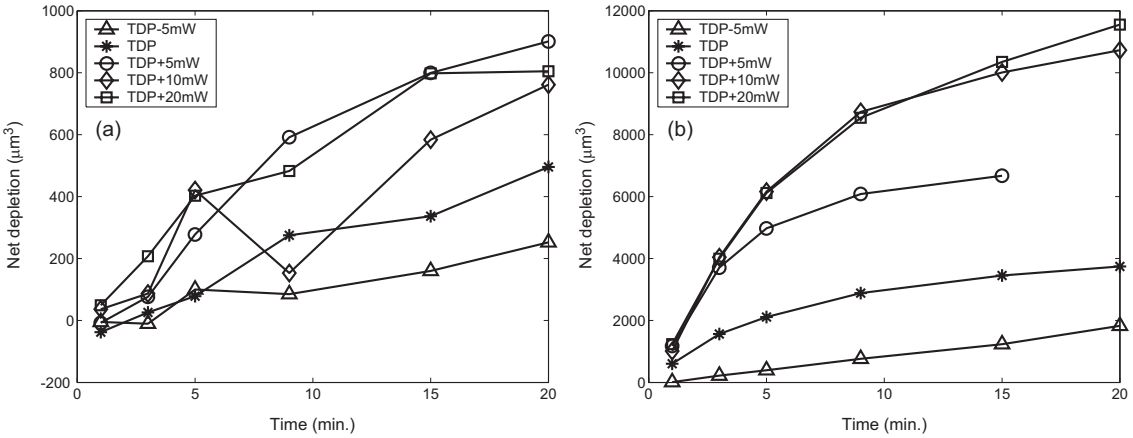

Figure 7.9: Net-depletion with time (a) Z-tetraol+A20H 9.5Å (b) Z-tetraol+A20H 14.5Å

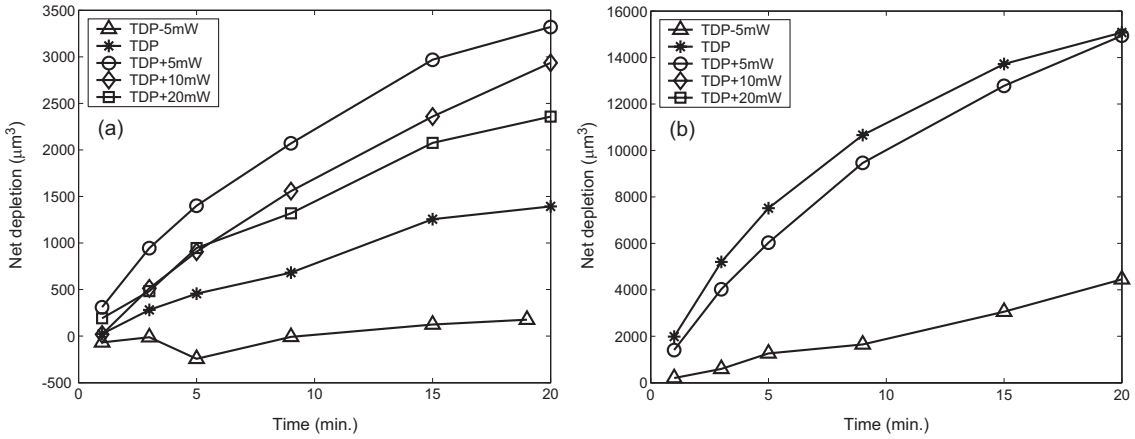

Figure 7.10: Net-depletion with time (a) Z-dol+A20H 9.6Å (b) Z-dol+A20H 13.7Å

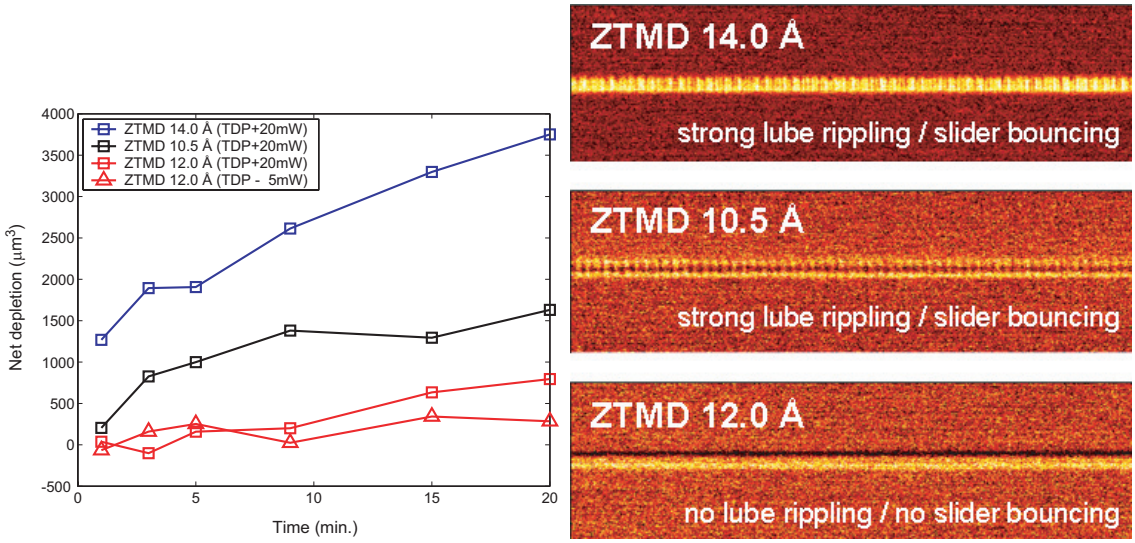

Figure 7.11: Net-depletion vs. slider dynamics and lubricant rippling signature

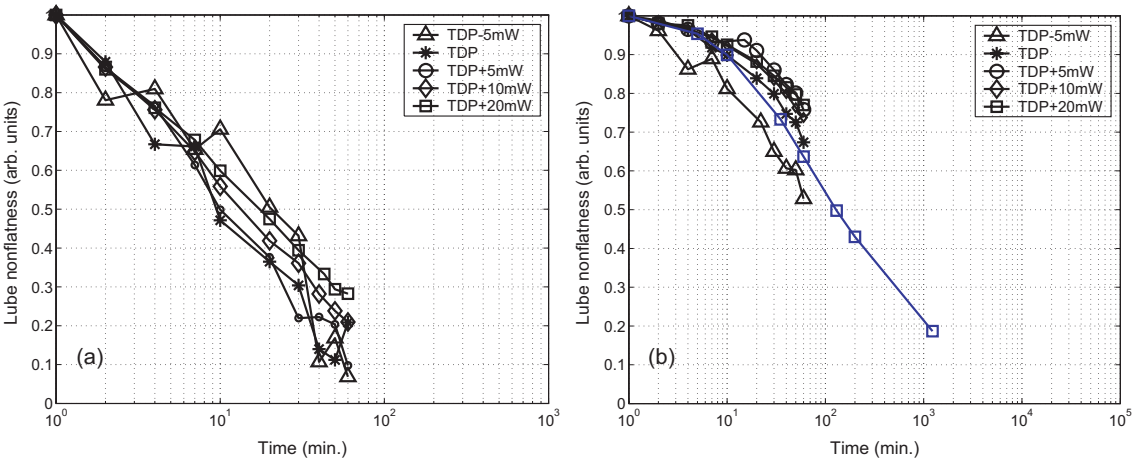

Figure 7.12: Lubricant recovery to flatness with time (a) Z-dol+A20H 9.6Å (b) Z-tetraol+A20H 14.5Å, blue curve represents test conducted on different day

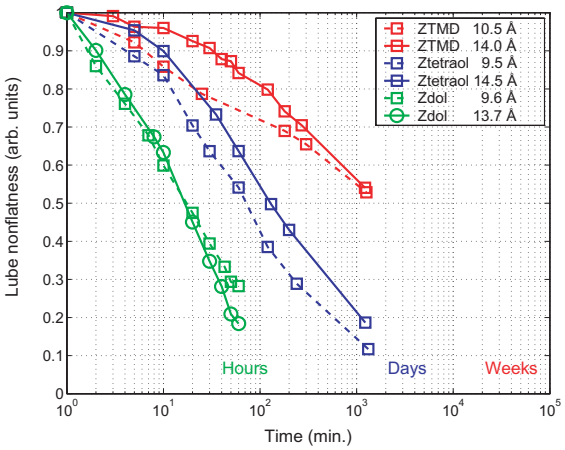

Figure 7.13: Lubricant recovery plots for different lubricants

Chapter 8

Slider-Lubricant Interactions and Lubricant Transfer at the Head-Disk Interface of Thermal Fly-height Control Sliders

The effect of thermal fly-height control (TFC) actuation induced contact on the disk lubricant distribution and recovery is discussed in Chapter 7 together with results on slider-lubricant interactions and their correlation to slider dynamics. The behavior of the disk lubricant is further investigated in this chapter through carefully controlled tests in which TFC sliders are actuated to proximity (i.e backoff) and into contact (i.e. overpush) on one specific half of the disk per rotation by synchronization with the spindle index. Observations of the lubricant distribution in the contact tests (i.e overpush) reveal an accumulation of lubricant on the disk near the onset of contact suggesting a migration of lubricant from the slider to the disk as the slider approaches the disk. Experiments also reveal a similar deposition of lubricant even in the absence of contact for backoff tests. Furthermore, light contact results in significant lubricant rippling and depletion with associated slider dynamics. The lubricant rippling frequencies correlate well with the slider vibration frequencies. Interestingly, strong overpush may lead to stable slider dynamics (for certain air bearing designs) that is also associated with noticeably lower lubricant distribution (compared to light contact case) and the greatest lubricant changes are observed only at the angular locations marking the onset and the end of contact. The complex nature of slider-lubricant interactions under near-contact and contact conditions revealed in these experiments highlights the need for further studies on the topic to help in the design and development of a HDI for recording systems of the future.

8.1 Experiments

The experimental spin stand set-up consists of an *in-situ* optical surface analyzer (OSA) to monitor the disk lubricant changes as the slider flies over the test track. Slider contact with the disk lubricant is monitored using an acoustic emission (AE) sensor and the slider dynamics is simultaneously measured using a laser doppler vibrometer (LDV). The slider

used for these experiments are of the 'pemto' type and the air bearing surface (ABS) is shown in Fig 8.1. The TFC heater is powered by amplified inputs from a data acquision board that is controlled using a custom written Labview program. This set-up allows for a versatile range of experiments and offers good power resolution. The research disks used in this work are coated with perfluoropolyether lubricant of similar thickness: ZTMD 12Å and Z-tetraol 12.5Å. The slider is loaded onto the rotating disk and moved to the desired test track. The touchdown power (TDP) is determined using an automated Labview program. The TFC heater is supplied a square pulse with increasing power (in steps of one milliwatt) that lasts one disk revolution. The AE signal standard deviation (σ) is monitored during the TFC pulse duration. The power corresponding to a sudden jump in the σ above a fixed threshold (set to 50%) above the baseline value (obtained when the slider is flying passively with zero heater power) is recorded as the TDP.

After determining the TDP, a controlled test is conducted by turning the TFC power 'on' over only one specific half of the disk by synchronizing the TFC power supply program with the disk spindle index Fig 8.2. In order to study the lubricant changes under different conditions, the peak power of the TFC pulse is set to $TDP - 5mW$ and $TDP - 2mW$ for testing in backoff, to $TDP + 2mW$ for testing with light contact and to $TDP + 20mW$ for testing with overpush conditions. The TFC pulses are supplied for a duration of 60 minutes and the OSA scans taken at specified time intervals to see the lubricant evolution with time. It is pointed out that in order to ensure good synchronization of the TFC pulse with the spindle index the Labview program is written to acquire the spindle index before every TFC pulse. This procedure and the resulting Labview computation time delay imposes an inherent limitation, and consequently the TFC pulses do not occur every disk revolution, but instead there are about 10 idle disk revolutions without any TFC pulse for every revolution with a TFC pulse, as shown in the representative plot Fig 8.3. In other words, one minute of testing is equivalent to approximately 600 TFC pulses with about 10 idle disk revolutions between each pulse.

8.2 Results and Discussion

A representative touchdown plot using the automated Labview code is shown in Fig 8.4. For this case the TDP is $70mW$ and at this power the AE signal σ increases sharply above 50% of the baseline. Once the touchdown power is determined, tests are conducted with the TFC power pulse input in backoff, light contact and overpush. The results for the overpush case are discussed first followed by a comparison with the results for the case of light contact and backoff conditions.

8.2.1 Lubricant behavior in overpush

The OSA scans monitoring lubricant evolution with time for tests with $20mW$ overpush (TFC heater power of $TDP + 20mW$) on a disk with ZTMD lubricant are shown in Fig 8.5. This figure shows the full circumference 360^o and a $300\mu m$ wide section of the track under the TFC protrusion, and the angular section of the disk where the TFC power is 'on' and 'off' are indicated. The slider flies over the disk track from left to right as indicated by the direction of the arrows. A lighter color on the OSA scan implies lubricant depletion

and a darker color implies lubricant accumulation. It is observed that the most significant lubricant change in all of these plots occurs at angular sections that correspond to the onset and end of contact (i.e. where the heater is turned 'on' and turned 'off'). The interesting feature is that even after fairly long durations (up to 30 minutes) the lubricant change in the middle of the section where the TFC power is 'on' is minimal.

A zoomed image of the angular section (70^o long and $300\mu m$ wide) near the onset of contact (where the TFC power is turned 'on') is shown in Fig 8.6. Interestingly, lubricant accumulation is observed when the TFC power is turned 'on' suggesting lubricant deposition/transfer from the slider to the disk as the TFC protrusion approaches the disk. It is surmised that any lubricant that is collected on the slider's trailing pad (deposited end) [Pit et al. 2003] bridges the gap between the slider and disk at small clearances as the TFC protrusion approaches the disk and results in lubricant transfer from the slider to the disk. It is noted that following this lubricant accumulation region (which signals the beginning of contact) there is a section of lubricant depletion/removal from the disk because the TFC protrusion enters into an interference condition as the TFC power rises quickly to the peak value of $TDP + 20mW$. Of particular importance is that this lubricant depletion does not continue for the entire duration of the TFC pulse. In fact, it is seen that after the small angular section that marks lubricant depletion, the OSA scans indicate a negligible change of the lubricant in these tests (especially up to the 30 minute scan which is a fairly long duration). There is some change in the lubricant profile for longer durations as observed in the 60 minute scan, but this change is much smaller compared to the strong changes observed at the beginning of contact. This lubricant distribution trend that occurs when the TFC power is turned 'on' is confirmed to be repeatable based on several experiments with this ABS design: an angular section marking lubricant accumulation, followed by an angular section marking lubricant depletion (with possibly some lubricant rippling), finally followed by negligible lubricant thickness changes.

A similar zoomed image corresponding to the angular section near the end of contact (where the TFC power is turned 'off') is shown in Fig 8.7. A distinct lubricant change is observed at the end of contact (which is stronger than the changes observed in the section with TFC power 'on') indicating enhanced slider lubricant interactions as the thermal protrusion retracts away from the disk when the TFC power is turned 'off'. It is pointed out that while the current test shows a strong lubricant accumulation at the end of contact, a strong lubricant depletion has also been observed in other tests with the same slider ABS and media combination.

Similar results are obtained for tests conducted with media coated with Z-tetraol lubricant are shown in Fig 8.8 - Fig 8.10.

The amount of lubricant accumulated at the onset of contact is computed using the OSA images as shown in Fig 8.11 for two experiments conducted on media coated with ZTMD and Z-tetraol. The accumulated volume increases gradually with time, but a contacting HDI is subject to complex slider lubricant interactions and more experiments are required to verify the quantitative results reported in this work.

8.2.2 Lubricant behavior in backoff

An understanding of disk lubricant distribution and its dependence on the TFC power is discussed in this section. Fig 8.12 and Fig 8.13 show the zoomed OSA scans of the angular sections marking the TFC power 'on' and TFC power 'off', respectively, after 60 minutes of testing in backoff ($TDP-5mW$,$TDP-2mW$), in light contact ($TDP+2mW$), and in overpush ($TDP+20mW$) for ZTMD lubricant. It is observed from Fig 8.12a and Fig 8.12b that even in the case of backoff (as with the case of overpush), there is a zone of lubricant accumulation when the TFC power is turned 'on'. This test confirms the premise that lubricant transfer from the slider to the disk may occur when the physical clearance becomes small under the thermal protrusion. It is noted that this lubricant accumulation zone is limited only to a small angular section where the TFC power is turned 'on'. It is presumed that the initial transfer of lubricant from the slider to the disk reduces the slider-lubricant interaction and hence no lubricant changes are observed farther downtrack even if the TFC power remains turned 'on'.

For the case with contact ($TDP+2mW$) shown in Fig 8.12c, it is observed that the initial lubricant accumulation zone is followed by strong lubricant rippling, and there is substantial slider bouncing in this case. The lubricant rippling frequency correlates well with slider bouncing frequencies Fig 8.14. It is noted that lubricant rippling and slider bouncing are suppressed in overpush, and Fig 8.12d shows that the lubricant changes are negligible in the section with TFC power turned 'on' (except at the beginning and end of contact), and are in fact comparable to the case of backoff. Suppression of slider vibrations in overpush and the corresponding absence of lubricant rippling are slider ABS specific phenomenon. It is expected therefore that the lubricant behavior observed in these tests would change for sliders with different ABS designs, especially for those designs which do not result in a suppression of slider vibrations in overpush.

Similar results are observed for tests with Z-tetraol lubricant as shown in Fig 8.15 and Fig 8.16. One key difference in this particular experiment with Z-tetraol is that lubricant rippling is not significant for the case of light contact ($TDP+2mW$). It is not a typical result. Generally, for this ABS design, lubricant rippling and slider bouncing dynamics are significant for the case of light overpush, and they get suppressed for stronger overpush as reported in previous research work [Vangipuram Canchi and Bogy 2011a,b].

The important correlations between lubricant thickness changes and slider dynamics may be summarized for this particular ABS design. During an overpush test, the physical spacing between the thermal protrusion and the disk is first reduced and the slider then moves into a condition of light contact before moving into an overpush condition. When the physical spacing under the thermal protrusion approaches the contact condition, there is a tendency for lubricant transfer from the slider's trailing end to the disk. As the slider moves into a light contact condition, it exhibits 'unstable' slider dynamics that is associated with lubricant depletion and rippling. Some plausible reasons for this instability have been discussed and attributed to system nonlinearities [Vangipuram Canchi and Bogy 2011a]. In the overpush condition, the slider exhibits 'stable' dynamics which is also interestingly marked with negligible lubricant change and smaller lubricant depletion [Vangipuram Canchi and Bogy 2011b]. This condition with 'stable' dynamics is the interesting zone also speculated to correspond to the lubricant-surfing regime [Liu et al. 2009]. Contrary to expectation, significant

lubricant changes do not appear in this lubricant-contact regime, and a full understanding of the HDI is not yet available. The effect of slider and lubricant parameters on lubricant distribution and HDI behavior still remains to be understood and these investigations are necessary to design and realize a successful contacting HDI.

8.3 Conclusion

Slider lubricant interactions at the HDI are investigated using carefully designed experiments that actuate TFC sliders into proximity (backoff), light contact and overpush on one specific half of the disk track every disk revolution. Lubricant accumulation is observed in all cases (backoff, light contact and strong overpush) at the location where the TFC power is turned 'on' indicating possible transfer of lubricant from the trailing end of the slider to the disk. The accumulated lubricant quantity generally increases with time. For this ABS design, light contact tests generally result in an 'unstable' condition marked with slider bouncing and lubricant rippling at air bearing frequencies. Stronger overpush conditions lead to a 'stable' state associated with no slider bouncing that interestingly also corresponds with a negligible change in the disk lubricant thickness. In the overpush case, the greatest changes to the lubricant distribution occur at the onset and end of contact. The onset of contact is characterized by a repeatable lubricant thickness change that is independent of the lubricant type (ZTMD or Z-tetraol) used in this work: an angular section marked with lubricant accumulation, followed by an angular section marked with lubricant depletion (with possibly some lubricant rippling), and finally followed by negligible thickness changes for the strong overpush case. This lubricant behavior may vary depending on the ABS design. This research work reveals the complex nature of slider-lubricant interactions under near-contact and contact conditions. Slider-lubricant interactions at a contacting HDI are still not fully understood and thorough investigations on this topic are required to enable the disk drive industry to meet the magnetic spacing targets imposed by the data density goals of the future.

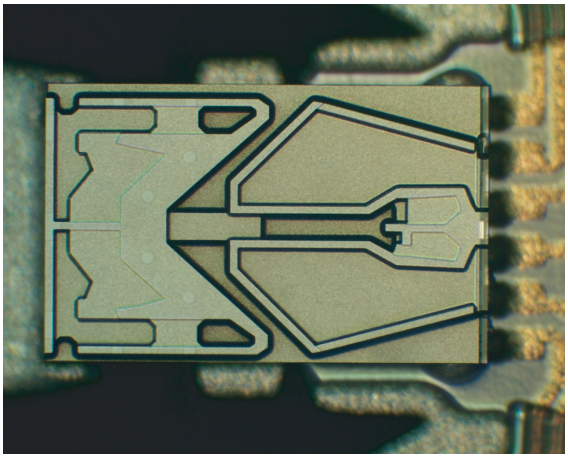

Figure 8.1: Slider ABS design

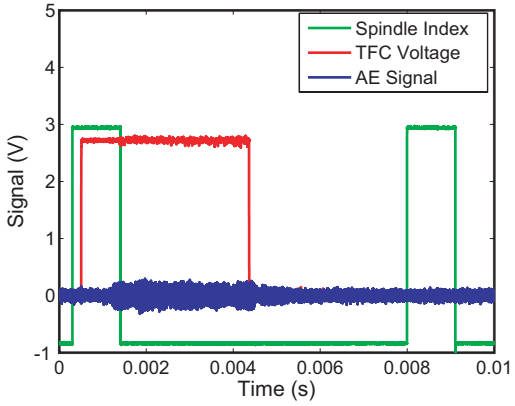

Figure 8.2: TFC heater power pulse lasting one half of a disk revolution

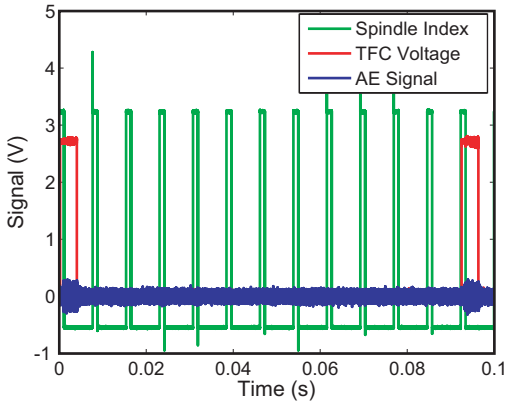

Figure 8.3: TFC heater power pulses and idle revolutions between pulses

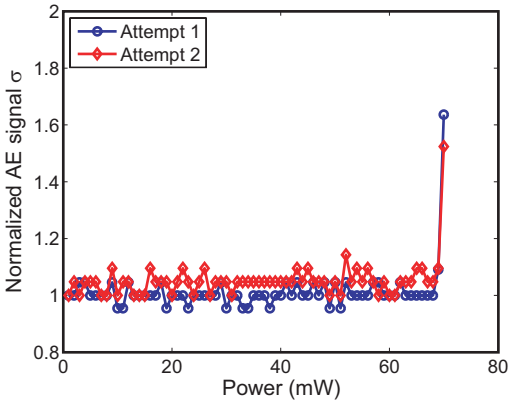

Figure 8.4: Touchdown detection plot

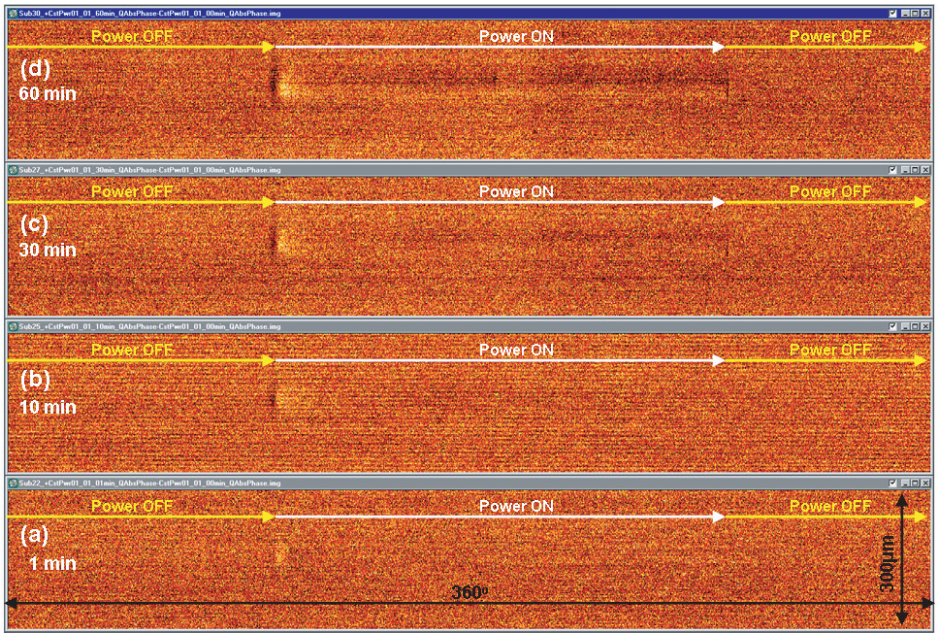

Figure 8.5: ZTMD lubricant change with time for $20mW$ overpush

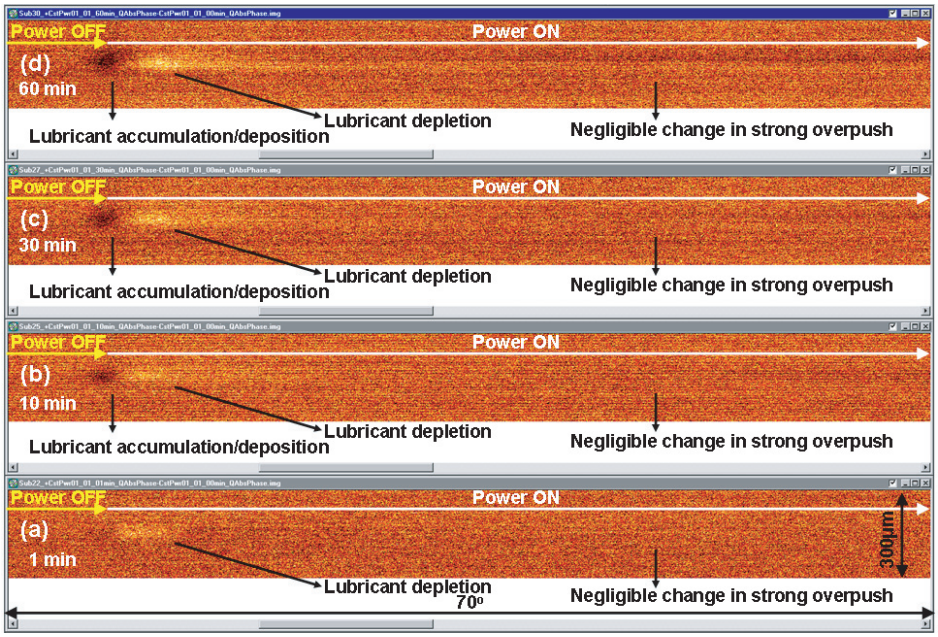

Figure 8.6: Zoomed image showing ZTMD lubricant change with time for $20mW$ overpush showing region near the onset of contact

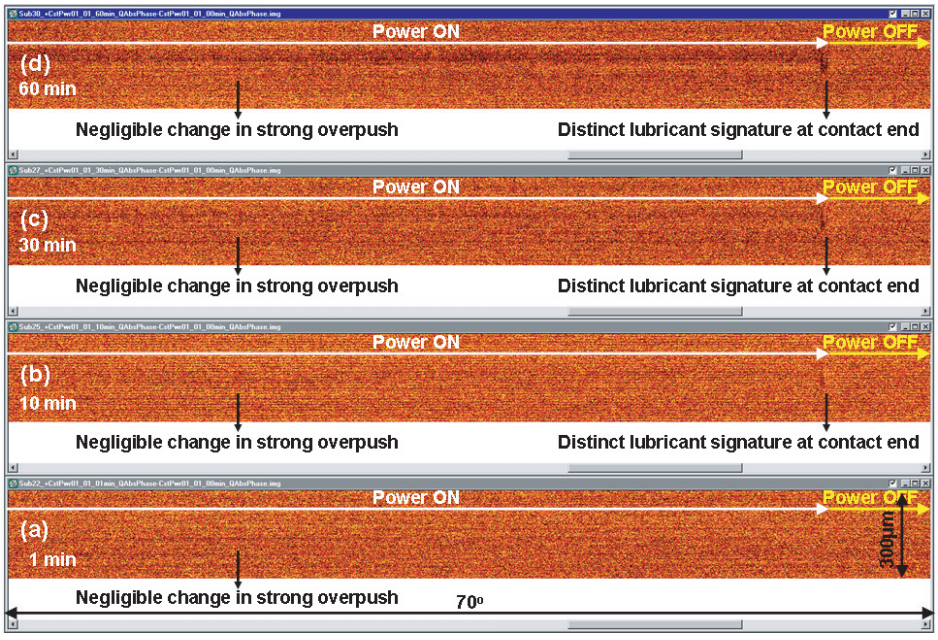

Figure 8.7: Zoomed image showing ZTMD lubricant change with time for $20mW$ overpush showing region near the end of contact

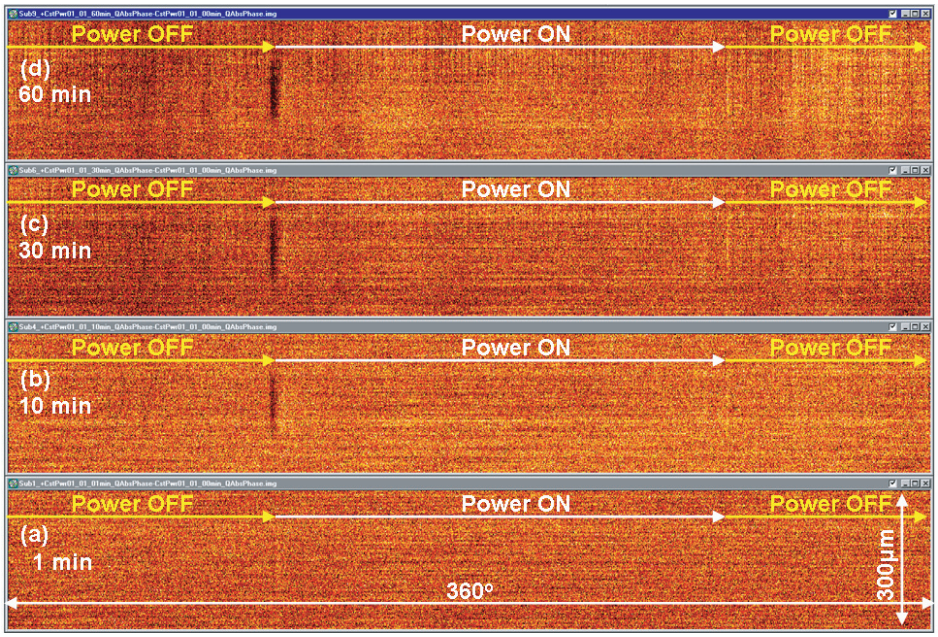

Figure 8.8: Z-tetraol lubricant change with time for $20mW$ overpush

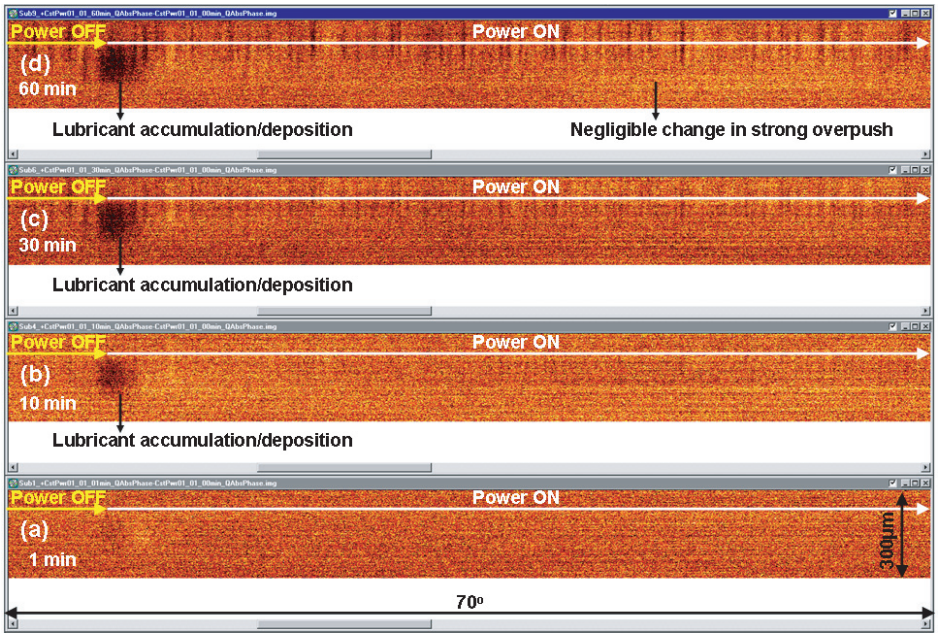

Figure 8.9: Zoomed image showing Z-tetraol lubricant change with time for $20mW$ overpush showing region near the onset of contact

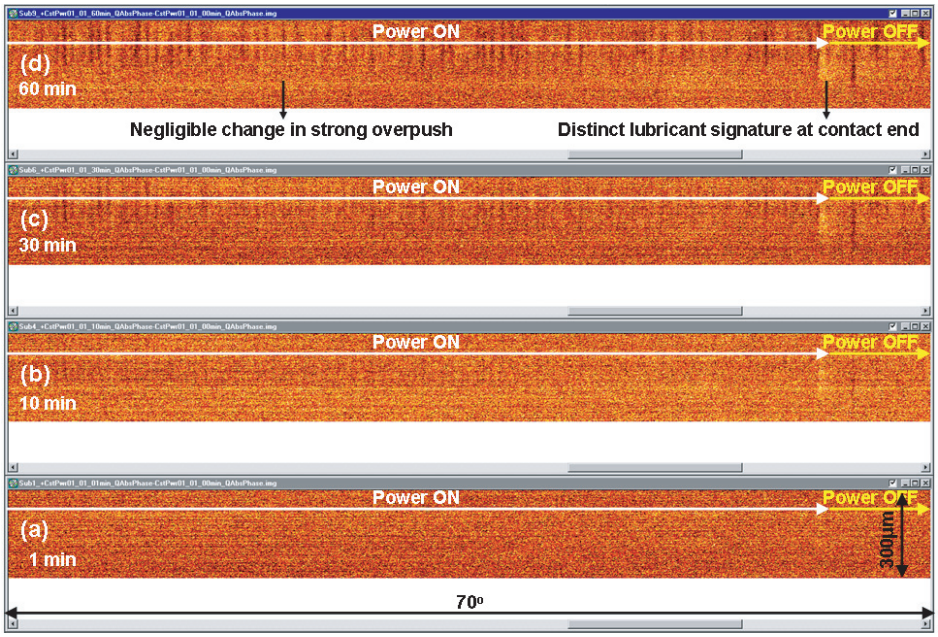

Figure 8.10: Zoomed image showing Z-tetraol lubricant change with time for $20mW$ overpush showing region near the end of contact

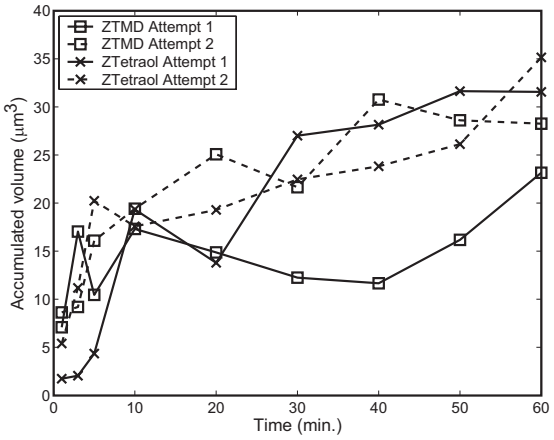

Figure 8.11: Growth with time of the accumulated lubricant volume near the onset of contact for $20mW$ overpush

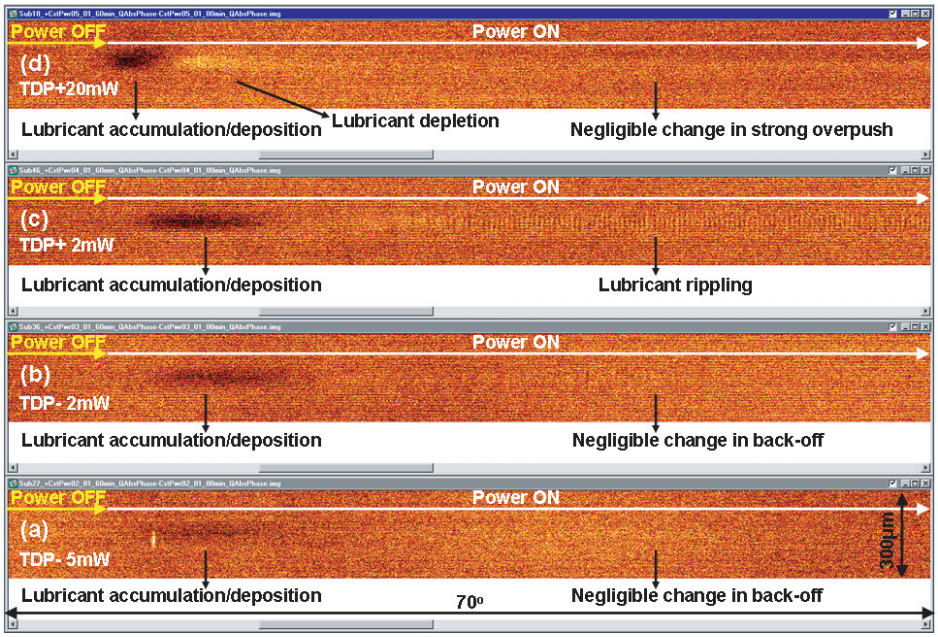

Figure 8.12: ZTMD lubricant accumulation near the onset of contact for backoff and overpush

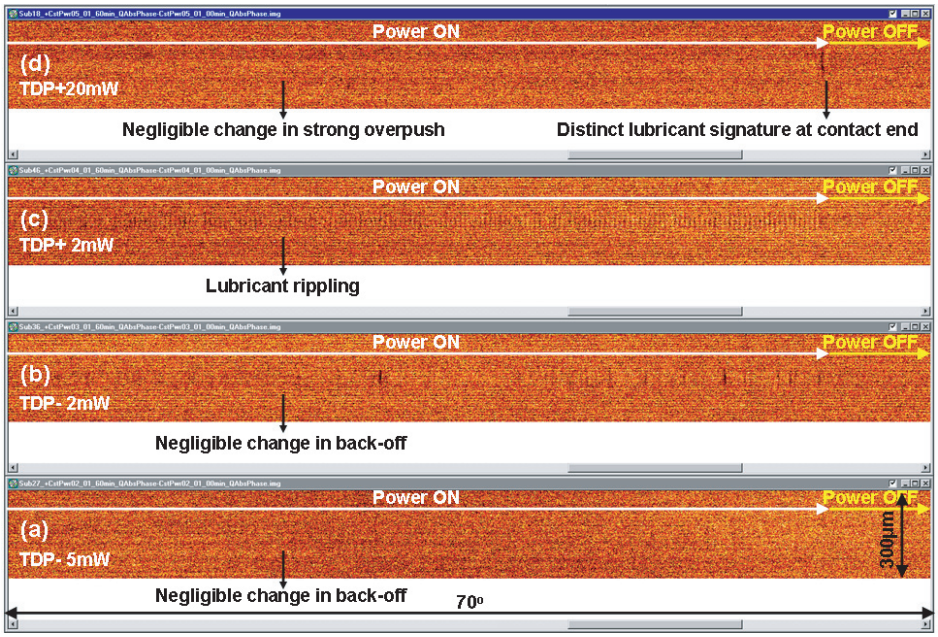

Figure 8.13: ZTMD lubricant distribution near the end of contact for backoff and overpush

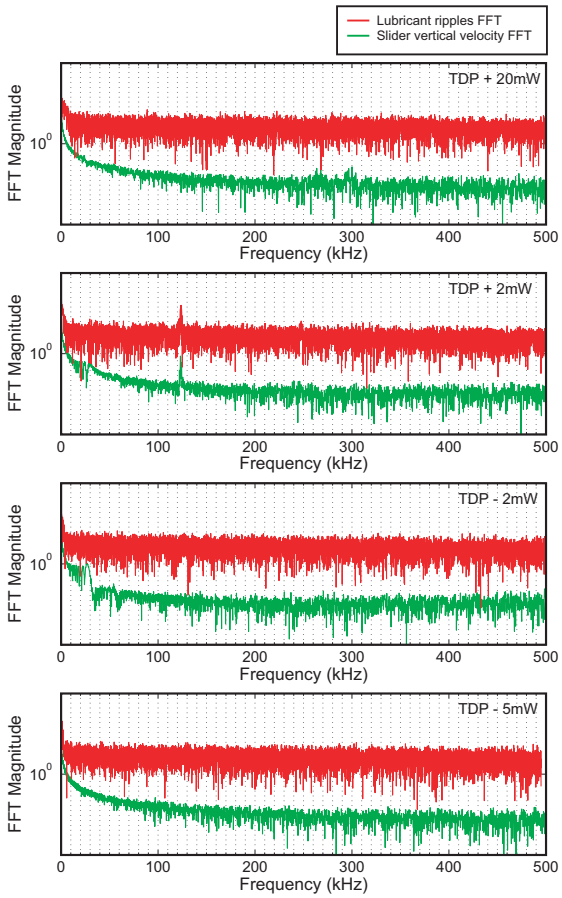

Figure 8.14: Slider's vertical velocity spectrum and disk lubricant spectrum for backoff and overpush

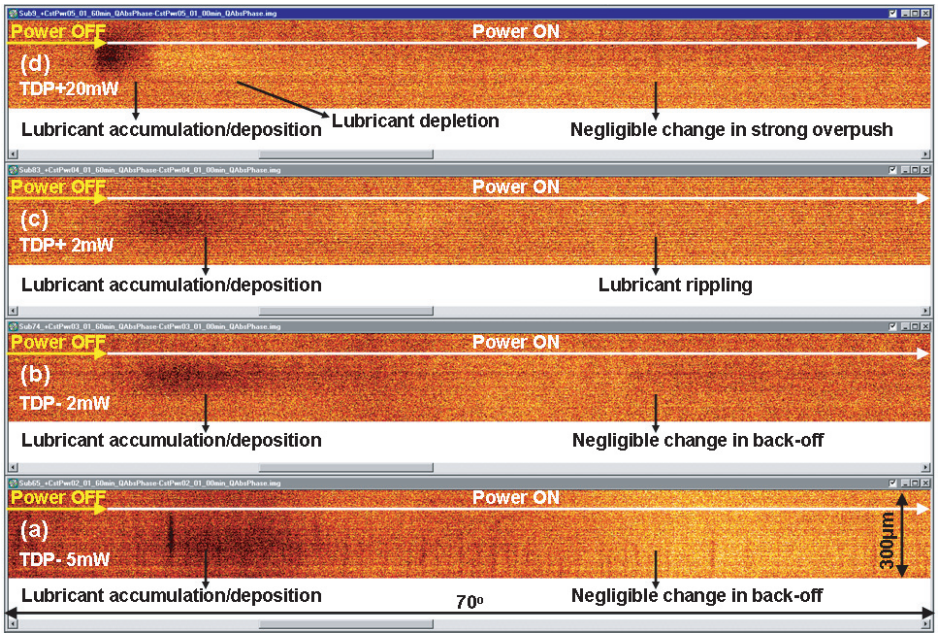

Figure 8.15: Z-tetraol lubricant accumulation near the onset of contact for backoff and overpush

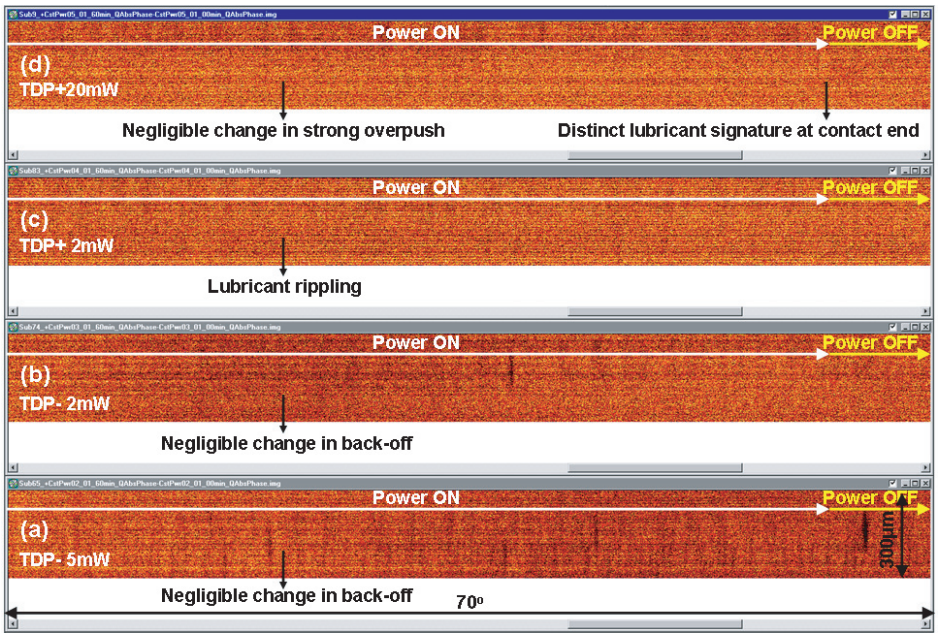

Figure 8.16: Z-tetraol lubricant distribution near the end of contact for backoff and overpush

References

R Ambekar and DB Bogy. Effect of slider lubricant pickup on stability at the head-disk interface. *IEEE Transactions on Magnetics*, 41(10):3028–3030, 2005.

R Ambekar and DB Bogy. Lubircant depletion and disk-to-head lubricant transfer at the head-disk interface in hard disk drives. *Proceedings of STLE/ASME International Joint Tribology Conference 2006*, 2006.

R Ambekar, V Gupta, and DB Bogy. Experimental and numerical investigation of dynamic instability in the head disk interface at proximity. *Journal of Tribology*, 127(3):530–536, 2005.

D Chen and DB Bogy. Dynamics of partial contact head disk interface. *IEEE Transactions on Magnetics*, 43(6):2220–2222, 2007.

CMLAir. The cml air bearing design program user's manual (version 7.0). *Computer Mechanics Laboratory Technical Report*, 2007.

Q Dai, BE Knigge, RJ Waltman, and B Marchon. Time evolution of lubricant-slider dynamic interactions. *IEEE Transactions on Magnetics*, 39(5):2459–2461, 2003.

Q Dai, F Hendriks, and B Marchon. Modeling the washboard effect at the head/disk interface. *Journal of Applied Physics*, 96(1):696–703, 2004a.

Q Dai, F Hendriks, and B Marchon. Washboard effect at head-disk interface. *IEEE Transactions on Magnetics*, 40(4):3159–3161, 2004b.

V Gupta and DB Bogy. Dynamics of sub-5-nm air-bearing sliders in the presence of electrostatic and intermolecular forces at the head-disk interface. *IEEE Transactions on Magnetics*, 41(2):610–615, 2005.

J Kiely and Y-T Hsia. Three-dimensional motion of sliders contacting media. *Journal of Tribology*, 128(3):525–533, 2006.

J Kiely and Y-T Hsia. Slider dynamic motion during writer-induced head-disk contact. *Microsystem Technologies*, 14:403–409, 2008.

B Knigge and FE Talke. Dynamics of transient events at the head/disk interface. *Tribology International*, 34:453–460, 2001.

B Liu, MS Zhang, SK Yu, W Hua, CH Wong, WD Zhou, YJ Man, L Gonzaga, and YS Ma. Towards fly- and lubricant-contact recording. *Journal of Magnetism and Magnetic Materials*, 320:3183–3188, 2008.

B Liu, MS Zhang, SK Yu, W Hua, YS Ma, WD Zhou, L Gonzaga, and YJ Man. Lube-surfing recording and its feasibility. *IEEE Transactions on Magnetics*, 45(2):899–904, 2009.

B Marchon, T Karis, Q Dai, and R Pit. A model for lubricant flow from disk to slider. *IEEE Transactions on Magnetics*, 39(5):2447–2449, 2003.

B Marchon, XC Guo, A Moser, A Spool, R Kroeker, and F Crimi. Lubricant dynamics on a slider: "the waterfall effect". *Journal of Applied Physics*, 105(7), 2009.

MC Mate, PC Arnett, P Baumgart, Q Dai, UM Guruz, BE Knigge, RN Payne, OJ Ruiz, GJ Wang, and BK Yen. Dynamics of contacting head-disk interfaces. *IEEE Transactions on Magnetics*, 40(4):3156–3158, 2004.

MC Mate, B Marchon, AN Murthy, and S-H Kim. Lubricant-induced spacing increases at slider-disk interfaces in disk drives. *Tribology Letters*, 37:581–590, 2010.

DW Meyer, PE Kupinski, and JC Liu. Slider with temperature responsive transducer positioning. *United States Patent 5991113*, 1999.

S Moseley and DB Bogy. Experimental evidence of lubricant droplet transfer from slider to disk. *IEEE Transactions on Magnetics*, 45(2), 2009.

AH Nayfeh and DT Mook. *Nonlinear oscillations*. John Wiley & Sons, New York, 1979.

R Pit, Q-H Zeng, Q Dai, and B Marchon. Experimental study of slider-lubricant interactions. *IEEE Transactions on Magnetics*, 39(2):740–742, 2003.

Y Shimizu, J Xu, H Kohira, K Kuroki, and K Ono. Experimental study on slider dynamics during touchdown by using thermal fly-height control. *ASME Information Storage and Processing Systems Conference, Santa Clara*, 2010.

BH Thornton and DB Bogy. Nonlinear aspects of air-bearing modeling and dynamic spacing modulation in sub-5nm air bearings for hard disk drives. *IEEE Transactions on Magnetics*, 39(2):722–728, 2003a.

BH Thornton and DB Bogy. Head-disk interface instability due to intermolecular forces. *IEEE Transactions on Magnetics*, 39(5):2420–2422, 2003b.

GW Tyndall, RJ Waltman, and DJ Pocker. Concerning the interactions between z-dol perfluoropolyether lubricant and an amorphous-nitrogenated carbon surface. *Langmuir*, 14:7527–7536, 1998.

AI Vakis, S-C Lee, and A Polycarpou. Dynamic head-disk interface instabilities with friction for light contact (surfing) recording. *IEEE Transactions on Magnetics*, 45(11):4966–4971, 2009.

S Vangipuram Canchi and D Bogy. Experimental investigation of slider dynamics at a contacting head-disk interface. *Computer Mechanics Laboratory Technical Report*, 2009.

S Vangipuram Canchi and D Bogy. Slider dynamics in the lubricant-contact regime. *IEEE Transactions on Magnetics*, 46(3):764–769, 2010.

S Vangipuram Canchi and D Bogy. Thermal fly-height control slider instability and dynamics at touchdown: explanations using nonlinear systems theory. *Journal of Tribology*, 133(2), 2011a.

S Vangipuram Canchi and D Bogy. Slider-lubricant interactions and lubricant distribution for contact and near contact recording conditions (accepted). *IEEE Transactions on Magnetics*, 2011b.

RL Wallace. The reproduction of magnetically recorded signals. *The Bell System Technical Journal*, 30:1145–1173, 1951.

RJ Waltman. The interactions between z-tetraol perfluoropolyether lubricant and amorphous nitrogenated- and hydrogenated-carbon surfaces and silicon nitride. *Journal of Fluorine Chemistry*, 125:391–400, 2004.

R-H Wang, V Nayak, F-Y Huang, W Tang, and F Lee. Head-disk dynamics in the flying, near contact, and contact regimes. *Journal of Tribology*, 123:561–565, 2001.

L Wu and DB Bogy. Effect of the intermolecular forces on the flying attitude of sub-5 nm flying height air bearing sliders in hard disk drives. *Journal of Tribology*, 124(3):562–567, 2002.

J Xu, H Kohira, H Tanaka, and S Saegusa. Partial-contact head-disk interface approach for high density recording. *IEEE Transactions on Magnetics*, 41(10):3031–3033, 2005.

S Yu, B Liu, W Hua, and W Zhou. Dynamics of read/write head positioning in both flying-height and off-track directions. *IEEE Transactions on Magnetics*, 43(9):3796–3801, 2007.

SK Yu, B Liu, WD Zhou, W Hua, and L Gonzaga. Dynamic stability analysis for surfing head-disk interface. *IEEE Transactions on Magnetics*, 45(11):4979–4983, 2009.

Q-H Zeng and D Bogy. The cml slider-air bearing parameter identification program. *Computer Mechanics Laboratory Technical Report*, 1997.

Q-H Zeng, C-H Yang, S Ka, and E Cha. An experimental and simulation study of touch-down dynamics (submitted). *IEEE Transactions on Magnetics*, 2011.

J Zheng and D Bogy. Thermal fly-height control (tfc) code user's manual. *Computer Mechanics Laboratory Technical Report*, 2009.

J Zheng and D Bogy. Investigation of flying height stability of thermal fly-height control sliders in lubricant or solid disk contact with roughness. *Tribology Letters*, 38(3):283–289, 2010.